Modeling the Role of Surfaces and Grain Boundaries in Plastic Deformation

Bryan Kuhr

Dissertation submitted to the Faculty of the

Virginia Polytechnic Institute and State University

in partial fulfillment of the requirements for the degree of

Doctor of Philosophy

in

Materials Science and Engineering

Diana Farkas (Chair)

Sean G Corcoran

Celine Hin

William T Reynolds

June 14, 2014, Blacksburg, VA

Modeling the Role of Surfaces and Grain Boundaries in Plastic Deformation

Bryan Kuhr

ABSTRACT

In this dissertation, simulation techniques are used to understand the role of surfaces and grain boundaries in the deformation response of metallic materials. This research utilizes atomistic scale modeling to study nanoscale deformation phenomena with time and spatial resolution not available in experimental testing. Molecular dynamics techniques are used to understand plastic deformation of grain boundaries and surfaces in metals under different configurations and loading procedures.

Stress and strain localization phenomena are investigated at plastically deformed boundaries in axially strain thin film samples. Joint experimental and modelling work showed increased stress states at the intersections of slip planes and grain boundaries. This effect, as well as several other differences related to stress and strain localization are thoroughly examined in digital samples with two different grain boundary relaxation states. It is found that localized stress and strain is exacerbated by initial boundary disorder.

Dislocation content in the randomly generated boundaries of these samples was quantified via the dislocation extraction algorithm. Significant numbers of lattice dislocations were present in both deformed and undeformed samples. Trends in dislocation content during straining were identified for individual samples and boundaries but were not consistent across all examples. The various contributions to dislocation content and the implications on material behavior are discussed.

The effects of grain boundary hydrogen on the deformation response of a digital Ni polycrystalline thin film sample is reported. H content is found to change the structure of the boundaries and effect dislocation emission. The presence of dispersed hydrogen caused a slight increase in yield strength, followed by an increase in grain boundary dislocation emission and an increase in grain boundary crack formation and growth.

An atomistic nano indenter is employed to study the nanoscale contact behavior of the indenter-surface interface during nano-indentation. Several indentation simulations are executed with different interatomic potentials and different indenter orientations. A surface structure is identified that forms consistently regardless of these variables. This structure is found to affect several atomic layers of the sample. The implications of this effect on the onset of plasticity are discussed.

Finally, the implementation of an elastic/plastic continuum contact solution for use in mesoscale molecular dynamics simulations of solid spheres is discussed. The contact model improves on previous models for the forces response of colliding spheres by accounting for a plastic regime after the point of yield. The specifics of the model and its implementation are given in detail.

Overall, the dissertation presents insights into basic plastic deformation phenomena using a combination of experiment and theory. Despite the limitations of atomistic techniques, current computational power allows meaningful comparison with experiments.

Modeling the Role of Surfaces and Grain Boundaries in Plastic Deformation

Bryan Kuhr

GENERAL AUDIENCE ABSTRACT

Certain engineering metals have a remarkable bend-then-break quality. This allows a metal component to withstand damage without totally failing. The process of permanent distortion is called plastic deformation. Metals, in nearly all practical forms, contain defects. During plastic deformation, defects are generated, moved, changed and annihilated. The rates of these actions govern the mechanical behavior of metals. There are several types of defects and several ways in which they can interact, forming a complex interplay during plastic deformation. The focus of this dissertation is on plastic deformation associated with two particular defect types: surfaces and grain boundaries. Because these defects occur on a very small length scale, the details of their behavior can best be observed via simulation. For this reason, Molecular Dynamics was employed as the primary research tool, and other methods were used for validation. This allows fully 3D rendering of our simulated samples with atom-scale resolution, and complete stress/energy information. In each of the 6 manuscripts presented in this dissertation, new insights into the plastic deformation around surfaces or grain boundaries is presented.

DEDICATION

To my parents Peggy and Richard for the countless ways you have supported me and contributed to this pursuit. Your love and patience during this process has been inspiring.

CONTENTS

LIST OF FIGURES

LIST OF TABLES

INTRODUCTION

Atomistic simulation has a vital role to play in understanding plasticity. The calculations are simple enough that a simulation can include millions of atoms over millions of time steps, yet accurate enough to realistically represent crystal defects. Atomic scale resolution of simulated systems is available to the researcher, allowing time and length scale resolution not available in experiment. For instance, a 3D characterization of a dislocation or the pinpointing of a dislocation source is easily achieved in simulation, but extremely difficult in experiment. The growing availability of super computing power allow a variety of length scales to be achieved.

This dissertation is compiled in manuscript format in accordance with the Virginia Tech Graduate School guidelines. It includes 6 manuscripts that have been prepared by the author during his doctoral candidacy. These manuscripts make up chapters 2-6. The first chapter contains explanations of simulation tools and scientific concepts that were excluded from the manuscripts for brevity. The order in which the manuscripts are presented is intended to follow the logical connections of their content. Chapters 2-5 focus on grain boundary deformation mechanisms, with somewhat different approaches. Chapter 2 (published in Scripta Materialia [1]) and chapter 3 (in preparation for submission to the International Journal of Plasticity), examine the stress and strain states of boundaries undergoing deformation. Chapter 4 (also in preparation for submission to IJP) and chapter 5 (published in Computational Materials Science [2]) compare dislocation content in samples with defect-dense boundary regions. Chapter 6 (published in the Journal of Physical Chemistry C [3]) and chapter 7 (a government report prepared for Sandia National Laboratories [4]) consider near-surface deformation of plastically deforming metals under contact pressure. The dissertation also includes all the front matter recommended by the Graduate School and a summary of the conclusions in this work following the chapters.

1.	Johnson, D.C., et al., *Quantitative analysis of localized stresses in irradiated stainless steels using high resolution electron backscatter diffraction and molecular dynamics modeling.* Scripta Materialia, 2016. **116**: p. 87-90.
2.	Kuhr, B., D. Farkas, and I.M. Robertson, *Atomistic studies of hydrogen effects on grain boundary structure and deformation response in FCC Ni.* Computational Materials Science, 2016. **122**: p. 92-101.
3.	Tavazza, F., et al., *Ni Nanoindentation at the Nanoscale: Atomic Rearrangements at the Ni-C Interface.* Journal of Physical Chemistry C, 2017. **121**(5): p. 2643-2651.
4.	Kuhr, B., M.R.W. Brake, and J.B. Lechman, *An Elastic Plastic Contact Model with Strain Hardening for the LAMMPS Granular Package.* 2015.

ACKNOWLEDGEMENTS AND ATTRIBUTIONS

The following is a summary of the contributions to this work made by my collaborators. My sincere thanks to each of them.

Dr. Diana Farkas *is a professor in the Materials Science and Engineering Department at Virginia Tech (VT). She is my dissertation advisor and committee chair. She principally conceived the research goals and provided advice, revisions and content in all stages of the research in chapters 2-6 of this dissertation.*

Dr. Laura Smith *is an Engineer at the U. S. Nuclear Regulatory Commission and former advisee of Diana Farkas at VT. She provided preliminary results, including digital samples and simulation procedures that were the basis for chapters 2- 5.*

Dr. Gary Was *is a professor in the Nuclear Engineering department at the University of Michigan (UM). He helped conceive the research goals and provided advice that guided the work in chapters 2-5.*

Mr. Drew Johnson *is a doctoral candidate and advisee of Dr. Was at UM. He was the primary researcher for chapter 2. He executed the experimental and characterization work. He wrote portions of the text and created figures 2-1 and 2-4 and parts of figure 2-3. He also contribute the experimental findings in chapter 3. He worked closely with me during the conception and execution of the work in chapter*

Dr. Ian Robertson *is the Dean of the College of Engineering at the University of Wisconsin (UW). He helped conceive the basic research goals and provided advice that guided the work in chapters 2-5. He co-authored chapter 5 providing several rounds of edits and rewrites.*

Dr. Rigen Mo *is a post-doctoral researcher and advisee of Ian Roberson at UW. He worked closely with us during the conception and execution of the work in chapters 2-5.*

Dr. Francesca Tavazza *is a researcher at the National Institute for Standards in Technology (NIST). She was the lead researcher in chapter 6. She executed all of the Density Functional Theory (DFT) simulations and some of the Molecular Dynamics simulations. She wrote portions of the text and generated all of the figures in this chapter.*

Dr. Lyle Levine *is a researcher at NIST. He contributed advice and revisions to chapter 6.*

Dr. Mathew Brake *is currently a professor at Rice University and formerly a researcher at Sandia National Laboratories (SNL). He conceived the research goal and provided advice throughout the execution of the work in chapter 7 as well as its writing.*

Dr. Jeremy Lechman *is a researcher at SNL. He helped develop the simulation tools and procedures in chapter7.*

Dr. AlexanderJeremy Lechman *is a researcher at SNL. He helped develop the simulation tools and procedures in chapter7.*

CHAPTER 1: BACKGROUND

The principle simulation tool in this dissertation is molecular dynamics (MD) using the embedded atom method (EAM) in the LAMMPS implementation. The following is a brief description of this method, including its scientific basis and use in current research.

1.1 Molecular Dynamics Overview

MD modeling is a simulation method for estimating the behavior of a many-body system confined to a parallelepiped-shaped simulation box over a finite period of time. These bodies, usually intended to describe atoms or molecules, are modelled as point masses. Each body can exert a force on and affect the potential energy of surrounding bodies. Conversely, each atom has a net force and potential energy resulting from its position relative to surrounding bodies. The specifics of the energetics are defined by a series of equations and empirical values collectively known as an interatomic potential. This will be discussed in a later section.

In addition to position, force and potential energy, MD also considers each atom's mass and velocity. The least computationally expensive MD ensemble is called the microcanonical or NVE (fixed <u>N</u>umber of atoms, <u>V</u>olume and total <u>E</u>nergy) ensemble. In this scenario, the motion of an atom is described by Newton's equations of motion.

$$\frac{d\mathbf{r}_i}{dt} = \mathbf{v_i}; \qquad \frac{d\mathbf{v}_i}{dt} = \mathbf{a_i} = \frac{\mathbf{f}_i}{m_i} \tag{1}$$

where $\mathbf{r_i}$, $\mathbf{v_i}$, $\mathbf{a_i}$ and m_i are the position, velocity and acceleration vectors and mass of atom i; f_i is the net force vector acting on atom i; and t represents time. Each atom's acceleration vector is calculated from its mass and the net force acting on it. Its change in velocity is then calculated by integrating this acceleration over the simulation timestep. Likewise, its position change is calculated by integrating the velocity. New forces and potential energies are calculated from the new positions at this new time step.

This process repeats until some predetermined number of timesteps are executed. The system temperature is calculated using a derivation of the ideal gas law of the form:

$$T = \frac{2E_k}{3Nk_B} = \frac{2}{3Nk_B}\sum_{i=o}^{N}\frac{1}{2}m_i|\mathbf{v}_i|^2 \tag{2}$$

where T and E_k, are the temperature and total kinetic energy of the system, N is the total number of atoms and k_B is the Boltzmann constant. The system pressure [1] is calculated during the simulation by the virial stress. This can be expressed as

$$P = \frac{Nk_BT}{V} + \frac{1}{3V}\sum_{i=o}^{N}\sum_{j=o}^{i-1}(\mathbf{r}_i - \mathbf{r}_j)\cdot\mathbf{f}_{ij} \tag{3}$$

where P is the calculated pressure of the system and V volume of the simulation box. The second term can be expressed as the summed dot products of each atom pair's relative position vector and interaction force. Often, MD simulations include a cutoff radius, such that atoms that are far apart do not interact. Thus, in large simulations, most f_{ij} is equal to zero.

1.2 Thermostatting in MD

In many cases, it is more representative to fix the temperature of a system and allow the total energy to fluctuate. This requires a periodic adjustment of the atomic velocities to conserve the temperature of the system. The specific numerical approach to this adjustment is known as the thermostat. Several thermostats are available in MD, which differ in their assumptions about how temperature is regulated. One of the simplest thermostats is the Gaussian isokinetic thermostat (also known as a velocity rescaling thermostat) [2], which simply applies an adjustment to the velocity of every atom in the system according to

$$\mathbf{v}_i \rightarrow \sqrt{\frac{T_0}{T}}\mathbf{v}_i \tag{4}$$

where T is the instantaneous temperature, T_0 is the desired temperature. This method successfully maintains the temperature of the system.

It has been argued, however, that rather than maintaining a constant temperature, it is more physically

realistic that a collection of atoms in a simulation maintain thermal equilibrium with an external mass

that is maintained at a constant temperature, called a heat bath. This is referred to as a canonical, or

NVT (fixed Number of atoms, Volume and Temperature) ensemble. Such a method was developed by

Nose, and later reinterpreted by Hoover and is commonly referred to as a Noose-Hoover thermostat [3].

Use of a Noose-Hoover thermostat alters the equations of motion to the form

$$\frac{d\mathbf{r}_i}{dt} = \mathbf{v}_i; \qquad \frac{d\mathbf{v}_i}{dt} = \frac{\mathbf{f}_i}{m_i} - \zeta\mathbf{v}_i \tag{5}$$

where thermostat friction coefficient, ζ, is a system-wide, time-dependent variable controlled by the

differential equation

$$\frac{d\zeta}{dt} = \frac{1}{t_T{}^2}\left(\frac{T}{T_0} - 1\right) \tag{6}$$

where t_T is the thermal relaxation time, which must be specified by the user. Rather than insuring a

constant temperature of T_0, the Noose-Hoover thermostat insures a time-averaged temperature of T_0.

This may seem like a trivial distinction, but the former adds further discontinuity to an already

discretized simulation method. Some other thermostats that have been developed to satisfy the NVT

ensemble are the Anderson [4], Berendsen [5] and Langevin [6] thermostats.

1.3 Barostatting in MD

If a fixed system pressure is desired in addition to fixed temperature, an isobaric-isothermal or NPT

(fixed Number of atoms, Pressure and Temperature) ensemble may be employed. The numerical

approach to adjusting this pressure is called a barostat. This is accomplished by adjusting the size of the

simulation box and, optionally the positions of atoms. This is a more complicated adjustment than

those made by thermostats, as pressure is dependent on the interatomic potential and temperature is

not. Thus, very small adjustments in atomic position can produce large changes in the forces acting on

the atoms, and thus the pressure of the system.

One of the most commonly used barostats, and the one used in this dissertation is the Nose-Hover

Barostat [7]. A NPT ensemble with a Nose-Hoover barostat uses the altered equations of motion

$$\frac{d\mathbf{r}_i}{dt} = \mathbf{v}_i + \eta(\mathbf{r}_i - \mathbf{r}_{cm}); \qquad \frac{d\mathbf{v}_i}{dt} = \frac{\mathbf{f}_i}{m_i} - (\zeta + \eta)\mathbf{v}_i \tag{7}$$

where $\mathbf{r}_{cm}$ is the center of mass of the system and η is the barostat friction coefficient. η and ζ, like the

Nose-Hoover thermostat, are system-wide, time-dependent variables controlled by the differential

equations

$$\frac{d\zeta}{dt} = \frac{1}{t_T{}^2}\left(\frac{T}{T_0} - 1\right); \quad \frac{d\eta}{dt} = \frac{1}{Nk_B T_0 t_P{}^2} V(P - P_0) \tag{8}$$

where t_P is the barostat relaxation time, P_0 is the target pressure. For the case of imposed isotropic

pressure, η, P and P_o may be considered scalars. The simulation box geometry is, in the isotropic case,

controlled by the differential equation

$$\frac{d\mathbf{R}}{dt} = \eta\mathbf{R} \tag{9}$$

where $\mathbf{R}$ is a 3x3 matrix containing the cell edge vectors. For anisotropic pressure conditions P and P_o

may be treated as 3x3 symmetric stress symmetric tensors, necessarily making η a 3x3 symmetric

tensor. The components of P_0 may be set independently, coupled with one another or excluded from

barostating. Also used in MD are the Berendsen [5] and Perinello-Rahmen [8] barostats.

1.4 Boundary Conditions

Spatial boundary conditions describe how atoms near the simulation box edges are treated. The effects

of the very short length scales inherent to atomistic modelling can be partially eased by selecting

periodic boundary conditions. When periodic boundary conditions are employed, atoms can influence

each other across opposite boundaries. If an atom is forced out of the top simulation box, it is placed in

the bottom of the simulation box such that the summed distance between the original and final

positions and the points at which it crossed the top and bottom boundaries conforms to the solution for

the equation of motion for that particle at that timestep. The use of non-periodic boundaries is used to

model surfaces in MD simulations of solids. Periodic boundary surfaces must be parallel and shaped

exactly alike. This is achievable in any parallelepiped-shaped simulation box. Typically, barostating can

only be applied to spatial components that have periodic boundaries. One drawback to using periodic

boundary conditions is that longer ranging effects, like strain fields, caused by nano-scale phenomena,

such as dislocations, can extend across the boundaries. If the simulation box is short enough in a

periodic direction this can cause an artificial change in the magnitude of theses effects.

1.5 Interatomic Potentials

Central to the accuracy of a MD simulation is the interatomic potential which describes the physics of

the interaction between atoms during a simulation. An interatomic potential is a set of equations and

tables of data that describe the potential energy of an atom as a function of its surrounding atoms. The

net force on an atom is calculated, within an MD simulation, as the spatial derivative of the potential

energy. [Maybe discuss some conditions that must be met with potentials]. Potentials can be generated

to replicate several material properties including [give examples and site. Particularly Zimmerman].

These potentials can be separated into two practical groups, pair-wise and many-body potentials. The

difference between the two is subtle, but important. Many-body potentials have an added energetic

dependence on the arrangement of nearest neighbors. This added dependence allows modelling of

complex crystal structures. Simulations using many-body potentials are typically more computationally

expensive than pair-wise potentials. Many such interatomic potentials have been developed. In certain

circumstances multiple potentials can be used in the same simulation.

1.5.1 Pairwise Potentials

Pair-wise potentials calculate an atom's potential energy as the sum of the interaction energies between

every atom in the system with which that atom interacts. These pair interaction energies are

independent of one another. Perhaps the most common pair-wise potential style is known as the

Lennard-Jones (LJ) method[9]. Using LJ, the potential energy of an atom *i* interacting with *n* atoms is

calculated by

$$2E_{p,i} = \sum_{j=1}^{n} E_{p,ij} = \sum_{j=1}^{n} \epsilon \left[\left(\frac{r_m}{r_{ij}} \right)^{12} - \left(\frac{r_m}{r_{ij}} \right)^{6} \right] \tag{10}$$

Here r_{ij} is the interatomic distance. The minimum pair energy will be $-\epsilon$ when $r_{ij}=r_m$. Thus, r_m is the

equilibrium separation distance between two atoms in a vacuum. This method is computationally

inexpensive and effective for modelling liquids and gases [10]. When modelling solids, however, LJ

potentials always favor closer packing, which physical solids do not. HCP is slightly energetically

favorable in LJ over FCC due to its lesser third nearest neighbor distance (if the third nearest neighbor

distance is within the simulation cutoff distance) [11].

Other pairwise potential styles include Reactive Empirical Bond Order (REBO) [12], Beck [13], Born [14],

Buckingham [15], Coulombic interaction and Morse [16] potentials.

1.5.2 Many-Body potentials

Many-body potentials include a secondary dependence on the arrangement of atoms, such that an

atoms energy cannot be calculated as a sum of pair interaction energies. One many-body potential style

is known as the embedded atom method (EAM) [17]. Using EAM, the potential energy of an atom *i*

interacting with *n* atoms is calculated by

$$E_{p,i} = F\left(\sum_{j=1}^{n} \rho(r_{ij}) \right) + \frac{1}{2} \sum_{j=1}^{n} \phi(r_{ij}) \tag{11}$$

Here, the second term is the pair function, which can have the same form as any of the pair-wise

potentials described above. The first term is the embedding function, intended to represent the energy

of an atom in the delocalized electron "cloud" due to its proximity to *n* surrounding atoms. These

functions can take different forms depending on the model. Voter described the electron density at a

distance r from an atom as

$$\rho(r) = r^6(e^{-\beta r} + 2^9 e^{-2\beta r}) \tag{12}$$

where β is an adjustable parameter. This was intended to describe a hydrogenic 4s orbital for modelling

first row transitions metals. It was found to work well as a description for many FCC metals [18]. The

embedding function F is typically a set of piecewise functions, such as a spline, based on a series of

energy calculations from density functional theory (DFT) modelling or fit to optimized certain material

properties [17]. Other many-body potential styles include Tersoff [19], angular dependent (ADP) [20],

Charge-Optimized Many-Body (COMB) [21] and Vashinita [22] potentials.

1.6 Modelling Deformation in MD

During the simulation, a myriad of outside manipulations can be applied, in order to replicate various

environments. These include strain deformation in any tensile or shear component. These adjustments

can be made after every timestep or at some other interval. Any component which is subject to

straining, is typically excluded from barostating. Due to the time restraints discussed [above/below],

deformation rates are often much higher than those applied in experiment. The lowest strain rate used

in this dissertation (in MD simulation) was $3x10^7$/s. By contrast, an experimental tensile test reported in

this dissertation used a strain rate of$3x10^{-7}$/s [23]. Lower strain rates can be used at the expense of

computation time.

1.7 Time/Length restraints of MD

Currently, supercomputers have the capacity to run simulations with millions of atoms for millions of

timesteps, allowing simulations of systems with nanometer length scales for nanosecond time scales.

These are appropriate scales for processes such as dislocation motion, grain boundary motion, the

formation of displacement cascades, shock loading and deformation response in nanograin materials

and thin films. Time dependent processes such as diffusion, creep and cyclic loading are not easily

simulated using MD.

1.8 MD for modelling Particle Dynamics

Molecular dynamics simulation can be extended from point particles to finite sized particles by including

the angular form of Newton's laws of motion in addition to the translational form. This demands that

addition particle properties, including angular displacement (θ), angular velocity (ω) and moment of

inertia (I) be defined. In these simulations, particles can exert on one another both a translational force

(f_1) and a rotational moment (M). The equations of motion in this case become:

$$\frac{d\mathbf{r}_i}{dt} = \mathbf{v}_i \; ; \; \frac{d\mathbf{v}_i}{dt} = \mathbf{a}_i = \frac{\mathbf{f}_{1,i}}{m_i} \; ; \; \frac{d\boldsymbol{\theta}_i}{dt} = \boldsymbol{\omega}_i \; ; \; \frac{d\boldsymbol{\omega}_i}{dt} = \boldsymbol{\alpha}_i = \frac{\mathbf{M}_i}{I_i} \tag{13}$$

Commonly, the bodies are treated as colliding objects with pair forces acting on the point of contact.

This pair force will have a component ($f_{1,ij}$) acting in the direction of the body's center of mass and a

component ($f_{2,ij}$) acting normal to that direction, which contributes to the moment (M_{ij}) via:

$$\mathbf{M}_{ij} = \mathbf{r}_{m,ij} \times \mathbf{f}_{2,ij} \tag{14}$$

where $r_{m,ij}$ is the spatial vector connecting the center of mass of particle i and the point of contact

between particles i and j.

In the simplest three-dimensional case, these bodies would be modeled as spheres of uniform density.

In this case, r_m is always perpendicular to the surface normal. Thus, f_1 is the surface normal force

component at the point of contact and f_2 is the surface tangential force. This allows f_1 to be directly

computed by contact force models such as that by Hertz for fully elastic spheres, and f_2 to be calculated

by coulombic friction.

References

1.   Thompson, A.P., S.J. Plimpton, and W. Mattson, *General formulation of pressure and stress tensor for arbitrary many-body interaction potentials under periodic boundary conditions.* Journal of Chemical Physics, 2009. **131**(15).

2.   Dettmann, C.P. and G.P. Morriss, *Hamiltonian formulation of the Gaussian isokinetic thermostat.* Physical Review E, 1996. **54**(3): p. 2495-2500.

3.   Hoover, W.G., *Canonical Dynamics - Equilibrium Phase-Space Distributions.* Physical Review A, 1985. **31**(3): p. 1695-1697.

4.   Andersen, H.C., *Molecular-Dynamics Simulations at Constant Pressure and-or Temperature.* Journal of Chemical Physics, 1980. **72**(4): p. 2384-2393.

5.   Berendsen, H.J.C., et al., *Molecular-Dynamics with Coupling to an External Bath.* Journal of Chemical Physics, 1984. **81**(8): p. 3684-3690.

6.   Schneider, T. and E. Stoll, *Molecular-Dynamics Study of a 3-Dimensional One-Component Model for Distortive Phase-Transitions.* Physical Review B, 1978. **17**(3): p. 1302-1322.

7.   Martyna, G.J., D.J. Tobias, and M.L. Klein, *Constant-Pressure Molecular-Dynamics Algorithms.* Journal of Chemical Physics, 1994. **101**(5): p. 4177-4189.

8.   Parrinello, M. and A. Rahman, *Polymorphic Transitions in Single-Crystals - a New Molecular-Dynamics Method.* Journal of Applied Physics, 1981. **52**(12): p. 7182-7190.

9.   Jones, J.E., *On the determination of molecular fields - II From the equation of state of a gas.* Proceedings of the Royal Society of London Series a-Containing Papers of a Mathematical and Physical Character, 1924. **106**(738): p. 463-477.

10.   Watanabe, H., N. Ito, and C.K. Hu, *Phase diagram and universality of the Lennard-Jones gas-liquid system.* Journal of Chemical Physics, 2012. **136**(20).

11.   Kihara, T. and S. Koba, *Crystal Structures and Intermolecular Forces of Rare Gases.* Journal of the Physical Society of Japan, 1952. **7**(4): p. 348-354.

12.   Stuart, S.J., A.B. Tutein, and J.A. Harrison, *A reactive potential for hydrocarbons with intermolecular interactions.* Journal of Chemical Physics, 2000. **112**(14): p. 6472-6486.

13.   Beck, D.E., *A New Interatomic Potential Function for Helium.* Molecular Physics, 1968. **14**(4): p. 311-&.

14.   Tosi, M.P., *Cohesion of Ionic Solids in the Born Model.* Solid State Physics, 1964. **16**: p. 1-120.

15.   Buckingham, R.A., *The classical equation of state of gaseous helium, neon and argon.* Proceedings of the Royal Society of London Series a-Mathematical and Physical Sciences, 1938. **168**(A933): p. 264-283.

16.   Morse, P.M., *Diatomic molecules according to the wave mechanics. II. Vibrational levels.* Physical Review, 1929. **34**(1): p. 57-64.

17.   Daw, M.S. and M.I. Baskes, *Embedded-Atom Method - Derivation and Application to Impurities, Surfaces, and Other Defects in Metals.* Physical Review B, 1984. **29**(12): p. 6443-6453.

18.   Voter, A.F., Chen, S.P, *High temperature ordered intermetallic alloys* MRS Symposia Proceedings, 1987. **82**: p. 175.

19.   Tersoff, J., *New Empirical-Approach for the Structure and Energy of Covalent Systems.* Physical Review B, 1988. **37**(12): p. 6991-7000.

20.   Mishin, Y., M.J. Mehl, and D.A. Papaconstantopoulos, *Phase stability in the Fe-Ni system: Investigation by first-principles calculations and atomistic simulations.* Acta Materialia, 2005. **53**(15): p. 4029-4041.

21.   Shan, T.R., et al., *Charge-optimized many-body potential for the hafnium/hafnium oxide system.* Physical Review B, 2010. **81**(12).

22.   Vashishta, P., et al., *Interaction Potential for Sio2 - a Molecular-Dynamics Study of Structural Correlations.* Physical Review B, 1990. **41**(17): p. 12197-12209.

23.   Johnson, D.C., et al., *Quantitative analysis of localized stresses in irradiated stainless steels using high resolution electron backscatter diffraction and molecular dynamics modeling.* Scripta Materialia, 2016. **116**: p. 87-90.

CHAPTER 2: QUANTITATIVE ANALYSIS OF LOCALIZED STRESSES IN IRRADIATED STAINLESS STEELS USING HIGH RESOLUTION ELECTRON BACKSCATTER DIFFRACTION AND MOLECULAR DYNAMICS MODELING

D.C. Johnson[a], Bryan Kuhr[b], D. Farkas[b], G.S. Was[a]

[a]Nuclear Engineering and Radiological Sciences Department, University of Michigan, Ann Arbor, MI, 48109, USA

[b]Materials Science and Engineering Department, Virginia Tech, Blacksburg, VA, 24061, USA

Abstract

Quantitative measurements of stress near dislocation channel–grain boundary (DC-GB) interaction sites were made using High Resolution Electron Backscatter Diffraction (HREBSD) and have been compared with molecular dynamic (MD) simulations. The stress normal to the grain boundary was significantly elevated at discontinuous DC-GB intersections with peak magnitudes roughly an order of magnitude greater than at sites where slip transfer occurred. These results constitute the first measurement of stress amplification at DC-GB intersections and provide support to the theory that high normal stress at the grain boundary may be a key driver for the initiation of irradiation assisted stress corrosion cracks.

Comments

This work was published in the journal Scripta Materialia [1]. It has been lightly edited for formatting.

1.   Johnson, D.C., et al., *Quantitative analysis of localized stresses in irradiated stainless steels using high resolution electron backscatter diffraction and molecular dynamics modeling.* Scripta Materialia, 2016. **116**: p. 87-90.

Austenitic stainless steel is a primary structural material and a candidate for generation IV reactors [1]. Understanding degradation and failure mechanisms in this alloy becomes increasingly important as the nuclear industry pushes the lifetime of current reactors and plans for the construction of new plants. A degradation mode of stainless steels that has been a growing problem for several decades is irradiation assisted stress corrosion cracking (IASCC). Due to the complex nature of dynamic processes during irradiation [2-4], isolating the fundamental mechanisms responsible for component failure by IASCC has been exceedingly difficult. However, in recent years localized deformation has emerged as a potential factor in the IASCC process [5]. The introduction of hard barriers such as dislocation loops, precipitates, and stacking fault tetrahedra (SFTs) under irradiation causes a change in deformation mode from homogeneous slip to localized heterogeneous deformation [6,7]. The first mobile dislocations partially annihilate these barriers [8], leaving a relatively soft region of material compared to the hard matrix. Subsequent dislocations move preferentially in these soft regions, confining a majority of the material deformation within narrow channels.

Jiao et al. [9] showed a strong correlation between the average weighted channel height and IASCC susceptibility. McMurtrey et al. [10] identified two different families of dislocation channel – grain boundary (DC-GB) interaction types: discontinuous channels where the dislocation channel arrested at the grain boundary, and continuous channels where the dislocation channels were transmitted across the grain boundary into the adjacent grain. Cracking propensities for discontinuous DC-GB interaction sites exhibited a greater cracking fraction by a factor of six. The cause of this behavior is believed to be a high local tensile stress due to dislocation pile-up at the head of discontinuous channels. West et al. [11] showed that the inclination angle of cracked boundaries with respect to the loading axis for similar alloys to this study was heavily weighted towards 90 degrees, indicating grain boundary normal stress is an important factor for the crack initiation mechanism. Supporting evidence for this crack initiation

mechanism was provided by Fukuya et al. [12] after investigating 316 stainless steel irradiated to 73 dpa in a fast reactor.

One explanation for the difference in cracking behavior is a difference in the grain boundary normal stress between continuous and discontinuous channels. To date, no quantitative measurements of the stress state near the channel – grain boundary interaction site have been made. Quantitative measurements of residual elastic stress can be made with high spatial resolution using a cross correlation technique developed by Wilkinson, Meaden, and Dingley called High Resolution Electron Backscatter Diffraction (HREBSD) [13]. Kikuchi patterns generated during traditional EBSD analysis will distort when the material is strained. By measuring changes in the Kikuchi pattern, the magnitude of the residual elastic strain can be determined, which can be used to calculate elastic stress. (For a detailed explanation of the technique see [14, 15].) With HREBSD, quantitative stress measurements near discontinuous and continuous channels have been made. The resulting data has been compared and analyzed using molecular dynamic (MD) simulations.

Material used for the study was lab purity stainless steel produced by General Electric Global Research with a nominal composition of 70.36 wt% Fe, 13.41 wt% Cr, 15.04 wt% Ni, 0.016 wt% C, 1.03 wt% Mn, and 0.10 wt% Si that had undergone cold rolling and heat treatment (1200 °C: 2 hr) resulting in a final average grain size of 25 microns. Tensile bars were electrical discharge machine (EDM) cut with a 2mm x 2mm cross section and a 21mm gauge length. Samples were mechanically polished in stages from 320 to 1200 grit SiC paper. Each sample was electropolished for 60-90 seconds using a solution of 10% perchloric acid and 90% methanol at 30 V and -40° C.

Samples were irradiated using 3.2 MeV protons at 360° C to a total dose of 5 dpa with a dose rate of 1.006x10^{-5} dpa/s at the University of Michigan Ion Beam Laboratory (MIBL). Dose was calculated at a depth of 20μm using the quick Kinchin-Pease formulation using the SRIM simulation program [16] and a

displacement energy of 40 eV. Ion irradiated samples were subjected to constant extension rate tensile (CERT) tests at a strain rate of $3x10^{-7}$ s^{-1} to a total plastic strain of 3% in a high purity argon environment at 288 °C.

A LEXT confocal laser microscope and an SEM were used to determine the location and type of formed dislocation channels (discontinuous or continuous). 20 nm colloidal silica was used to remove approximately 200 nm of material from the sample surface, which is the average height of the dislocation channels. EBSD scans using a Phillips XL30 FEG and TSL OIM 5 software were performed near DC-GB intersections over a 400 μm^2 area with a 100 nm step size. Kikuchi patterns collected during scans were analyzed offline with the CrossCourt3 software package developed by BLG Vantage. The cross correlation software was run using 50 ROI's distributed uniformly across the reference pattern and single crystal elasticity coefficients for stainless steel [17]. All points with a calculated mean angular error by the CC3 program above 10^{-3} radians were removed from this analysis due to the large calculation errors for these points.

Stress fields, made by resolving the principle components of the stress tensor onto the grain boundary plane, for both discontinuous and continuous channel – grain boundary interactions are presented in Fig 1. Confocal microscopy shows dark contrast at the location of dislocation channels (Fig 1a). The location of this same region within the SEM is confirmed by overlaying a traditional EBSD orientation map on top of the SEM image, Fig 1b. Surface steps have been removed entirely near DC-GB sites, allowing for high quality EBSD patterns to be collected near the location of dislocation channels. The removal of these surface steps is critical to EBSD pattern generation since their height (up to 600 nm) causes shadowing of the detector, preventing the acquisition of critical information. The green cross in Fig 1b denotes the location where the EBSD pattern (Fig 1c) was collected. Fig 1d shows the stress in the direction normal to the grain boundary as calculated by the CC3 cross correlation software package. The phenomenon of high tensile stress near an intersection site is visible for the three discontinuous channels in Fig 1d

14

(indicated with red arrows). Elevated stress values are localized to the point of DC-GB interaction and then dissipate rapidly over the first few microns into the adjacent grain. Shear stresses were also observable, but at values only ~30% of the tensile stress. Figures 2-1e – 2-1h show the same information for two continuous dislocation channels intersecting a grain boundary. Such a high stress is *not* observed at the continuous DC-GB intersection.
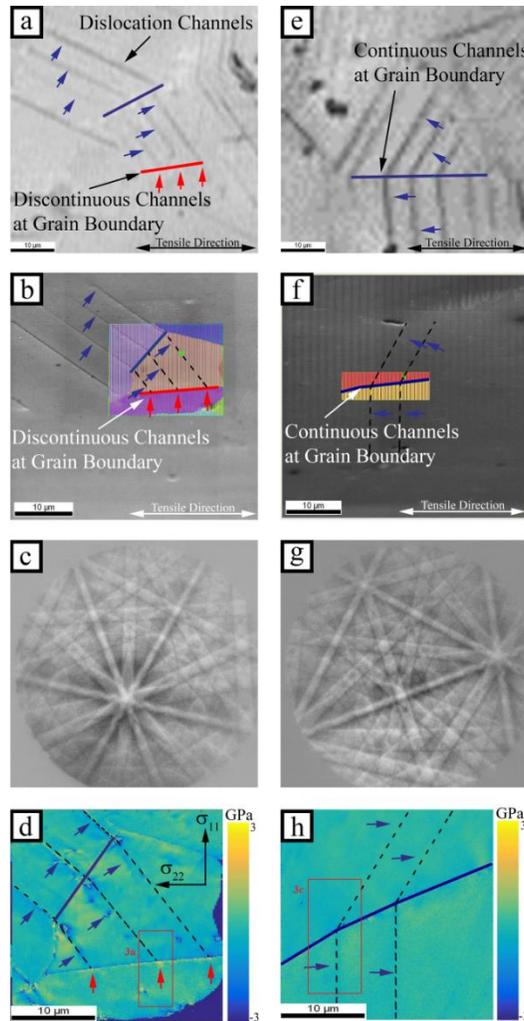
Figure 2-1: Process for generating stress distributions using CC3 for a discontinuous DC-GB intersection. Confocal height profile (a), SEM with EBSD overlay (b), captured EBSD pattern near a channel with green cross showing pattern location (c), and the CC3 calculated GB normal stress distribution for a discontinuous DC-GB intersection (d). Figures e-h show the same progression for a continuous DC-GB intersection. Black dashed lines denote dislocation channel location, blue arrows show dislocation channels which are continuous at the grain boundary, and red arrows show dislocation channels which are discontinuous at the grain boundary intersection site. Red boxes show areas which are expanded for visualization in figure 2-3.

Digital samples were created to match the ones investigated experimentally. The deformation response was modeled using molecular dynamics (MD) and an Embedded Atom Method interatomic potential [10]. Five grains surrounding a specific DC-GB intersection with an average size of 120 nm and the same orientations as in the experimental sample were generated using the Voronoi construction method [18] to form nano-structured thin films with a thickness of 9 nm. Relaxation, deformation, and quenching were simulated using MD with the LAMMPS [19] implementation and the embedded atom method potential for Ni developed by Voter et al [20]. All samples were relaxed for 150 ps to obtain equilibrium grain structure, then strained in tension with a strain rate of 3 x 10^8 s^{-1} and a temperature of 300K using a Nosè Hoover Barostat [21]. All MD was run with periodicity in the x and y directions with free surfaces perpendicular to the z direction. Following increments of 0.5% strain, samples were quenched from 300K to 1K in 50 ps to eliminate remnants of thermal stress. All stress measurements of digital samples reflect post-quench values. The 6-component stress tensor was estimated in LAMMPS as a sum of pairwise forces on each atom and the average volume occupied by a Ni atom in a FCC lattice. Dislocation slip lines were visualized by mapping the volumetric strain of each atom relative to the original, undeformed configuration. This value increases as neighboring atoms move away from one another due to slip, but are unaffected by uniform atomic displacement. Digital samples were visualized in the software package OVITO [22].

Figure 2-2a shows the grain cluster shape and orientation as measured by EBSD and Fig 2b shows the simulated grain cluster. After virtual straining to 5%, Fig 2c shows a GB stress map in the simulated sample with areas of high volumetric strain (>5%) in black. Strain is localized to several bands. Slip band angles with respect to the tensile axis in grains 1 and 2 are the same as shown in Fig 1a. Where the dislocations interact with a grain boundary elevated levels of stress are observed (example highlighted with red arrow in Fig 2c), similar to the experimental measurements. Note that the stresses presented here are translated so they are normal to the 2-3 boundary. These similarities occur despite the fact that

the MD technique is limited to much smaller grain sizes and much faster strain rates than the

experimental ones, and no account is taken for the irradiated microstructure or exact composition of

the sample.
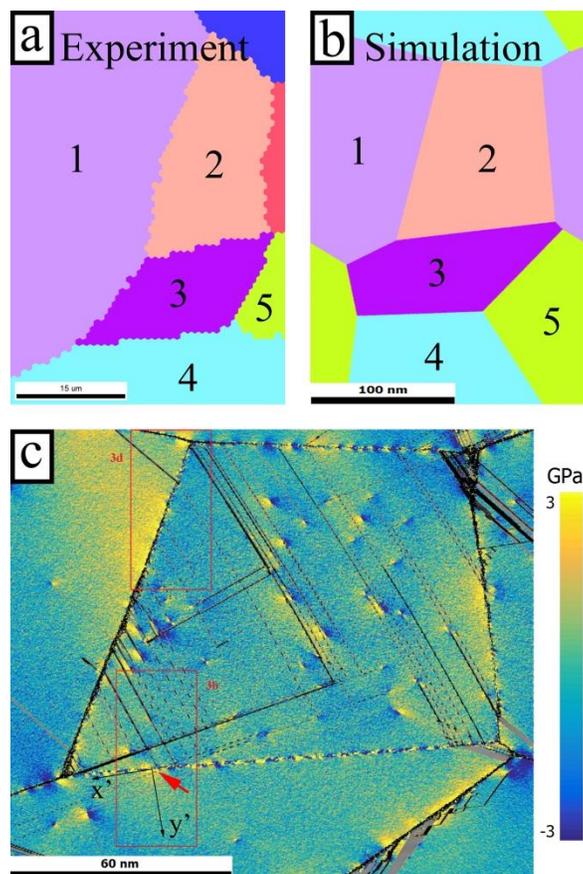
Figure 2-2: Results of 120 nm simulated grains strained virtually to 5% strain. (a) The experimental grain structure, (b) the digital sample, and (c) a resulting GB normal stress map after 5% deformation with dislocation paths overlaid. Black lines denote areas of high volumetric strain. Red arrow highlights region of elevated stress near discontinuous DC-GB interaction. Red boxes show areas which are expanded for visualization in figure 2-3.

Figure 2-3a shows a larger image of the central discontinuous DC-GB intersection in Fig. 1d. Location of

the dislocation channel is marked with a black dashed line. The angle of the grain boundary plane to the

surface is not known, so it was assumed that the grain boundary plane was perpendicular to the sample

surface, making the calculated stress value an upper bound. The peak grain boundary normal stress is

2.78 GPa. This peak value is much larger than the shear stresses observed by Guo et al. [23] at slip band

– grain boundary interaction points in titanium, which ranged from 0.15 to 0.60 GPa. This difference is

likely due to irradiation produced obstacles which prevent dislocation transmission, and allow for larger

dislocation pile-ups. Brief investigation of non-irradiated stainless steel showed heightened stress at

discontinuous slip bands, having stress magnitudes much closer to the titanium case with peak values

ranging from 0.60 to 0.90 GPa. The rotation field, calculated by CC3, ahead of the pile-up is on the order

of 1% which could lead to slightly elevated stress value calculations. The stress field for a simulated

discontinuous channel is presented in Fig 3b. Peak normal stress is 4.75 GPa, and is located at the point

of DC-GB intersection. Elastic constants for the simulated Ni potential are ~20% larger than those of

stainless steel [24], which could contribute to the larger observed stresses in the simulated grains. The

small size of the simulated grains affects the pile-up length and could be influenced by the close

proximity of other grain boundaries.
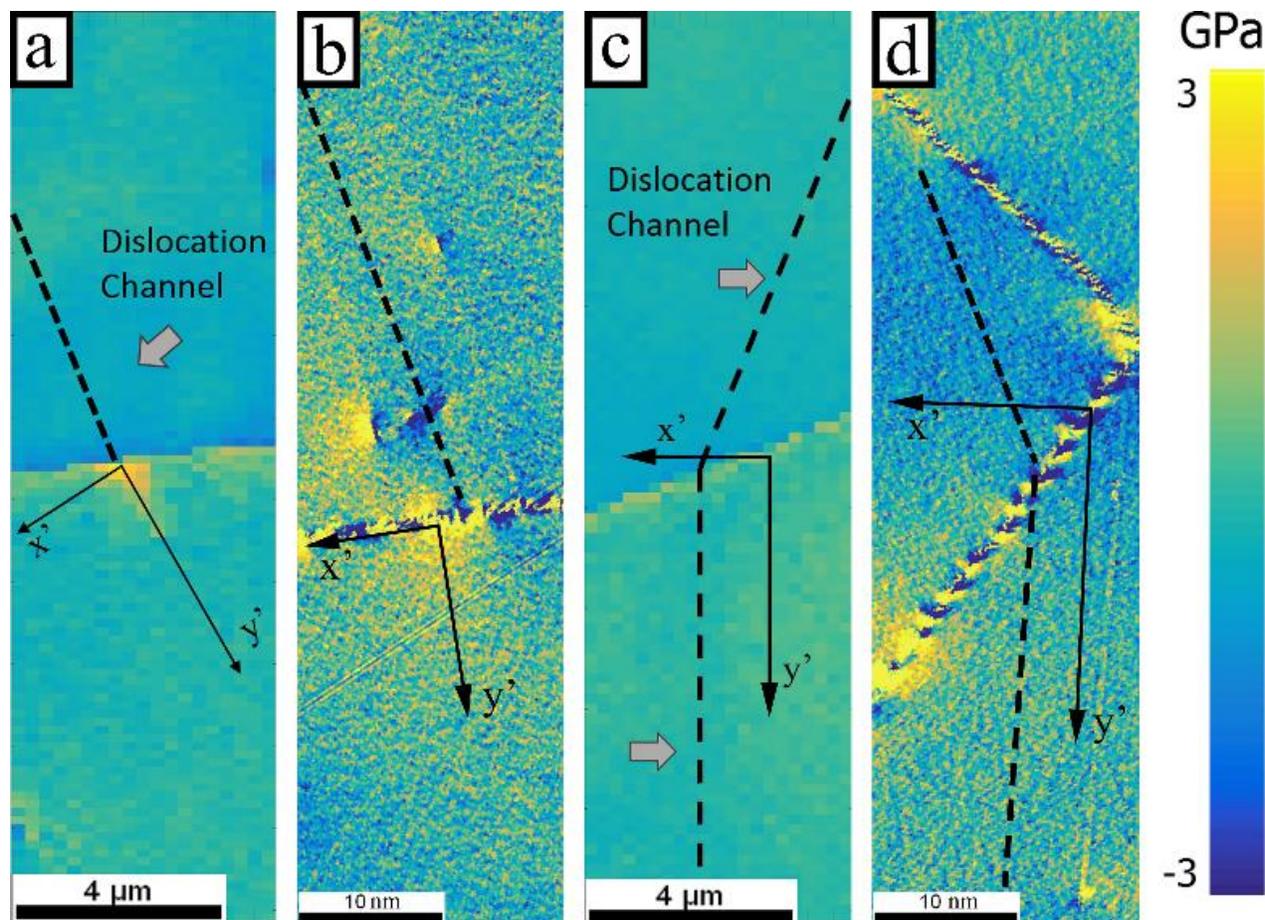
Figure 2-3: Direct comparison of GB normal stress profile near discontinuous DC-GB intersections; a) experiment (taken from figure 2-1d), b) model (taken from figure 2-2c), and near continuous DC-GB intersections; c) experiment (taken from figure 2-1h), d) model (taken from figure 2-2c).

Experimental and simulated continuous DC-GB interaction sites are shown in Fig 2-3c and 2-3d

respectively. The normal stress measured experimentally at the continuous DC-GB interaction point was

0.34 GPa, which is nearly an order of magnitude lower than what is observed in the discontinuous

channel case, and doesn't vary greatly into the adjacent grain. A similar behavior is observed in the MD

simulations. These findings are consistent with a grain boundary normal stress-driven crack initiation

mechanism where the high stress field near discontinuous channels promotes grain boundary cracking.

Theoretical work by Eshelby et al. [25] produced an analytical solution to the pile-up of dislocations at an immovable barrier, similar to the case here in which dislocations within a channel are blocked by a grain boundary. In the Eshelby model, the number of dislocations, *n*, are constrained to lie in the same slip plane under the combined action of their mutual repulsion and the force of an applied stress. The resulting stress field present on the other side of the stationary barrier was found to be closely approximated by $r^{-1/2}$ dependence, where *r* is the distance from the dislocation pile-up. The data was fit with a least squares algorithm to a function of the form:

$$\sigma_N = A + \frac{K}{\sqrt{r + B}} \ [GPa] \qquad\qquad (1)$$

where σ_N denotes the grain boundary normal stress and *K* is the stress intensity factor that describes resistance to slip transfer of this grain boundary. The factor *A* is introduced to allow for uncertainty in the stress state of the selected reference pattern and *B* allows for uncertainty of the exact location of grain boundary beneath the resolving limit of your EBSD step size. This analysis is similar to that performed by Britton et al. [26] on the stress distributions near blocked slip bands at grain boundaries in commercial purity titanium.

A line scan is taken along the y' direction labeled in Figs 3a and 3c. Raw stress data taken along the line scan and curve fittings for both types of DC-GB interactions are plotted in Fig 4a. Initial results show excellent agreement with Eq. (1) for the discontinuous case. The fitting parameters *A*, *B*, and *K* are -0.848 GPa, 0.035 μm, and 1.1995 MPa$\sqrt{m}$ respectively. The flat profile near the continuous DC-GB case could not be fit using Eq. (1). This behavior has also been observed by Guo et al. who saw no elevated stress values near slip transmission sites [23]. Six additional scans have been made near discontinuous

DC-GB interaction sites, and all have exhibited the behavior observed in Fig 3a. Upper and lower bounds have been added to Fig 4a to show the range of these stress profiles. *K* values of scans range from 0.84 to 1.32 MPa$\sqrt{m}$.
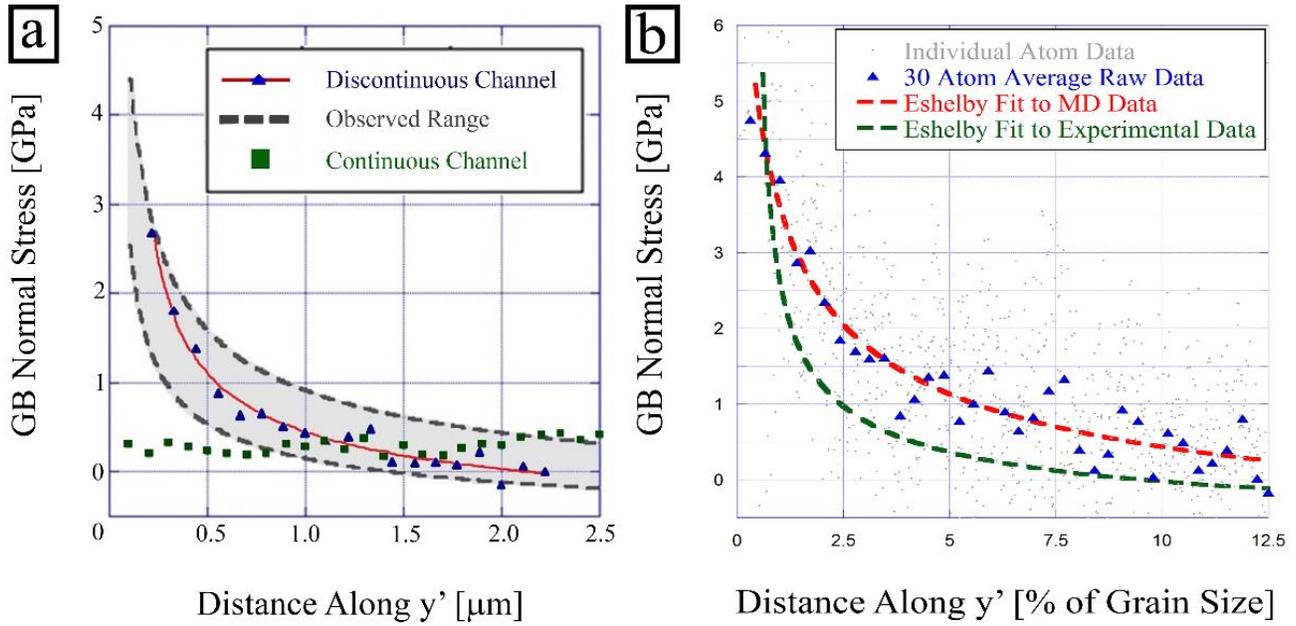
Figure 2-4 Raw data from discontinuous channel stress distribution a) with both Eshelby model curve fit and dashed lines denoting upper and lower bounds for experimentally observed stress values, and raw data from continuous channel stress distribution. b) MD data is compared directly to experimental stress profile data by normalization of the distance from the grain boundary to the grain size.

Simulated stress profiles were similar in shape to experimental profiles on a much smaller length scale. For quantitative comparison, the stress profile along y' in Fig 3b is plotted in Fig 4b as a function of distance from the grain boundary normalized by grain size. 30 atom moving averages were taken as a measurement of the local stress. These average points were then subjected to the same fitting algorithm presented earlier. The simulated data can be fit well using Eq. (1). The curve fit shown in Fig 4 for the experimental data is reproduced here for comparison. Simulation data agrees in both magnitude and shape with the experimental data.

In summary, quantitative stress values have been determined from measurements of the local strains using CC3 near both continuous and discontinuous dislocation channel – grain boundary interaction sites in an irradiated stainless steel. Near the head of a discontinuous channel, a large tensile stress normal to the grain boundary is observed. Similar values have been found through molecular dynamics simulations. The profile of the induced stress plume is consistent with the Eshelby model, and other experimental results published on non-irradiated materials. MD simulation of the same grain cluster analyzed with CC3 also revealed similar high stress normal to the grain boundary that decayed in a manner similar to that from measurement. Stress at continuous DC-GB interaction sites were noticeably lower due to relief of stress by dislocation transmission. All results presented throughout are consistent with a mechanism in which the high GB normal stress drives the initiation of IASCC cracks in the grain boundary.

Acknowlegements

References

1. K.L. Murty, I. Charit, JNM 383 (2008) 189
2. P.R. Okamoto, L.E. Rehn, JNM 83 (1979) 2
3. R.D. Carter, D.L. Damcott, M. Atzmon, G.S. Was, E.A. Kenik, JNM 205 (1993) 361
4. F.A. Garner, M. B. Toloczko, JNM 251 (1997) 252
5. G.S. Was, B. Alexandreanu, J. Busby, Key Engineering Materials 261-263 pt. 2 (2004) 885
6. T. Miura, K. Fujii, K. Fukuya, Y. Ito, JNM 386-388 (2009) 210
7. N Hashimoto, T.S. Byun, JNM 367-370 (2007) 960
8. J.S. Robach, I.M. Robertson, B.D. Wirth, A. Arsenlis, Philosophical Magazine 83 (2003) 955
9. Z. Jiao, G.S. Was, JNM 382 (2008) 203
10. M.D. McMurtrey, G.S. Was, B. Cui, I.M. Robertson, L. Smith, D. Farkas, International Journal of Plasticity 56 (2014) 219

11.   E.A. West, M.D. McMurtrey, Z. Jiao, G. Was, Metallurgical and Materials Transactions A 43 (2012) 136
12.   K. Fukuya, H. Nishioka, K. Fujii, T. Miura, T. Torimaru, JNM 417 (2011) 958
13.   A.J. Wilkinson, G. Meaden, D.J. Dingley, Ultramicroscopy 106 (2006) 307
14.   A.J. Wilkinson, G. Meaden, D.J. Dingley, Mater. Sci. Technol. 22 (2006) 1271
15.   J. Kacher, C. Landon, B.L. Adams, D. Fullwood, Ultramicroscopy 109 (2009) 1148
16.   R.E. Stoller, M. B. Toloczko, G.S. Was, S. Dwaraknath, F.A. Garner, Nuclear Instruments and Methods in Physics Research B 310 (2013) 75
17.   K. Benyelloul, H. Aourag, Computational Materials Science 67 (2013) 353
18.   J. Park, Y. Shibutani, Intermetallics 15 (2007) 187
19.   S. Rawat, V.M. Chavan, M. Warrier, S. Chaturved, S. Sharma, R.J. Patel, AIP Conference Proceedings 1512 (2013) 84
20.   A.F. Voter, S.P. Chen, Characterization of Defects in Materials Symposium 175
21.   G. Bussi, T. Zykova-Timan, M. Parrinello, Journal of Chemical Physics 130 (2009)
22.   A. Stukowski, Modelling and Simulation in Materials Science and Engineering 18 (2010) 015012
23.   Y. Guo, T.B. Britton, A.J. Wilkinson, Acta Materialia 76 (2014) 1
24.   Y.Mishin, D.Farkas, M.J.Mehl, D.A.Papaconstantopoulos, Phys. Rev. B 59 (1999) 3393
25.   J.D. Eshelby, F.C. Frank, F.R.N. Nabarro, Philosophical Magazine 42 (1951) 351
26.   T.B. Britton, A.J. Wilkinson, Acta Materialia 60 (2012) 5773

CHAPTER 3: STRESS LOCALIZATION RESULTING FROM GRAIN BOUNDARY DISLOCATION INTERACTIONS.

Bryan Kuhr[1], Diana Farkas[1], Ian M. Robertson[2], Gary Was[3], Drew Johnson[3]

[1]Department of Materials Science and Engineering, Virginia Polytechnic Institute and State University, 213 Holden Hall 445 Old Turner Street Blacksburg, VA 24061

[2] Department of Materials Science and Engineering, University of Wisconsin, 1415 Engineering Drive, Madison, WI 53706.

[3]Nuclear Engineering and Radiological Sciences Department, University of Michigan, Ann Arbor, MI 48109, USA

Abstract

Large-scale molecular dynamics simulations are used to study strain and stress localization in atomistic polycrystalline FCC digital samples in a thin film configuration, deformed in tension. Special focus is placed on the effects of dislocation-grain boundary intersections. The development of the localized stress and strain regions is studied as dislocations are emitted from and arrive at grain boundaries, it depends on the details of the grain boundary structure and relaxation state. The results are compared with the predictions by continuum theories. Furthermore, the results are compared with experimental measurements of localized stress performed in austenitic stainless steel. Digital samples with two different relaxation states of the grain boundaries but otherwise identical microstructures are compared. The samples with more disordered, less relaxed grain boundaries are found to be more prone to strain and stress localization, with a higher fraction of atoms experiencing extreme deformation.

Comments

This manuscript is in preparation for submission to the International Journal of Plasticity. It is currently being reviewed by its coauthors.

3.1 Introduction

The interaction of dislocations with grain boundaries (GBs) and interfaces impacts deformation mechanisms in metals that can contribute to strengthening [1], crack nucleation [2], and irradiation embrittlement [3]. Yield strength in metals, for instance, is dependent on the local stress intensity that causes slip transfer from one grain to another across a GB [4]. The criteria for slip transfer across an interface is complex, as discussed for example by Kacher et al [5]. The processes that govern slip transfer are affected by the details of the crystallography and relaxation state of in individual grain boundary [6-8].

Some recent studies have included simulations of multiple GB configurations in otherwise identical polycrystals. This technique is instructive both on the effects of additional disorder and as a check on the limitations of the near-perfectly planar boundaries that are typical in atomistic digital samples used in simulation work. Pan and Rupert, used this technique to show how amorphous GB regions can mitigate damage by acting as dislocation sinks [9]. Recent work by Burbery et al. showed that multiple metastable grain boundary structures can be present at otherwise identical GBs and established a correlation between critical resolved shear stress and GB energy and free volume [10, 11]. Tucker and McDowell linked increased GB free volume to lower yield stress due to increased dislocation emission and GB sliding [12]. Foley and Tucker found that equilibrium GB energy is the best predictor for a GB's damage tolerance, as quantified by the ranges of free volume and energy that a boundary can withstand during deformation before failure [13].

A pile up of dislocations against that GB results in strain and stress localization in the pile-up region. For example, stress localization caused by dislocation channeling has been identified as a contributing mechanism to irradiation assisted stress corrosion cracking (IASCC) in polycrystalline FCC metals [14-17]. When dislocation slip is not transferred to the adjacent grain, dislocations pile up in a region of highly localized stress and strain at the intersection [18-24]. As a result of this stress localization, failure tends

to occur via intergranular cracking, leading to the hypothesis that cracks tend to nucleate at the pile up

sites. Stroh estimated that cracking would occur at a pileup of about 1000 dislocations [25]. This is difficult

to confirm experimentally but crack nucleation has been identified at dislocation-GB intersections in MD

simulations [9, 26].

Understanding the evolution of the local stress fields as dislocations arrive and pile up at a grain boundary

is therefore critical. Continuum solutions by Stroh [25] and Eshelby [27] assume that *n* dislocations are

piled up in a channel behind a single locked dislocation and that *n* is a large number. These dislocations

are found to be in force equilibrium when their positions along the channel correspond to the zeroes of

an *n*th order Laguerre polynomial. The further a point in the slip plane is from the pinned point, the

greater the spacing between dislocations. The dislocation concentration in a crystal can be calculated

given the curvature of lattice distortions using the relations established by Nye [28]. Such distortions can

be estimated experimentally using EBSD [29, 30].

The solutions by Stroh and Eshelby [25, 27] present a solution for the stress along a half line originating at

the GB and continuing into the opposite grain. This stress decays from its maximum amplitude at that

pinned location with the inverse root of the distance from the origin. The inverse root dependence of

these solutions has been verified experimentally in high purity titanium by Britton and co-workers [31-33]

and in irradiated austenitic stainless steel by Johnson et al including validation with molecular dynamics

(MD) simulations [34]. The reduced empirical form of this solution is as follows:

$$\sigma = A + \frac{K}{\sqrt{r-B}} \tag{15}$$

where σ is a stress component of interest, and *K* is a parameter with units of stress intensity that is related

to the number and nature of the dislocations in the pile-up. *A* is an additional parameter allowing for

stresses not caused by the pile-up. If there is uncertainty in the exact location of the GB, an additional

parameter *B* may be used as a correction factor. This form is attractive as a fitting equation for experimental stress data because it only has 2 or 3 fitting parameters.

The inverse root dependence described above is not expected to hold when *n* is small. In fact, the Eshelby solution is based on a widely observed and frequently published Elastic Filed Theory (EFT) solution for a single dislocation (*n*=1) wherein the stress has an inverse dependence on the distance from the dislocation core [35, 36]. It is somewhat unclear, then, what dependence the stress will have when the number of dislocations in the pileup (n) is greater than one, but not great enough to mimic the distributions in the Eshelby solution.

Stresses, as calculated via the continuum methods, are not expected to hold in the region near the dislocation core. Webb et al. found that the stresses from atomistic and continuum methods diverge within a 1.5-2nm radius of the core for simulations of an edge dislocation in Al. On the tensile side of a dislocation, the atomistic model predicted a stress peak 0.3-1nm from the dislocation core of roughly 5GPa, which decreases to zero at the core [37]. Elastic Field Theory calculations predict a stress singularity at the core, with the magnitude of at least one stress component approaching infinity as distance from the dislocation core decreases. Webb et al. further concluded that this discrepancy can be accounted for in continuum modeling by the use of the non-local elasticity calculations presented by Erigen [38], with an internal characteristic length of around 0.7nm, corresponding to the distance over which atomic strain in one part of a material can directly-contribute to stress in another.

Dislocation pile-ups against a grain boundary also result in measurable steps where that grain boundary reaches the surface of the sample. The height of these steps is related to the number of dislocations in the pile-up. Surface steps heights as high as 500nm have been observed experimentally by Sharp in irradiated Cu [39] and in irradiated Steel by Jiao and Was [18, 20]. This is in good agreement with continuum crystal plasticity estimations by Patra and McDowell [40]. The height of a surface step is

roughly equal to the surface normal component of summed Burgers vector of the dislocations that have passed through the dislocation channel, which increases as the overall deformation proceeds. The dislocation step height has been linked to crack susceptibility in irradiated steels [20, 41].

The purpose of the present work is to study the evolution of localized stresses due to dislocation grain boundary (GB) intersections in polycrystalline samples. The technique used is atomistic molecular dynamics (MD) using massively parallel resources to understand and follow the detailed evolution of the stress localization process in a representative number of grain boundaries. We report the results from MD simulations with GBs in two different disorder states, and compare the observed stress fields to the predictions from continuum elastic field theory calculations. We also compare the results with experimental studies performed in irradiated austenitic stainless steel.

3.2 Methods:

3.2.1 Digital smaple generation and virtual tensile testing

The procedure described below involves simulated processing of virtual atomistic samples. The Molecular Dynamics computational testing was performed using the LAMMPS implementation [42] with a time step of 1fs and a Noose-Hoover barostat and thermostat [43]. The EAM method [44] was used to describe atomic interactions with the Ni interatomic potential by Voter et al. [45] In all cases, periodic boundary conditions were used in the x- and y- directions and free surfaces were used in z. It is an intrinsic limitation of MD simulation that timescales are shorter than they would be in experiment.

This study was conducted using a 6-grain thin-film polycrystal, with grain boundaries in two different states of disorder. The sample has a grain size of approximately 160nm, a thickness of 10nm and contains about 100 million atoms. The relatively large grain size avoids specific nano-crystalline effects, such as boundary sliding during tensile testing. It also provides and large enough boundary area for analysis. The samples were generated using a Voronoi construction technique [46]. In order to compare the planar

boundaries often used in MD studies of polycrystalline metals to a boundary with a higher degree of disorder, the boundary regions were subject to a local melt and quench procedure.

The first sample, referred to as the room temperature relaxed (RTR) grain boundary sample, was relaxed at 300K for 50ps to allow the boundaries to form relaxed structures. The second sample, referred to as the rapidly solidified (RS) boundary sample, was subject to a local melt around the grain boundaries. To identify grain boundary regions, atoms with a centrosymmetry parameter [47] above 5 and a z-position less than 1nm were chosen to represent a planar section of the boundary. Atoms within a 2.5nm radius in the x-y plane, including those above or below the planar section, were included in the melt region. Atoms in the melt region were allowed to relax for 50ps at 300K. The melt region was then heated to 2000K over 200ps. The region melted at approximately 1700K, as identified by the time vs. energy inflection point. The melt region was then quenched to 300K over 50ps. The entire sample was then allowed to further equilibrate at 300K for 50ps.

After the above described relaxation procedures, both samples underwent virtual strain-controlled tensile deformation at 300K and a strain rate of 3×10^7/s. At strain intervals of 0.2%, snapshots of the strained samples were quenched from 300K to 1K in 50ps. This procedure removes the effects from thermal fluctuations allowing atomic resolution stresses.

3.2.2 Local Stress Measurement via the Eshelby Solution

The GB normal stress $\sigma_{x'}$ was determined for each atom in the vicinity of dislocation-GB intersections using the transformation in equation 2 below.

$$\sigma_{x'} = \frac{\sigma_x + \sigma_y}{2} + \frac{\sigma_x - \sigma_y}{2}\cos2\theta + \tau_{xy}\sin2\theta \qquad (16)$$

where θ is the angle between the x-direction in the simulation and the GB normal (x'). The stress components in the right side of equation 2 were obtained from snapshots of the quenched samples.

Estimating per-atom stress in standard units (GPa) required an estimate of atomic volume. For simplicity, this value was assumed to be a constant 10.9Å^3 across all atoms in both samples. This is equivalent to the average volume of an atom in a perfect FCC lattice with a=3.52Å.

For a dislocation-GB intersection to be included in this analysis, it must: 1) occur in both samples, 2) be discontinuous, 3) include multiple dislocations and 4) occur far enough from a triple junction to avoid unrelated stress fields. For each intersection analyzed, a 25x2x2nm section of the highest tensile stress region on the opposite side of the GB from the dislocation with the length aligned perpendicular to the GB was isolated for stress analysis. The perpendicular distance from the GB along this length is referred to as x' with *x'*=0 at the center of the boundary region. This center is identified by a maximum in the potential energy of atoms in the region and a corresponding increase in the variability of stresses. The atoms in this section with 2 < *x'* < 24nm are considered when fitting the data to the Eshelby stress profile solution. The lower limit was selected to exclude highly variant stresses in the boundary, and the upper limit was selected to exclude effects from stress fields at other boundaries. The Eshelby solution (Eq. 1) is fit to this data via a least square fitting method. This process is repeated for each intersection at axial strain intervals of 0.2% while the intersection remains discontinuous, with no dislocation transmission into the adjacent grain.

3.2.3 Local Stress Estimation via EFT

The stress fields associated with individual dislocations in isotropic materials can be calculated from elastic field theory (EFT). These solutions are widely reported [36]. In this study, they are used to provide estimates of the expected stress due to the dislocations that have arrived at the boundary. This procedure was applied to every intersection, GB type, strain level combination that was reported in the MD results.

For this estimate, the stress field of a single linear dislocation is calculated with a Burgers vector equal to the sum of the Burgers vectors of all the individual dislocations that have arrived at the boundary ($\bar{b}$), and a sense vector (s) that lies along the intersection of the slip plane and the grain boundary plane.

$$\bar{b} = \sum_{i=1}^{n} b_i \tag{17}$$

where n is the number of absorbed dislocations in the intersection. The Burgers vectors of the individual dislocations were identified before they reached the boundary by the crystal analysis tool, also known as the dislocation extraction algorithm (DXA) [48] in the OVITO visualization package [48]. Since edge and screw dislocations have different contributions to the stress field, the burgers vector must be separated into edge and screw components. The screw component is equal to the projection of the Burgers vector onto the sense vector, and the edge component is the difference between the total burgers vector and the screw component.

$$\bar{b}_s = \frac{\bar{b} \cdot s}{|s|^2} s \ , \ \bar{b} = \bar{b}_s + \bar{b}_e \tag{18}$$

In a Cartesian coordinate system with x'' as the direction of the edge component of the burgers vector and the z'' axis along the sense vector, the stresses due to this dislocation, from elastic field theory are

$$\sigma_{x''} = -\frac{G\bar{b}_e}{2\pi(1-v)} \frac{y''\left(3x''^2+y''^2\right)}{\left(x''^2+y''^2\right)}, \ \sigma_{y''} = \frac{G\bar{b}_e}{2\pi(1-v)} \frac{y''\left(x''^2-y''^2\right)}{\left(x''^2+y''^2\right)}, \ \tau_{x''y''} = \frac{G\bar{b}_e}{2\pi(1-v)} \frac{x''(x''^2-y''^2)}{(x''^2+y''^2)} \tag{19}$$

where G is the shear modulus of the surrounding material and v is the Poisson's ratio (79GPa and 0.31 in this case, respectively). For simplicity, anisotropic properties were not considered in EFT calculations. Other non-zero stress components exist in this tensor but they were not considered because the line along which the stress profile was constructed lies in the x''-y'' plane. EFT predicts no stress contribution to $\sigma_{x''}$, $\sigma_{y''}$ or $\tau_{x''y''}$ from the screw component. The GB normal stress was then calculated by the stress transformation

$$\sigma_{x'} = \frac{\sigma_{x''}+\sigma_{y''}}{2} + \frac{\sigma_{x''}-\sigma_{y''}}{2}\cos-2\theta' + \tau_{xy}\sin-2\theta' \tag{20}$$

where θ' is the angle between x' and x''. The x'' and y'' coordinates of this stress profile line are found by

$$x'' - x_0'' = x' \cos \theta' \, , \ y'' - y_0'' = x' \sin \theta' \tag{21}$$

where x_0'' and y_0'' are the points of maximum tensile stress along the GB observed in the MD results.

Plotting $\sigma_{x'}$ as calculated via this continuum method against x' gives a continuum estimation of the stress

profiles measured via MD in this study.

3.2.4 Step Height

Step heights were estimated by the magnitude of the surface normal component of $\bar{b}$. This was verified

by direct measurements in visualization software. Because grain rotation was minimal during

deformation, it was assumed that the surface normal was unchanged. This step height was correlated

with the Eshelby fitting parameter *K*, as an indicator of stress localization.

3.2.5 Visualization

To visualize these samples, a rainbow spectrum color scheme was chosen to represent tensile stress

ranging from -5GPa (blue) to +5GPa (red). In maps where a single GB is of interest the stress in the

direction perpendicular to the boundary is mapped. In maps where several grains are shown, stress in

the direction of axial straining in the sample is mapped. To clearly see both the dislocation channels as

well as the resulting stress fields, all stress maps include a translucent overlay of atoms with high shear

strain slightly darker. This color scheme allows the visualization of both stress and strain localization. The

OVITO visualization software [49] is used for all atomic level visualization.

Atomic shear strain in this work was quantified via the Von Mises shear invariant as introduced by

Simizu et al [50]. This value is a positive unitless scalar calculated from the relative motion of the atoms

nearest neighbors during straining. This type of analysis can be employed in continuum simulations as

well as atomistic simulations and is a very convenient way to identify and visualize slip channels and

areas of highly localized deformation. Atomistic shear strain is calculated in the OVITO visualization

suite [49]. This visualization allowed us to follow the stress localization process in individual boundaries.

As an additional measure of strain localization, the fraction of atoms with extreme levels of shear strain was also tracked as the deformation proceeds.

3.3 Results and Discussion

3.3.1 Overall plasticity

The more disordered RS grain boundary sample was slightly softer in tension than the RTR sample as can be seen in the stress strain curves presented in Figure 3-1. The stress response of the RS sample was lower in both the elastic and plastic regimes. This is likely due, at early strain levels, to an increase in strain accommodation at the GB due to the higher defect density in the GB region. This can be identified in the atomistic shear strain maps in Figure 3-1 by the slightly darker grain boundaries in the RS sample. Intragranular dislocations in the RTR samples are almost all emitted from a triple junction, resulting in relatively few, very distinct slip planes. In the RS sample a majority of the dislocations were also emitted from TJs, but an increase in emission from the boundaries was observed. This difference in the number of dislocation sources could also contribute to the yield strength difference.
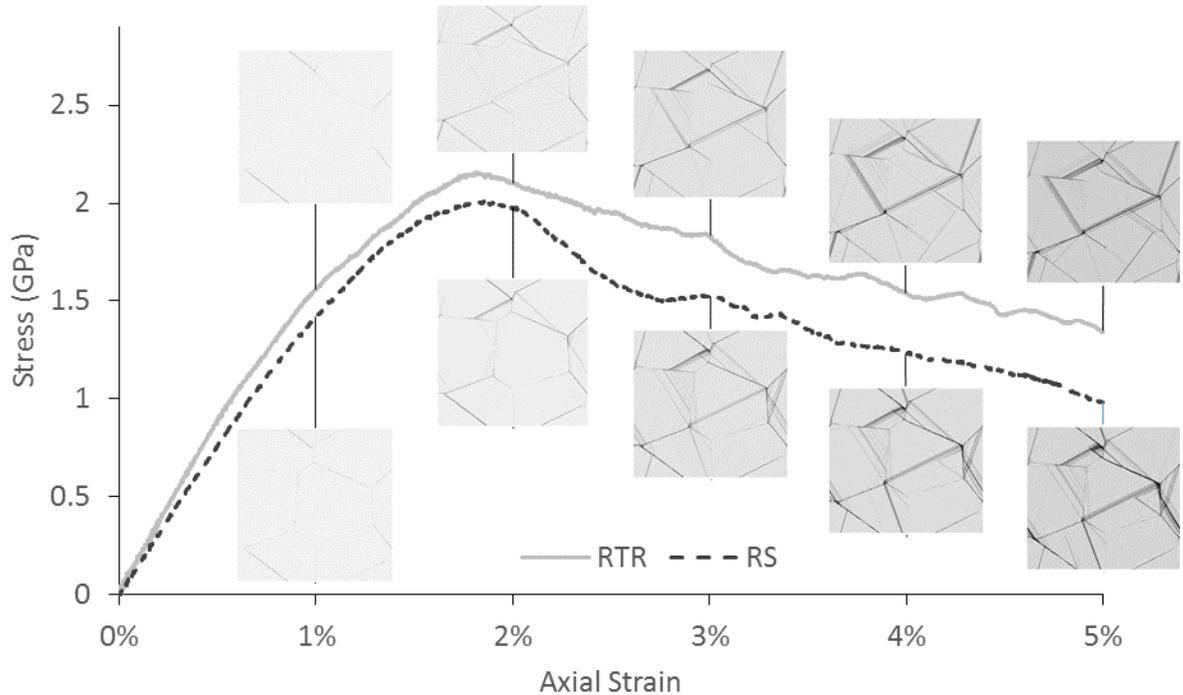
Figure 3-1: Stress-strain curves of samples with RTR and RS relaxation treatments with volumetric strain maps at 1% strain intervals. Maps indicate that most of the bulk crystal plasticity come from dislocations originating at TJs and terminating at GBs. The RS grain boundaries have a slightly increased propensity for dislocation emission and GB accommodation.

3.3.2 Stress Localization in Dislocation-GB Intersections

Three intersections were identified for analysis. One in each of the boundaries between grains 1 and 3, 1 and 5, and 2 and 4. In most cases the Eshelby solution fit was in good agreement with stress profile observed in MD. An example of the individual atom data, a 60 atom rolling average and the Eshelby solution fit are shown in Figure 3-2A. This example corresponds to the intersection at the 1-3 grain boundary in its relaxed state. Other intersections and strain levels had similar levels of scatter. The Eshelby Fit curves obtained for several axial strain levels are shown in Figure 3-2B. This shows how drastically stress is localized at the dislocation-GB intersection. The details of these intersections are discussed in the following three subsections.
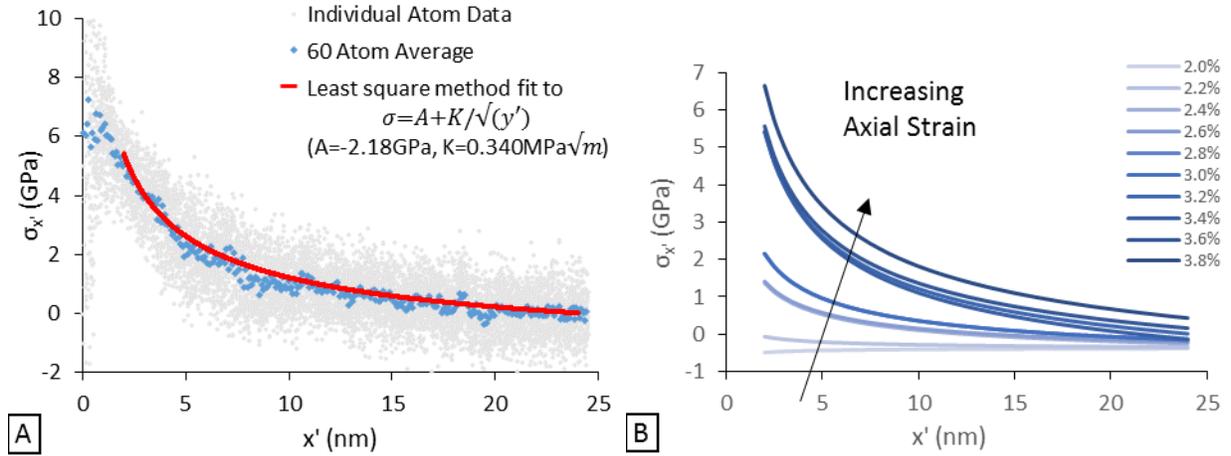
Figure 3-2: Demonstration of localized stress evolution and Eshelby solution fitting procedure for discontinuous DC-GB intersection in boundary RTR1-3. (A) GB normal stress along x' showing individual atom data, 60 atom moving average and Eshelby solution fit to eq. 1 at 3.2% applied axial strain. (B) Eshelby solution fit curves (red line in (A)) at this intersection at several strain levels.

It was observed in the RTR boundaries, that the Eshelby fit parameters *K* and *A* were very small to begin with and scaled roughly linearly with the number of dislocations absorbed in the boundary. This trend was less consistent in the more disordered RS boundaries. This is likely due to stress fields caused by near-boundary dislocations introduced during the rapid solidification process. These fields tended to move during straining. The K parameter, being a measure of stress localization, should rise as more dislocations are absorbed. The A parameter, if taken as an indicator of stress far from the intersection, should not necessarily always decrease with each absorbed dislocation, as it does in these results. For this reason, the A parameter, as reported here, should be regarded as an empirical parameter, which allows for uncertainty of the stress state caused by factors other than the intersection and not a measure of stress far from the intersection.

3.3.2.1 The intersection at GB 1-3

Between axial strains of 2.0 and 3.2% a total of 12 dislocations were emitted from the 3-4-5TJ into grain 3 and stopped at the 1-3 boundary of the RTR sample (Figure 3-3A). Higher strain levels were not considered as slip had transferred to grain 1. A thirteenth dislocation was emitted back into grain 3 from the intersection and arrived in the 3-4-5TJ region. This was included in the analysis, because the

dislocation character was such that the accumulated stress at the boundary was increased by its emission.

With each absorbed dislocation, the Eshelby solution parameter *K* rose by an average of 25.2KPa√m and

A fell by 132MPa. The evolution of *K* and *A* can be seen in Figure 3-3B.
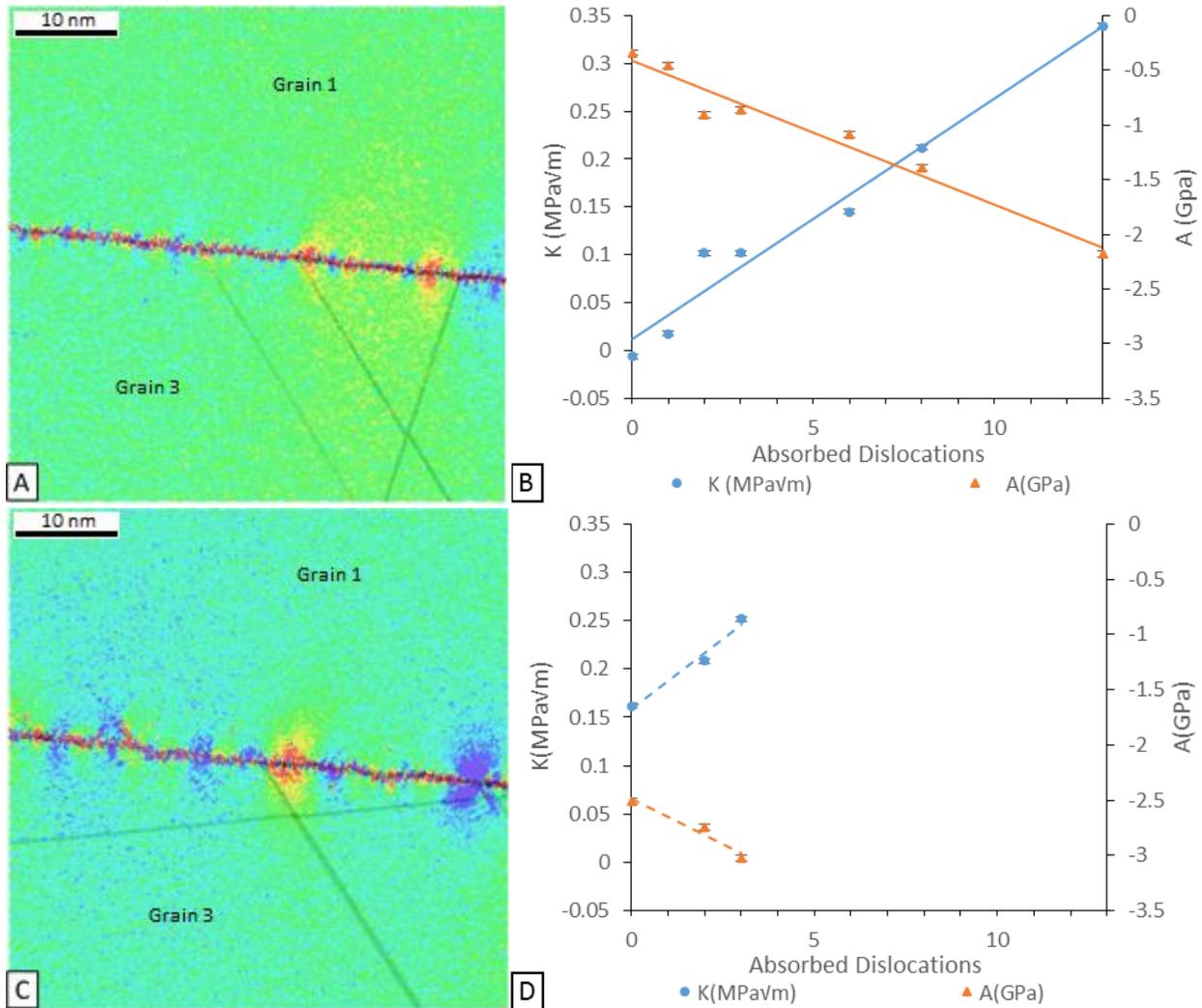
Figure 3-3: Evolution of stress localization due to a discontinuous DC-GB intersection in boundary 1-3. (A) RTR case, GB normal stress map at intersection at 2.6% axial strain with x' axis overlay indicating GB normal direction. (B) Eshelby fit parameters vs absorbed dislocations at DC-GB intersection in A. (C) RS case, GB normal stress map at intersection at 3.6% axial strain. (D) Eshelby fit parameters vs. number of absorbed dislocations in DC-GB intersection in C. Full stress development can be seen in Videos 3-1 (RTR) and 3-2 (RS).

The same slip channel was observed in the more disordered RS sample but only 3 dislocations were absorbed in the boundary by the end of the run. These dislocations occurred between 3.4-3.6% axial strain (Figure 4C). With each absorbed dislocation, the Eshelby solution parameter K rose by an average of 29.1KPa√m and A fell by 164MPa. The evolution of K and A can be seen in Figure 3-3D. The evolution of the Eshelby fit parameters was unique in this case. Where other K values ranged from -10 - 40KPa√m before any dislocations had encountered the boundary, this one began at 150KPa√m. Conversely, other A values began between -0.3 and -0.8GPa, this A value began at -1.5GPa.

The stress maps in Figure 3-3 A and C were taken at axial strain levels where 3 dislocations had encountered the boundary. This provides the most direct comparison between the two levels of boundary disorder for the same boundary crystallography. The more defective RS boundary shows more stress localization after the arrival of the same number of dislocations.

3.3.2.2 The intersection at GB1-5

Between axial strains of 2.0 and 3.0% a total of 5 dislocations were emitted from the 1-2-3TJ into grain 1 and stopped at the 2-4 boundary of the RTR sample (Figure 3-4A). At higher strain levels, additional dislocations arrived at the boundary, but dislocations were emitted from the intersection into grain 5. With each absorbed dislocation, the Eshelby solution parameter K rose by an average of 51KPa√m and A fell by 257MPa. The evolution of K and A can be seen in Figure 3-4B.
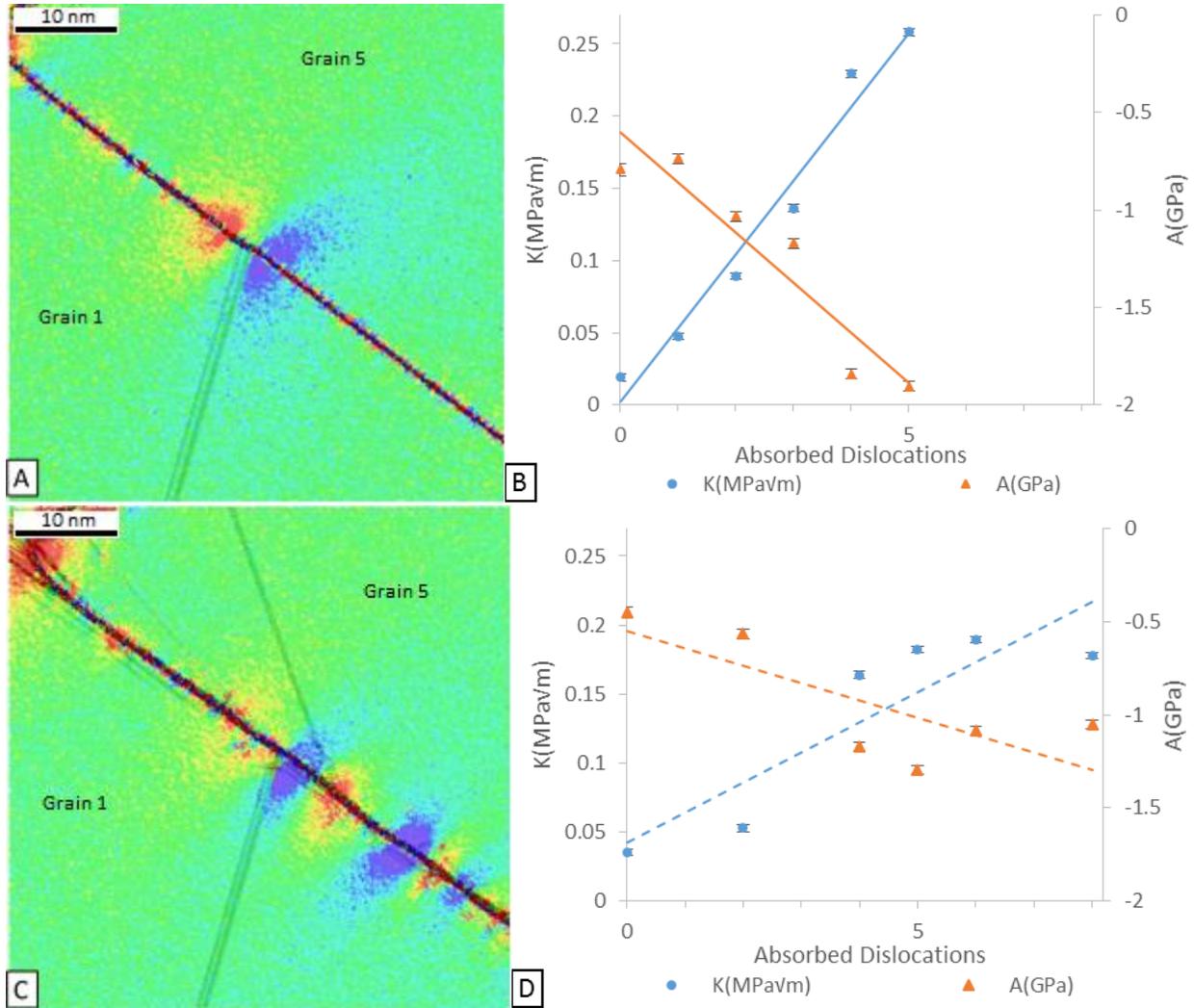
Figure 3-4: Evolution of stress localization due to a discontinuous DC-GB intersection in boundary 1-5. (A) RTR case, GB normal stress map at intersection with x' axis overlay at 3.0% axial strain. (B) Eshelby solution fit parameters for GB normal stress along x' as a function of the number or absorbed dislocations. (C) R case, GB normal stress map at intersection with x' axis overlay at 2.6% axial strain. (D) Eshelby solution fit parameters for GB normal stress along x' vs the number or dislocations absorbed in the boundary. Full stress development can be seen in Videos 3-3 (RTR) and 3-4 (RS).

In the more disordered RS sample, 8 dislocations were absorbed in the boundary between 2.0 and 3.0% axial strain (Figure 5C). With each absorbed dislocation, the Eshelby solution parameter K rose by an average of 21.9KPaVm and *A* fell by 93.1MPa. The evolution of K and A can be seen in Figure 3-4D.

As in Figure 3-3, Figure 3-4A and C each show a boundary type with the same number of absorbed dislocations. In this case 5, dislocation had encountered the boundary. These are the same snapshot as shown in Figures 2 B and C, but viewed from a different orientation. This boundary was unique in that the increase in K with each successive dislocation was, on average, somewhat lower in the more disordered RS sample than the more relaxed RTR sample.

3.3.2.3 The intersection at GB2-4

Between axial strains of 1.0 and 2.8% a total of 14 dislocations were emitted from the 1-2-5TJ into grain 2 and stopped at the 2-4 boundary of the RTR sample (Figure 3-5A). At higher strain levels, no additional dislocations arrived at the boundary. At no point did a dislocation emit from the intersection into grain 4. The stress map at 4.0% axial strain is in Figure 3-5A. With each absorbed dislocation, the Eshelby solution parameter K rose by an average of 10.6KPa√m and *A* fell by 91.4MPa. The evolution of K and A can be seen in Figure 3-5B.
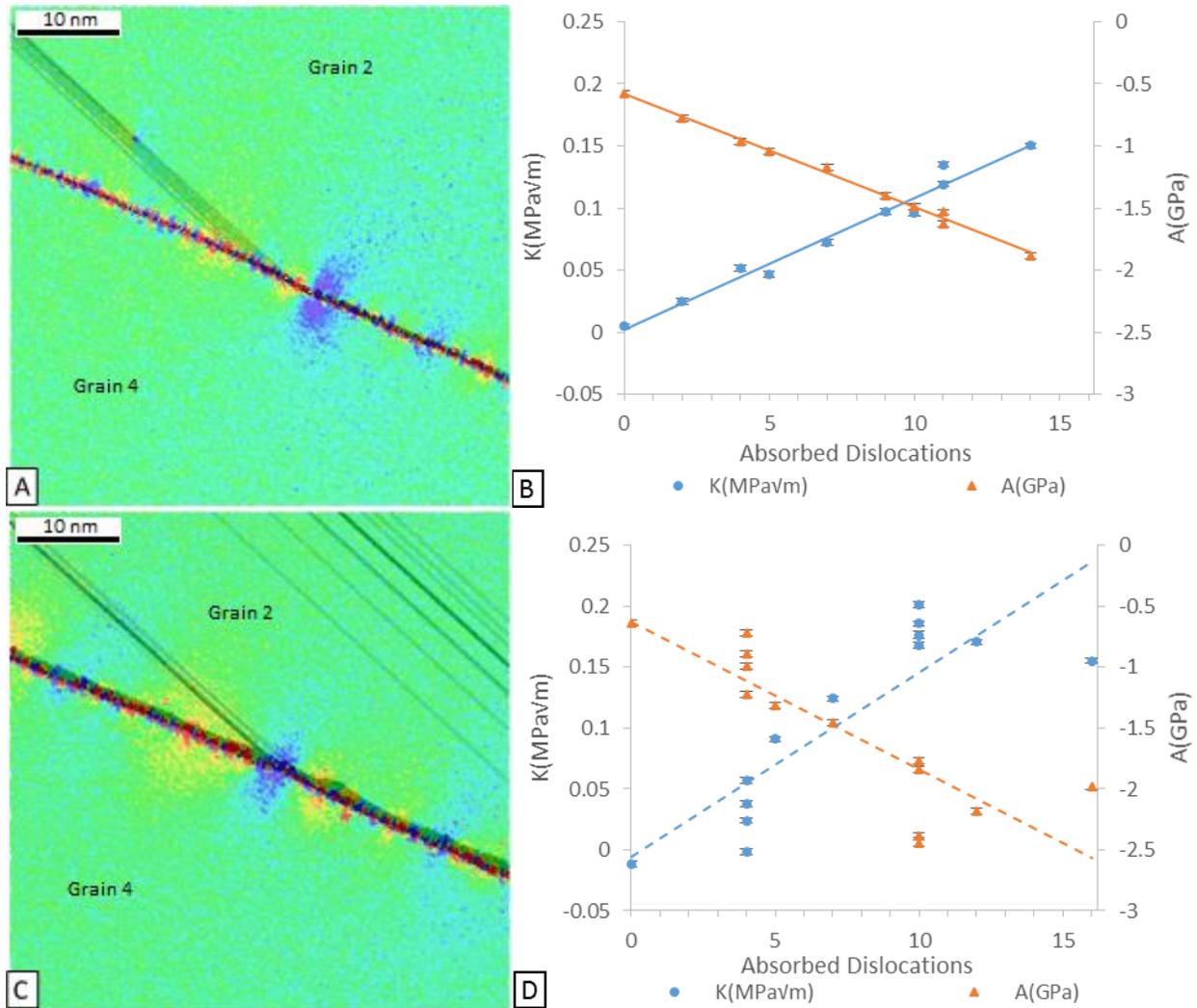
Figure 3-5: Evolution of stress localization due to discontinuous DC-GB intersection in boundary 2-4. (A) RTR case, GB normal stress map at intersection with x' axis overlay at 2.2% axial strain. (B) Eshelby solution fit parameters for GB normal stress along x' as a function of the number or absorbed dislocations. (C) RS case, GB normal stress map at intersection with x' axis overlay at 4.2% axial strain. Note the increased volume of the effected GB region. (D) Eshelby solution fit parameters for GB normal stress along x' as a function of the number or absorbed dislocations. Full stress development can be seen in Videos 3-5 (RTR) and 3-6 (RS).

The same slip channel was observed in the more disordered RS sample (Figure 3-5C). 16 dislocations were absorbed in the boundary between 2.6 and 5.0% axial strain. The stress map at 4.4% is in Figure 3-5C.

With each absorbed dislocation, the Eshelby solution parameter *K* rose by an average of 15.1KPa√m and *A* fell by 121MPa. The evolution of K and A can be seen in Figure 3-5D.

As in Figure 3-3 and 5, Figure 3-5 A and C each show a boundary type with the same number of absorbed

dislocations. In this case 10 dislocations had encountered the boundary.

Figure 3-6 shows the comparison of the Eshelby fit curves for the two different relaxation states of this

boundary, after the arrival of 5 and 10 dislocations. Higher maximum stresses in the region of the

intersection are observed for the more disordered RS boundary than for the relaxed RTR boundary state.
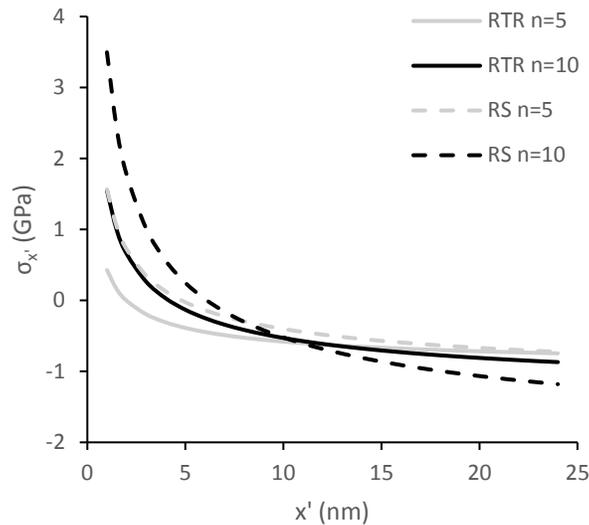
Figure 3-6: Eshelby Solution fit curves for localized stress of a DC-GB intersection at boundary 2-4 for RTR (solid lines) and RS (dashed lines) boundaries after 5 (grey lines) and 10 (black lines) dislocations have encountered the boundary.

3.3.3 Deviation of Stress Localization Behavior from EFT Calculations

Figure 3-7A is an example of GB normal stress ($\sigma_{x'}$) around the dislocation intersection at GB 1-5 from the

EFT calculation in equation 2. In this case, a direct comparison to MD results can be done for both the

RTR and RS samples because, in both cases, 5 dislocations had entered the boundary, and in both cases

the summed Burgers vector of these dislocations was roughly the same. The total edge component ($\bar{b}_e$

from equations 4 and 5) was 0.65nm in the RTR case and 0.63nm in the RS case.
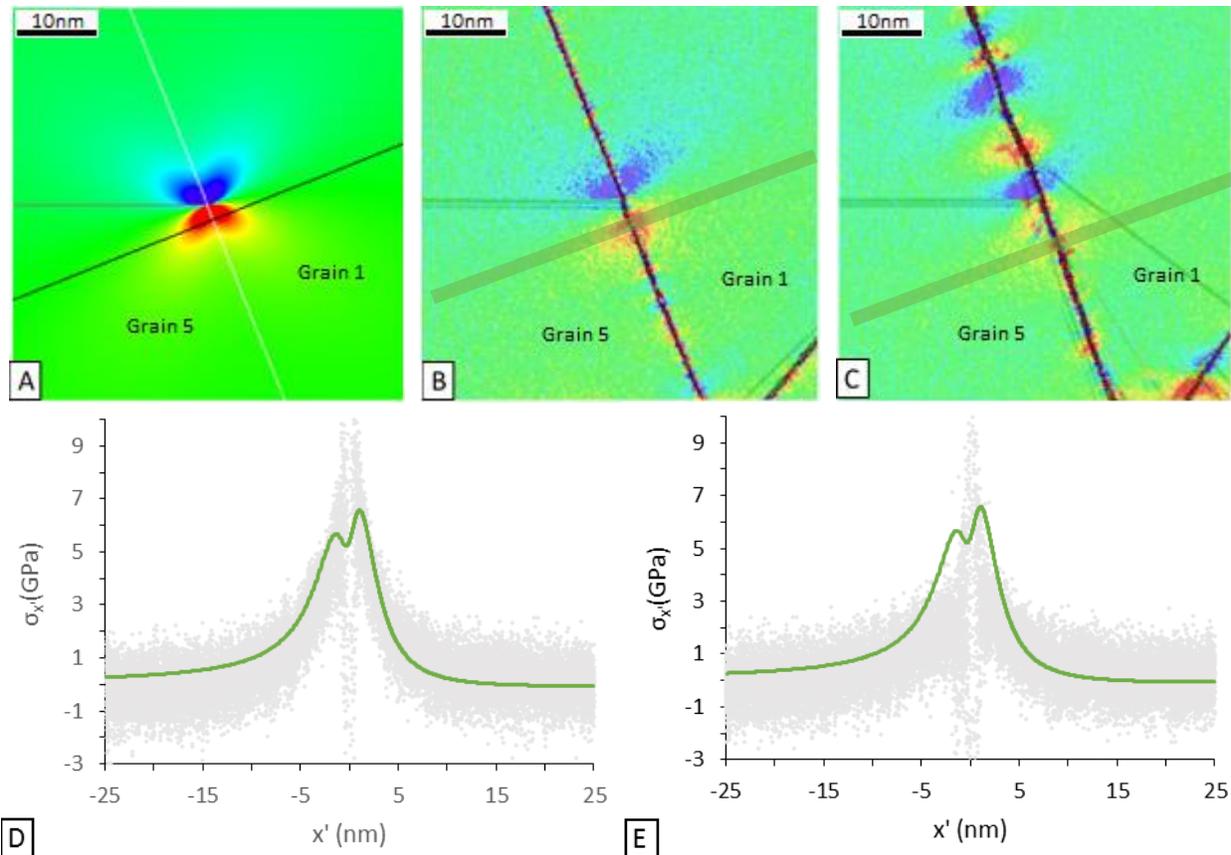
Figure 3-7: GB normal stress maps after 5 Shockley partial dislocations arrive at GB 1-5 as approximated by (A) continuum calculations, (B) MD with RTR boundaries and (C) MD with RS boundaries and RS approximation with indicators of the area sampled in plots of GB normal stress against the GB normal distance from (D) the RTR GB MD simulation with the continuum approximation and (E) RS GB MD simulation. This demonstrates the influence of boundary disorder in the stress state of the boundary. The dislocations that arrived at the boundary are the dominant source of stress in B but not C.

This map is in good qualitative agreement with the stress map of the equivalent stress component from the MD results of the RTR boundary sample pictured in Figure 3-7B, except around the dislocation core and GB region. The agreement is not as good in the more disordered RS case, pictured in Figure 3-7C. The stress data in the highlighted regions of Figure 3-7 A-C is plotted against *x'* in Figure 3-7 D and E.

Both the maximum stress found in the Eshelby solution fit of the MD stress data (occurring at x'=2nm from the boundary) and that from the EFT profile scaled roughly linearly with the number of absorbed dislocations. This is shown in Figure 3-8. On average, each dislocation caused an increase of 0.736, 1.30 and 0.580GPa for the intersections in boundaries 1-3, 1-5 and 2-4 in the EFT calculations; and 0.593, 1.16

and 0.242GPa in the MD simulations. The EFT predicted higher maximum stresses than the MD results

fitted to the Eshelby solution. The difference was found to be more significant as the inclination angle

between the slip plane and the GB decreases. The intersection in GB 2-4 had the lowest angle (26.5°),

followed by 1-3 (57.9°), then 1-5 (70.6°).   Two possible explanations for this correlation are: 1)

Intersections with lower inclination angles cause dislocations from closely-spaced slip planes to be

deposited farther apart on the boundary, thus delocalizing the stress, and 2) slip can more easily be

transferred from the slip plane to the boundary plane if the inclination angle is low. Slip transfer from the

slip plane to the boundary has been observed in experiment and MD simulations [22, 51].
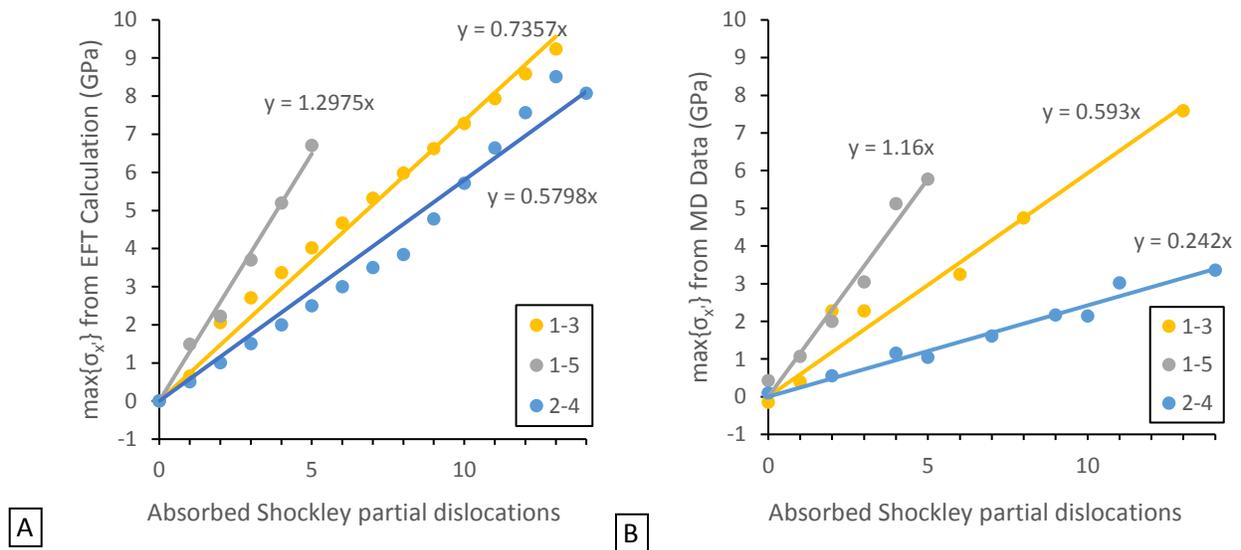
Figure 3-8: Observed maximum stress from Eshelby fit to MD stress data vs. the predicted maximum stress from EFT calculations. This demonstrates how the decreased inclination angle between the slip plane and the grain boundary in the intersection correlate to over prediction of the maximum grain boundary stress. These angles were 57.9°, 70.6° and 26.5° for GBs 1-3, 1-5 and 2-4, respectively.

In either case, a correction for DC-GB inclination angle could improve models for predicting yield stress

and crack nucleation, but the general agreement observed here with the MD results is quite good,

particularly if the grain boundary and the slip plane are close to perpendicular.

3.3.4 Other boundary regions and stress localization

To better understand the differences in the stress states of the relaxed RTR and more disordered RS

boundaries, it is instructive to view regions other than discontinuous DC-GB intersections. Figure 3-9

maps the tensile stress in the direction of axial straining both RTR and RS GB samples. It is apparent that

longer range stress fields exist around the RS boundaries than the RTR boundaries. This is illustrated in

more detail in Figure 3-10. Figure 3-10A and B shows 2 boundaries in the RTR sample. The boundary

region is narrow and the stress fields are short. By comparison, Figure 3-10 C and D show the same

boundaries in their more defective RS state. Here, the boundary region is slightly wider and the stress

fields are longer ranging. Typically, when boundary dislocations are isolated or loosely spaced, they

generated longer ranging stress fields. This has been shown for both extrinsic [52, 53] and intrinsic [54]

dislocations. A similar effect may be at play here due to the additional disorder in the RS boundaries.
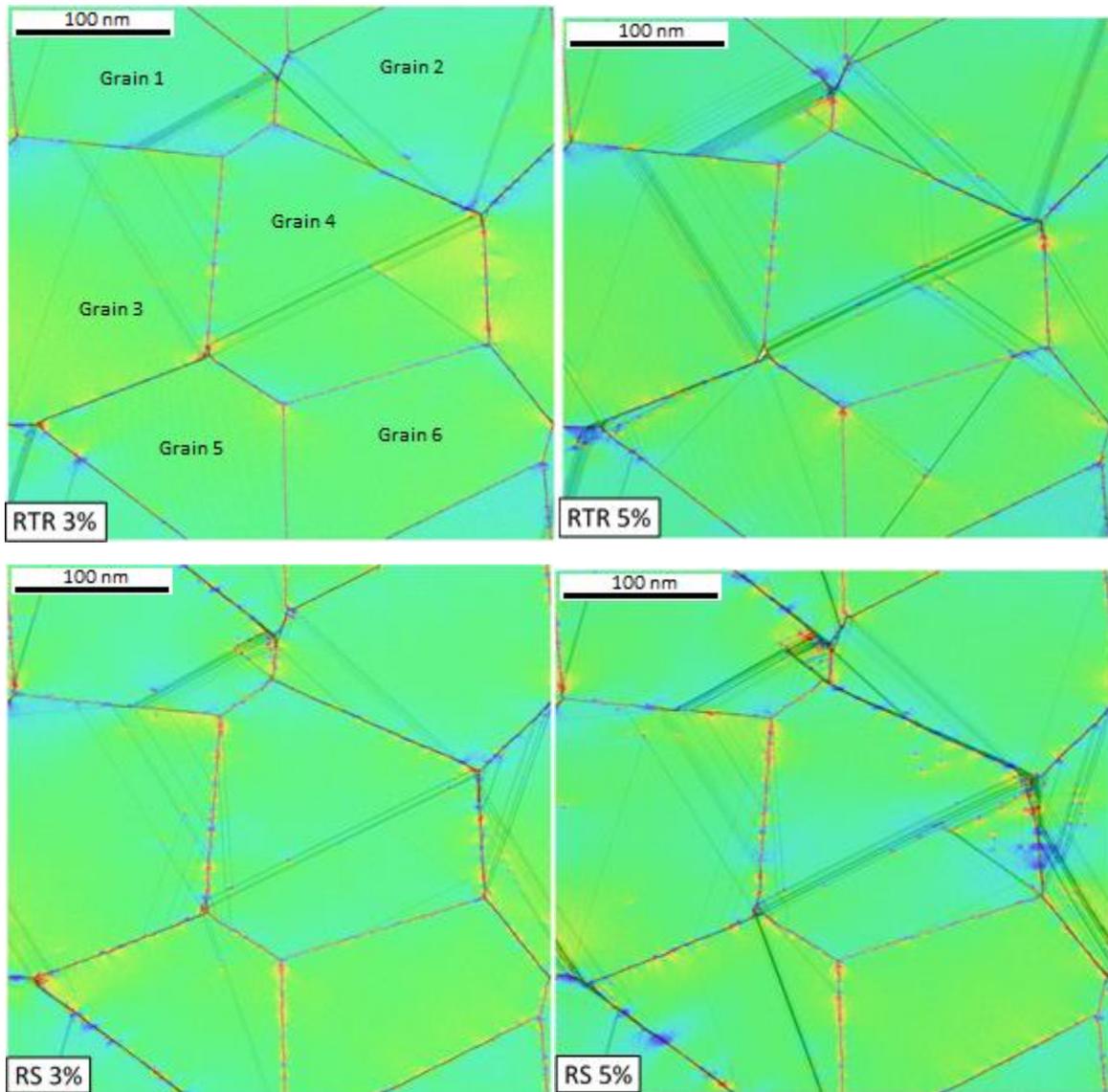
Figure 3-9: Strain and stress localization in the entirety of both samples. This demonstrates stress accumulation at sites of dislocation emission and absorption and TJs where GB sliding has caused an accumulation of strain.
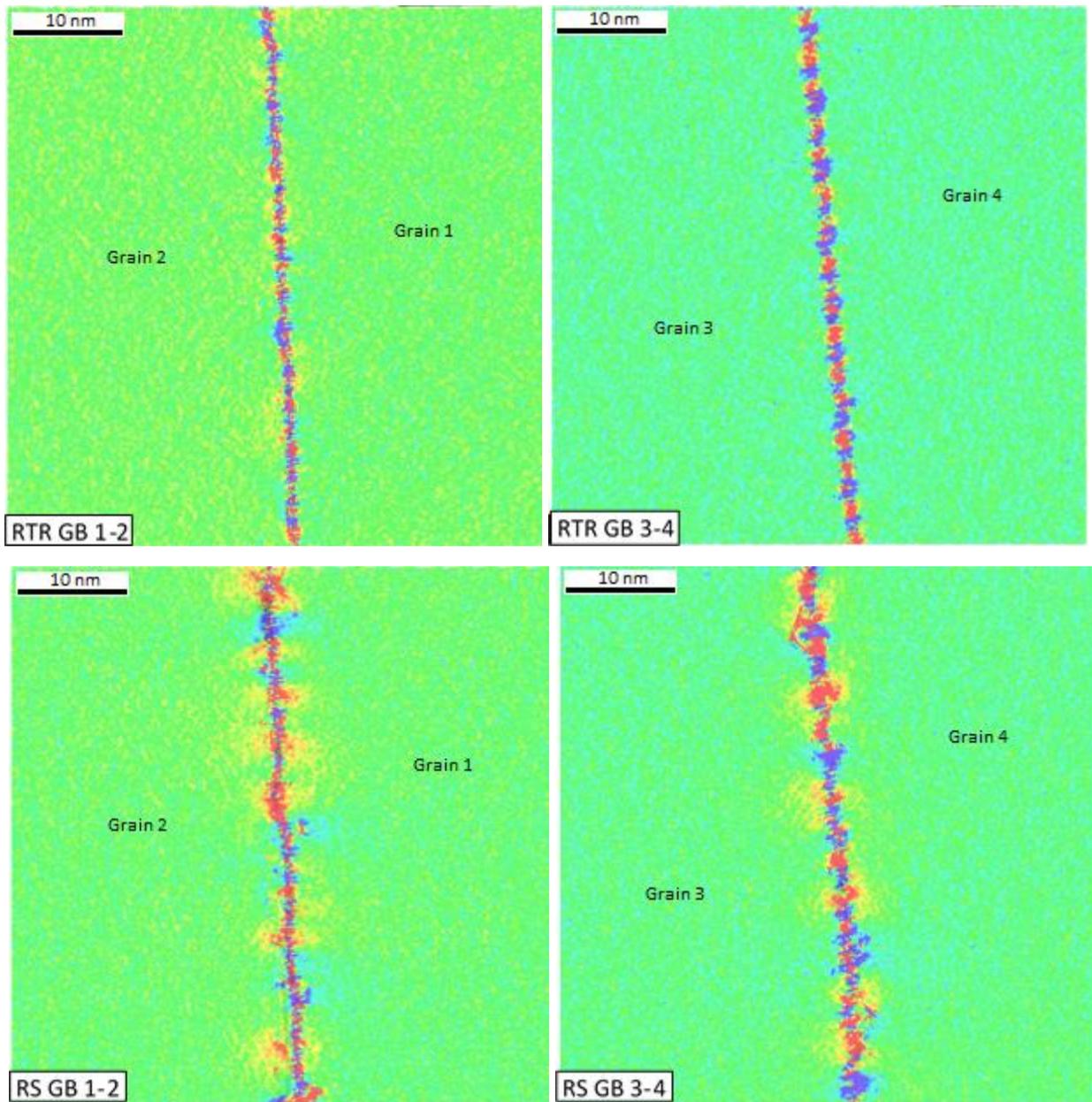
Figure 3-10: Stress map of GBs 1-2 and 3-4 in both GB states at 1.6% strain. This demonstrates the much longer-range stresses present in the RS boundaries.

Figure 3-11 shows stress and strain accumulation in TJ 2-3-4 for both GB relaxation states. There are a few key differences in these two states. In the more disordered RS state, more slip channels have been activated and GB migration has occurred. To better quantify this effect, Figure 3-12 shows the percent of sample atoms with extreme stain levels in both samples as sample straining proceeds. A higher percentage

46

of atoms in the RS sample have extreme values of inelastic shear strain. These results indicate more stress

localization in the case of the RS grain boundaries that present additional disorder.
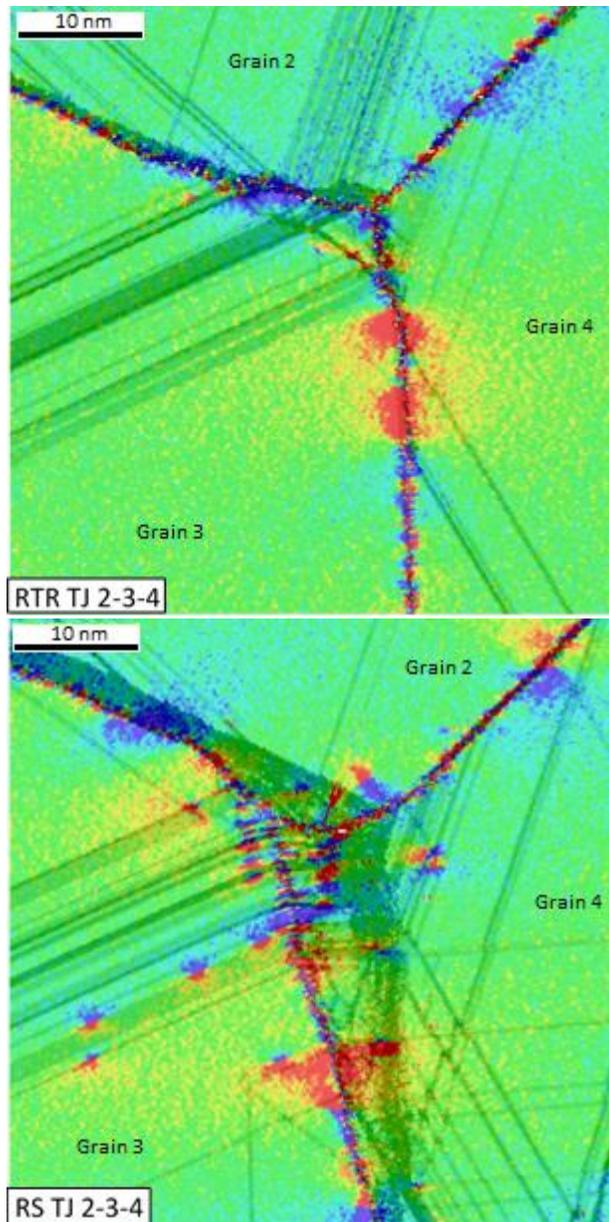
Figure 3-11: Stress and strain localization in triple junction 2-3-4 at 5% axial strain. This demonstrates the increased fraction of high stress and strain atoms in the RS sample. Full stress development can be seen in Videos 3-7 (RTR) and 3-8 (RS).
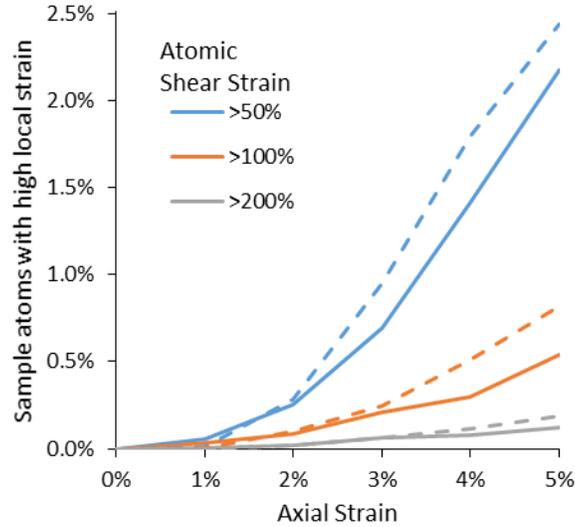
Figure 3-12: Strain Localization quantified by percent of atoms with extreme levels of shear strain. Solid lines indicate percentages in the RTR sample, dotted line indicate the RS sample. This measurement only considers an 8nm slice through the center of the sample, to exclude sample surface atoms. This demonstrates how localized shear straining is intensified in the RS boundaries.

3.3.5 Surface steps caused by the dislocation pile-ups and comparison to experiments

In experimental studies, it is difficult to directly measure the number of dislocations that arrive at a specific

boundary. However, an indirect measurement can be obtained from the height of the step produced at

the intersection of the boundary and the sample surface. This measurement gives the surface normal

component of the total slip in the system. Stresses can also be measured experimentally [34]. We have

measured the step heights in our simulations in order to compare more directly with experiments

performed in irradiated stainless steel. Surface step heights up to 0.94nm were observed in the digital

samples. The largest step was observed in the intersection at RTR 1-3. In all cases, Shockley partial

dislocations with multiple Burgers vectors were observed in each slip channel. This is consistent with

experimental findings that slip channels contain multiple slip systems. In some cases, a leading Shockley

partial dislocation would pass followed by a trailing Shockley partial dislocation in the same plane. In

others, the leading Shockley partial dislocation would be followed by one or more of the same Burgers

vector in adjacent planes, forming a narrow twin. The evolution of the step height depends upon the

48

surface normal component of these vectors. In general, the step heights correlated with increased stress

concentration and larger values of the K parameter in the Eshelby fit. The observed heights are plotted

against the corresponding *K* value from the Eshelby fit of the stress profile ahead of the slip channel in

Figure 3-13. In the intersection at GB 2-4, for instance, the Burgers vectors of the leading and trailing

Shockley partial dislocations had opposite surface normal components leading to very small step heights,

including a low step height outlier of 8×10^{-9}nm (which was omitted from the figure), and a high degree of

scatter in Figure 3-13. A power law fit to this data suggests that K scales roughly with the 0.38 power of

surface step height. Extrapolating this relationship only slightly over-predicts the K values obtained from

EBSD [34], despite substantial differences in method, grain size, local deformation level, and the size of

the sampled area for curve fitting.
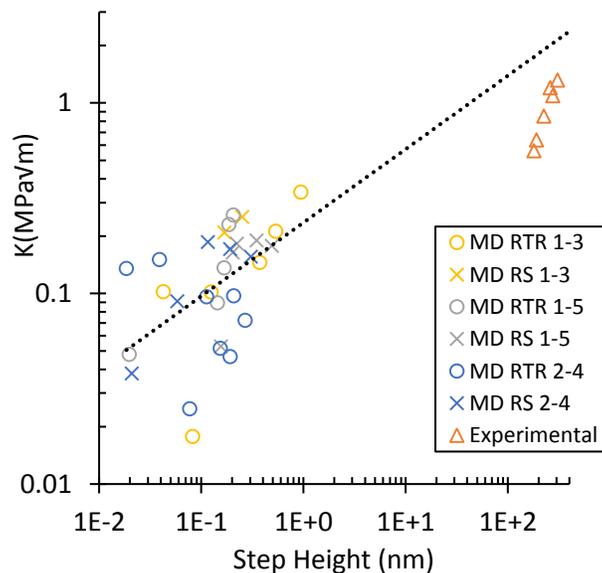
Figure 3-13: Eshelby solution fitting parameter K vs. step height for all discontinuous DC-GB intersections described above with power law fitting equation plus data points from experimental measurements.

3.5 Conclusions

This Molecular Dynamics study revealed the details of local stress states due to the interaction of

dislocations with grain boundaries digital atomistic polycrystals with two different states of boundary

relaxation/disorder.

The local stresses in the discontinuous DC-GB intersections were analyzed by fitting and comparison with continuum solutions. The stress concentration was measured by fitting the MD data to the empirical factor K in the Eshelby solution (eq. 1). It was found that the stress concentration increases roughly linearly with the number of dislocations that arrive at the intersection.

A positive correlation was established between the stress concentration that develops as dislocations arrive at the boundary and the height of the surface step produced by the slip channel. This allows for a comparison with experimental results, despite the differences in grain size and time scales.

The MD results were also compared with the predictions of elastic field theory calculation. The elastic theory predictions agree with simulation results for high-inclination angles between the grain boundary and the slip plane, but somewhat over-predict the stress for lower inclination angles between the slip plane and the GB plane. This is likely due in part to slip transfer from the slip plane to the boundary plane, and in part to delocalization of the stress caused by greater separation between dislocations arriving from adjacent slip planes.

The degrees of stress concentration were also found to depend on the relaxation state of the grain boundary. For most boundaries, the stress concentration was found to be greater when additional grain boundary disorder is present prior to straining. This is relevant to the behavior of irradiated samples, where additional disorder in the boundaries can result from the irradiation. Our results showed that the percentage of atoms that accumulate extreme values of local shear strain, as quantified by the Von Mises shear strain invariant, increases with additional GB disorder.

The relaxation state of the boundary also seemed to have an influence on the possibility of slip transmission across the boundaries. The present work focused on the stress concentration at discontinuous intersections, but we did note that there were a few boundaries (most prominently GB 1-2

but also 2-4 and 1-3 to a lesser extent) that allowed transmission of slip in their relaxed RTR state and not in the more disordered RS state.

Acknowledgements

References

1. Wang, J. and A. Misra, *An overview of interface-dominated deformation mechanisms in metallic multilayers.* Current Opinion in Solid State & Materials Science, 2011. **15**(1): p. 20-28.
2. Stephenson, K.J. and G.S. Was, *The role of dislocation channeling in IASCC initiation of neutron irradiated stainless steel.* Journal of Nuclear Materials, 2016. **481**: p. 214-225.
3. Was, G.S., *Fundamentals of radiation materials science : metals and alloys.* 2007, Berlin ; New York: Springer. xxii, 827 p.
4. Li, J.C.M. and Y.T. Chou, *Role of Dislocations in Flow Stress Grain Size Relationships.* Metallurgical Transactions, 1970. **1**(5): p. 1145-&.
5. Kacher, J., et al., *Dislocation interactions with grain boundaries.* Current Opinion in Solid State & Materials Science, 2014. **18**(4): p. 227-243.
6. Bai, X.M., et al., *Role of atomic structure on grain boundary-defect interactions in Cu.* Physical Review B, 2012. **85**(21).
7. Yu, W.S. and S.P. Shen, *Energetics of point defect interacting with grain boundaries undergone plastic deformations.* International Journal of Plasticity, 2016. **85**: p. 93-109.
8. Adams, B.L., et al., *Taylor theory with microscopic slip transfer conditions.* Iutam Symposium on Multiscale Modeling and Characterization of Elastic-Inelastic Behavior of Engineering Materials, Proceedings, 2004. **114**: p. 315-323.
9. Pan, Z.L. and T.J. Rupert, *Amorphous intergranular films as toughening structural features.* Acta Materialia, 2015. **89**: p. 205-214.
10. Burbery, N.J., R. Das, and W.G. Ferguson, *Modelling with variable atomic structure: Dislocation nucleation from symmetric tilt grain boundaries in aluminium.* Computational Materials Science, 2015. **101**: p. 16-28.
11. Burbery, N.J., R. Das, and W.G. Ferguson, *Transitional grain boundary structures and the influence on thermal, mechanical and energy properties from molecular dynamics simulations.* Acta Materialia, 2016. **108**: p. 355-366.

12.   Tucker, G.J. and D.L. McDowell, *Non-equilibrium grain boundary structure and inelastic deformation using atomistic simulations.* International Journal of Plasticity, 2011. **27**(6): p. 841-857.

13.   Foley, D. and G.J. Tucker, *Quantifying grain boundary damage tolerance with atomistic simulations.* Modelling and Simulation in Materials Science and Engineering, 2016. **24**(7).

14.   Kiritani, M., et al., *Growth of Interstitial Type Dislocation Loops and Vacancy Mobility in Electron-Irradiated Metals.* Journal of the Physical Society of Japan, 1975. **38**(6): p. 1677-1686.

15.   Averback, R.S., *Atomic Displacement Processes in Irradiated Metals.* Journal of Nuclear Materials, 1994. **216**: p. 49-62.

16.   Robach, J.S., et al., *In-situ transmission electron microscopy observations and molecular dynamics simulations of dislocation-defect interactions in ion-irradiated copper.* Philosophical Magazine, 2003. **83**(8): p. 955-967.

17.   Matsukawa, Y., et al., *Mechanisms of stacking fault tetrahedra destruction by gliding dislocations in quenched gold.* Philosophical Magazine, 2008. **88**(4): p. 581-597.

18.   Jiao, Z. and G.S. Was, *Localized deformation and IASCC initiation in austenitic stainless steels.* Journal of Nuclear Materials, 2008. **382**(2–3): p. 203-209.

19.   Farrell, K., T.S. Byun, and N. Hashimoto, *Deformation mode maps for tensile deformation of neutron-irradiated structural alloys.* Journal of Nuclear Materials, 2004. **335**(3): p. 471-486.

20.   Jiao, Z. and G.S. Was, *Impact of localized deformation on IASCC in austenitic stainless steels.* Journal of Nuclear Materials, 2011. **408**(3): p. 246-256.

21.   Tucker, R.P., M.S. Wechsler, and S.M. Ohr, *Dislocation Channeling in Neutron-Irradiated Niobium.* Journal of Applied Physics, 1969. **40**(1): p. 400-&.

22.   McMurtrey, M.D., et al., *Mechanism of dislocation channel-induced irradiation assisted stress corrosion crack initiation in austenitic stainless steel.* Current Opinion in Solid State & Materials Science, 2015. **19**(5): p. 305-314.

23.   Gussev, M.N., K.G. Field, and J.T. Busby, *Deformation localization and dislocation channel dynamics in neutron-irradiated austenitic stainless steels.* Journal of Nuclear Materials, 2015. **460**: p. 139-152.

24.   Byun, T.S. and N. Hashimoto, *Strain Hardening During Mechanical Twinning and Dislocation Channeling in Irradiated 316 Stainless Steels.* Effects of Radiation on Materials: 23rd International Symposium, 2008. **1492**: p. 121-133.

25.   Stroh, A.N., *The Formation of Cracks as a Result of Plastic Flow.* Proceedings of the Royal Society of London Series a-Mathematical and Physical Sciences, 1954. **223**(1154): p. 404-414.

26.   Pan, Z. and T.J. Rupert, *Damage nucleation from repeated dislocation absorption at a grain boundary.* Computational Materials Science, 2014. **93**: p. 206-209.

27.   Eshelby, J.D., F.C. Frank, and F.R.N. Nabarro, *The Equilibrium of Linear Arrays of Dislocations.* Philosophical Magazine, 1951. **42**(327): p. 351-364.

28.   Nye, J.F., *Some Geometrical Relations in Dislocated Crystals.* Acta Metallurgica, 1953. **1**(2): p. 153-162.

29.   Calcagnotto, M., et al., *Orientation gradients and geometrically necessary dislocations in ultrafine grained dual-phase steels studied by 2D and 3D EBSD.* Materials Science and Engineering a-Structural Materials Properties Microstructure and Processing, 2010. **527**(10-11): p. 2738-2746.

30.   Kamaya, M., *Assessment of local deformation using EBSD: Quantification of local damage at grain boundaries.* Materials Characterization, 2012. **66**: p. 56-67.

31.   Guo, Y., T.B. Britton, and A.J. Wilkinson, *Slip band-grain boundary interactions in commercial-purity titanium.* Acta Materialia, 2014. **76**: p. 1-12.

32.   Britton, T.B. and A.J. Wilkinson, *Stress fields and geometrically necessary dislocation density distributions near the head of a blocked slip band.* Acta Materialia, 2012. **60**(16): p. 5773-5782.

33.   Guo, Y., et al., *Measurements of stress fields near a grain boundary: Exploring blocked arrays of dislocations in 3D.* Acta Materialia, 2015. **96**: p. 229-236.

34.   Johnson, D.C., et al., *Quantitative analysis of localized stresses in irradiated stainless steels using high resolution electron backscatter diffraction and molecular dynamics modeling.* Scripta Materialia, 2016. **116**: p. 87-90.

35.   Hull, D. and D.J. Bacon, *Introduction to dislocations*. 3rd ed. International series on materials science and technology. 1984, Oxford Oxfordshire ; New York: Pergamon Press. xiii, 257 p.

36.   Weertman, J., *Dislocation based fracture mechanics*. 1996, Singapore ; River Edge, N.J.: World Scientific. xxiv, 524 p.

37.   Webb, E.B., J.A. Zimmerman, and S.C. Seel, *Reconsideration of continuum thermomechanical quantities in atomic scale simulations.* Mathematics and Mechanics of Solids, 2008. **13**(3-4): p. 221-266.

38.   Eringen, A.C., *Edge Dislocation in Nonlocal Elasticity.* International Journal of Engineering Science, 1977. **15**(3): p. 177-183.

39.   Sharp, J.V., *Deformation of Neutron-Irradiated Copper Single Crystals.* Philosophical Magazine, 1967. **16**(139): p. 77-&.

40.   Patra, A. and D.L. McDowell, *Crystal plasticity investigation of the microstructural factors influencing dislocation channeling in a model irradiated bcc material.* Acta Materialia, 2016. **110**: p. 364-376.

41.   McMurtrey, M.D., et al., *Relationship between localized strain and irradiation assisted stress corrosion cracking in an austenitic alloy.* Materials Science and Engineering a-Structural Materials Properties Microstructure and Processing, 2011. **528**(10-11): p. 3730-3740.

42.   Plimpton, S., *Fast Parallel Algorithms for Short-Range Molecular-Dynamics.* Journal of Computational Physics, 1995. **117**(1): p. 1-19.

43.   Bussi, G., T. Zykova-Timan, and M. Parrinello, *Isothermal-isobaric molecular dynamics using stochastic velocity rescaling.* Journal of Chemical Physics, 2009. **130**(7).

44.   Daw, M.S. and M.I. Baskes, *Embedded-Atom Method - Derivation and Application to Impurities, Surfaces, and Other Defects in Metals.* Physical Review B, 1984. **29**(12): p. 6443-6453.

45.   Voter, A.F., Chen, S.P, *High temperature ordered intermetallic alloys.* MRS Symposia Proceedings, 1987. **82**: p. 175.

46.   Farkas, D., *Atomistic simulations of metallic microstructures.* Current Opinion in Solid State & Materials Science, 2013. **17**(6): p. 284-297.

47.   Kelchner, C.L., S.J. Plimpton, and J.C. Hamilton, *Dislocation nucleation and defect structure during surface indentation.* Physical Review B, 1998. **58**(17): p. 11085-11088.

48.   Stukowski, A. and K. Albe, *Extracting dislocations and non-dislocation crystal defects from atomistic simulation data.* Modelling and Simulation in Materials Science and Engineering, 2010. **18**(8).

49.   Stukowski, A., *Visualization and analysis of atomistic simulation data with OVITO-the Open Visualization Tool.* Modelling and Simulation in Materials Science and Engineering, 2010. **18**(1).

50.   Shimizu, F., S. Ogata, and J. Li, *Theory of shear banding in metallic glasses and molecular dynamics calculations.* Materials Transactions, 2007. **48**(11): p. 2923-2927.

51.   McMurtrey, M.D., et al., *Strain localization at dislocation channel-grain boundary intersections in irradiated stainless steel.* International Journal of Plasticity, 2014. **56**: p. 219-231.

52.   Kinoshita, K., T. Shimokawa, and T. Kinari, *Grain Boundary Structure Dependence of Extrinsic Grain Boundary Dislocation Emission Phenomena: A Molecular Dynamics Study.* Materials Transactions, 2012. **53**(1): p. 147-155.

53.   Shimokawa, T., et al., *Effect of Extrinsic Grain Boundary Dislocations on Mechanical Properties of Ultrafine-Grained Metals by Molecular Dynamics Simulations.* Materials Transactions, 2009. **50**(1): p. 2-10.

54.   van Beers, P.R.M., V.G. Kouznetsova, and M.G.D. Geers, *Grain boundary interfacial plasticity with incorporation of internal structure and energy.* Mechanics of Materials, 2015. **90**: p. 69-82.

CHAPTER 4: DISLOCATION CONTENT IN RANDOM GRAIN BOUNDARIES

Bryan Kuhr[1], Diana Farkas[1], Ian M. Robertson[2], Gary Was[3]

[1]Department of Materials Science and Engineering, Virginia Polytechnic Institute and State University, 213 Holden Hall 445 Old Turner Street Blacksburg, VA 24061

[2] Department of Materials Science and Engineering, University of Wisconsin, 1415 Engineering Drive, Madison, WI 53706.

[3]Nuclear Engineering and Radiological Sciences Department, University of Michigan, Ann Arbor, MI 48109, USA

Abstract

Dislocation content in several random grain boundaries in an FCC polycrystal were determined through

Molecular Dynamics (MD) modeling and the Dislocation Extraction Algorithm (DXA) for detecting lattice

dislocations. This method provides a new means of studying random grain boundaries. Results are

presented for two different grain boundary relaxation states. The first resulting from a conventional

room temperature relaxation procedure and another containing additional disorder resulting from local

melting and rapid solidification in the GB region.   It was found that a large fraction of the boundaries

studied contained significant densities of lattice dislocations as part of their structure, mostly Shockley

partial dislocations and perfect lattice dislocations. The observed dislocation content varied widely

depending on the boundary's specific geometrical parameters and relaxation state and in response to

applied strain. The less relaxed boundaries are thicker, have higher energy and contain more

dislocations than the more relaxed boundaries. The dislocation content changed significantly during

virtual tensile straining of these samples. These results are discussed in the context of the role of the

multiplicity of possible grain boundary structures on the deformation response of polycrystalline

materials.

Comments

This manuscript is in preparation for submission to the International Journal of Plasticity. It is currently being reviewed by its coauthors.

4.1 Introduction

Grain boundaries (GBs) in metals are highly structurally complex, with contributions from grain

orientations, tilt planes, disconnections, and non-equilibrium defect structures. GBs are known to play a

critical role in the overall mechanical deformation of a polycrystal. There exists a complex interplay

between GB defect structures and mechanical deformation, which has been the subject of much

investigation. Detailed simulation studies of grain boundary response to deformation have been

performed mostly for "special" boundaries such as low-angle, symmetrical tilt, twist, coincident site

lattice (CSL), etc. Such studies are useful in understanding many boundary properties including

energetics and some aspects of mechanical response [1].   However, many GBs found in real

polycrystals do not fit in these "special" categories and are labeled "random", "general" or "high-angle"

boundaries. Special GBs appear sporadically throughout general rotations, limiting the direct predictive

capability of many geometric descriptions.

In addition, for each specific GB misorientation and GB plane, there is a multiplicity of possible

structures. This multiplicity of structures needs to be taken into account in order to understand grain

boundary structure and mechanical response [2]. Transformations may occur among these possible

structures akin to phase transformations in the bulk [3]. These have also been referred to as grain

boundary complexions in recent literature [4, 5]. In a recent editorial review, Harmer and Rohrer

describe grain boundary complexion as the "equilibrium structure and chemistry of a grain boundary in

the same way that a 'phase' is an equilibrium state of the bulk" [6]. Defect content, including

dislocation content, is an element of grain boundary complexion.

It has been suggested that amorphous regions exist within or adjacent to randomly oriented grain

boundaries. Tucker et al showed how additional disorder in a GB region, quantified by the additional

free volume associated with the boundary, makes the GB more susceptible to GB sliding and migration

as well as glide dislocation nucleation [7]. Beamish et al showed that disordered solute distributions led

to lower stress thresholds for grain boundary sliding in Fe-Ni bicrystals [8]. In a recent MD study, Pan and Rupert showed the effects of amorphous boundaries by melting then re-solidifying regions around grain boundaries [9].

GB models which use defect content as a descriptor include the Structural Unit model [10] and the Read-Shockley model [11]. Defect structures in low angle boundaries can be described in detail by the Read-Shockley model. As the misorientation angle of adjacent grains increases, the dislocation spacing in the GBs decreases, often causing them to combine or making them indistinguishable. This presents a challenge when attempting to describe a random GBs defect structure. In some cases, dislocation densities can be experimentally determined using TEM [12], and compared directly to numerical solutions like the Frank-Bilby equation (FBE) [13, 14] . Such solutions for GB dislocation content have proven useful in finite-element crystal plasticity modeling of deformation in polycrystalline metals such as the model developed by Rezvanian et al [15]. In a simple form, FBE can be used to calculate the summed Burgers vectors of dislocations crossed by any vector in an interface plane given the orientations of both grain's lattices. FBE does not give an indication of the Burgers vector of the individual dislocations. These limitations are discussed further by Sutton and Baluffi [16]. Trying to overcome some of these limitations Wang et al utilized what they call an "atomistically-informed" FBE approach [17, 18].

Grain boundaries have been recognized for years to contain both intrinsic and extrinsic boundary dislocations. Intrinsic boundary dislocations are the geometrically necessary dislocations that appear in a regular pattern on a planar boundary to accommodate the misorientation of two adjacent crystals. In addition, grain boundaries can contain extrinsic GB dislocations which interrupt the regular pattern of intrinsic dislocations and the planar geometry of the boundary, resulting in grain boundary ledges.

The detailed local structure of GBs has been shown to effect several deformation processes including GB strain accommodation. Recent studies have linked the dislocation content within a boundary to GB migration [19, 20], GB sliding [21, 22] [23], GB rotation[24], dislocation emission [25, 26]. Intrinsic GB dislocations in austenite act as preferential sites for martensite nucleation [27]. Some have linked these effects to the presence of GB ledges, created by excessive extrinsic dislocations [28, 29]. A review by Bieler et al showed the link between GB character and crack nucleation in metals [30]. GB strain accommodation can also be influenced by solute segregation [31]. A GBs propensity to emit dislocations during plastic deformation is critical in the process of plastic deformation [32].

Dislocations encountering a GB can have direct and indirect effects on the GB structure and the surrounding microstructure. Hirth et al. described the direct effects in a recent publication [33]. Indirect effects include changes to grain boundary character twin nucleation [34] and the formation of stress fields which shield further dislocation absorption [35]. The defect structure of a boundary has also been shown to affect the ability of slip to transmit slip across grains. Bieler et al reviewed these effects in Ta and Ti as characterized by SEM and crystal plasticity modeling [36].

Detailed understanding of dislocation content in general grain boundaries is therefore important for understanding mechanical response. The purpose of the present paper is twofold: 1. to look at grain boundary structure in a novel way that focuses on the dislocation content of random general boundaries and 2. to study the specific grain boundary state of disordered grain boundaries. We utilize the formalism of the Dislocation Extraction Algorithm (DXA) [37]. Dislocation content was characterized qualitatively and quantitatively before and during virtual tensile straining. This method gives an estimate of GB dislocation content in random boundaries with no assumptions from continuum calculations. The goal is to provide a statistical quantification of the dislocations contained in general random grain boundary structures. 15 randomly oriented boundaries in a digital atomistic sample are studied. In order to address the role of the multiplicity of possible structures we consider two different

relaxation states for each grain boundary, one significantly more disordered and less relaxed than the other. The following sections detail the procedure used in this study, show the effects of relaxation state on GB energy, thickness and dislocation content and finally discuss the effects of applied strain.

4.2 Simulation Procedure

4.2.1 Sample Generation and Relaxation

This study was conducted using a 6-grain thin-film polycrystal, with grain boundaries in two different states of disorder. The sample has a grain diameter of roughly 160nm and a thickness of 10nm and contains about 100 million atoms. This grain size is relatively large for atomistic simulation and has a number of advantages for the current work, including minimization of nano-size effects, such as boundary sliding during tensile testing, and larger boundary area for statistical analysis of defect concentration. The samples were generated using a standard Voronoi construction technique [32]. The sample was then subject to relaxation at room temperature for 50 ps, using the LAMMPS MD implementation [38] with a timestep of 1fs and a Noose-Hoover barostat and thermostat [39]. An EAM (Embedded Atom Method) [40] interatomic potential was used for all MD simulations , namely the Ni potential by Voter et al. [41]. In all cases, periodic boundary conditions were used in the x- and y-directions (horizontal and vertical to the page in figure 4-1) and free surfaces were used in z (out of the page in figure 4-1). It is an intrinsic limitation of MD simulation that timescales are much shorter than those used experimentally. This sample is termed the RTR sample, for its room temperature relaxation treatment.
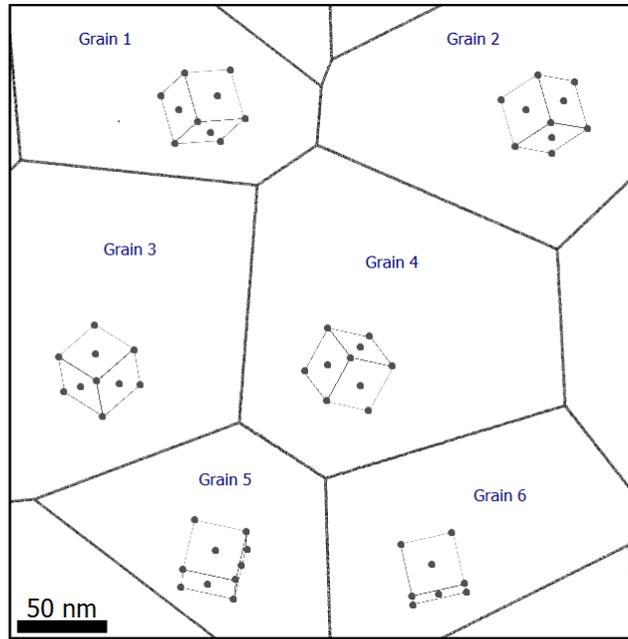
Figure 4-1: Microstructure of sample under investigation with grain orientation indicators

Table 4-1: Orientation of the FCC <100> directions of the 6 grains of the investigated sample in lattice units

Grain	[100]	[010]	[001]
1	(0.87, 0.05, -0.49)	(-0.24, 0.91, -0.33)	(0.43, 0.40, 0.81)
2	(0.68, -0.13, -0.72)	(-0.25, 0.88, -0.40)	(0.68, 0.45, 0.57)
3	(0.71, -0.47, 0.51)	(0.69, 0.60, -0.41)	(-0.11, 0.64, 0.76)
4	(0.80, -0.17,- 0.58)	(0.44, 0.82, 0.37)	(0.41, -0.55, 0.73)
5	(0.98, -0.20, 0.03)	(0.20, 0.92, -0.34)	(0.03, 0.34, 0.94)
6	(0.97, 0.23, 0.00)	(-0.22, 0.96, -0.15)	(-0.03, 0.15, 0.99)

In order to compare these relaxed boundaries with boundaries containing a higher degree of disorder, a second sample was created with exactly the same geometry and grain misorientations but with the boundary regions subject to a local melt and quench procedure that introduced a larger degree of disorder to the boundary structure. This second sample is referred to as the RS sample, for its rapid solidification treatment of the region around the grain boundaries.

Figure 2 shows the procedure used for the creation of the RS digital sample. Grain boundary regions were identified by atoms with a centro-symmetry parameter [42] above 5 and a z-position less than 1nm

were chosen to locate the position of the boundary. All atoms within a 2.5nm radius in the x-y plane

were included in the melt region. Atoms in the melt region were allowed to relax for 50ps at 300K and

then heated to 2000K over 200ps. The region melted at approximately 1700K, as identified by the

inflection point in the time vs. energy curve in figure 4-2A. The melt region was then quenched to 300K

over 50ps. The entire sample was then allowed to equilibrate at 300K for 50ps. At the conclusion of the

melting and quenching sequence, it was found that 1036850 (1.17%) atoms in an 8nm slice through

center of the RS boundary sample had a centro-symmetry parameter above 3 as opposed to 482073

(0.54%) in the RTR boundary sample. This verifies that additional disorder was introduced into the RS

sample. A histogram of the centro-symmetry parameter of atoms contained in both samples is shown in

figure 4-3. The 8nm slice was taken to exclude near-surface atoms, which have a wide range of

centrosymmetry parameters.
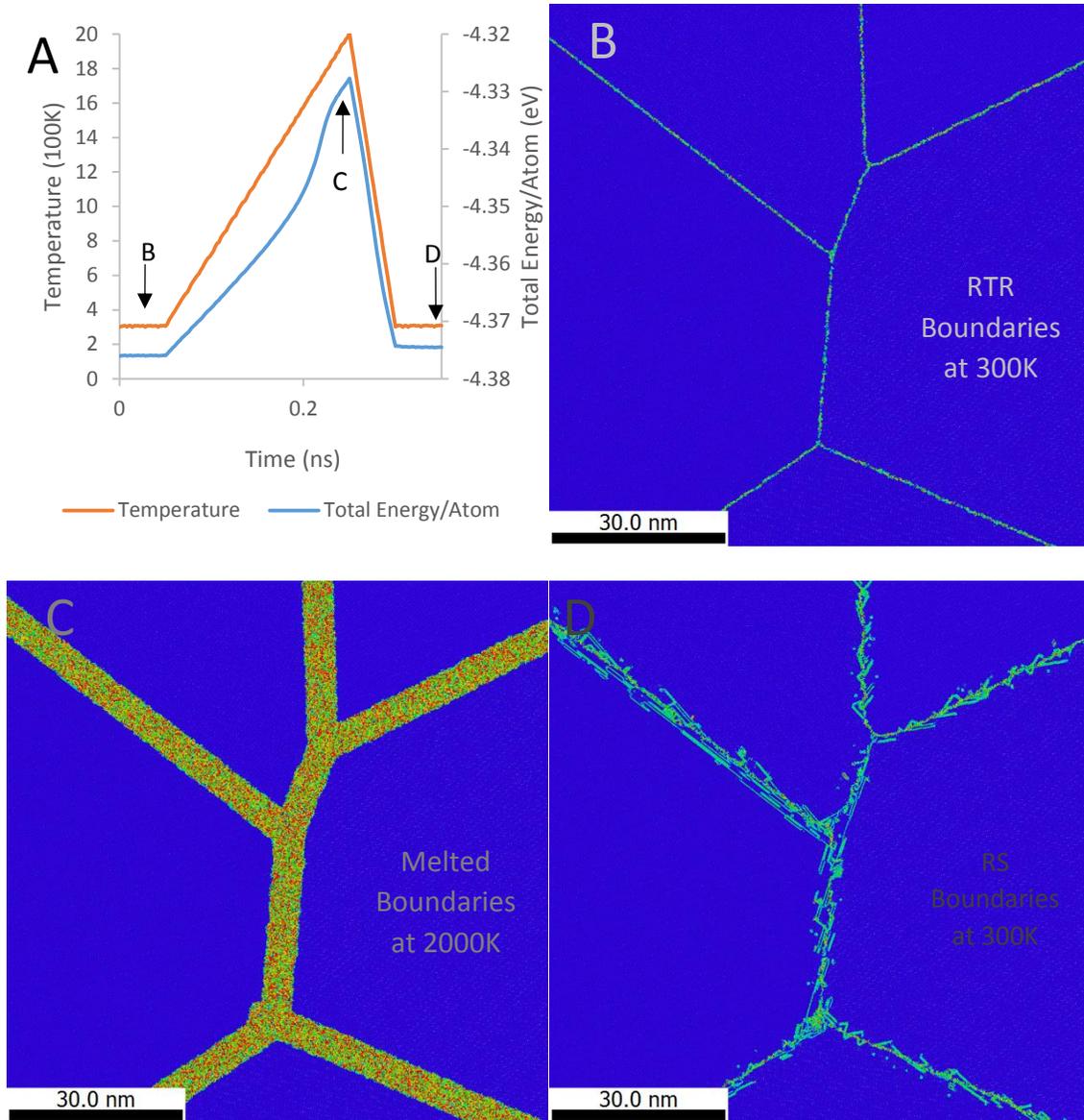
Figure 4-2: Illustration of RS boundary formation procedure including (A) the temperature and per atom energy as a function of time and centrosymmetry maps of a GB dense region of the sample with (B) RTR boundaries, (C) the GBs during their melted state and (D) RS boundaries. The point in the procedure when maps in (B), (C) and (D) were generated is indicated in (A).
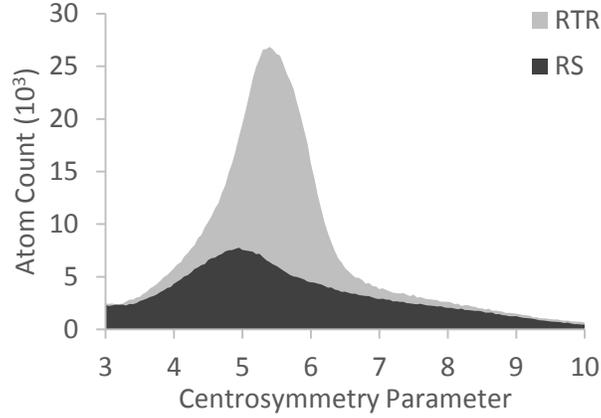
Figure 4-3: Histogram of centrosymmetry parameter in sample with RTR and RS boundaries with a bin size of 0.05. An x-axis range of 3-10 highlights the lesser of two modes in the distribution. The greater mode is at 0 and encompasses the bulk atoms, while the lesser encompasses more atoms in higher degrees of disorder.

4.2.2 Determination of the Grain Boundary Energy and Thickness

To determine the grain boundary energy, a rectangular prism section of each grain boundary was examined. The sections were 8nm in the z-direction, 10nm in the direction perpendicular to the boundary plane and 20nm in third orthogonal direction (parallel to both the grain boundary plane and the free surface. The grain boundary energy was then determined as follows:

$$\gamma = \frac{1}{A_{GB}} \sum_{i=0}^{N} E_i - \bar{E} \tag{1}$$

In equation 1, $\bar{E}$ is the average energy of a bulk crystal atom (found to be -4.409eV in this case), N is the number of sampled atoms, and A is the sample GB area.

Since a grain boundary is a region of high excess energy in a material, the point at which the potential energy of atoms begins to significantly deviate from that of the bulk was considered the transition from the bulk crystal region to the boundary region. In order to determine the approximate position of these transition planes and subsequently the grain boundary thickness, a Gaussian-like distribution was fit to a distribution of potential energy (E) vs. perpendicular distance from GB plane (x') via a least-squares

63

fitting method. The fitting equation (2) has 4 fitting parameters: base per-atom energy (E_0), energy peak

height (E_{max}), x' offset (x'_0), and boundary width (w).

$$E_{fit} = E_0 + E_{max}e^{-2.3025\left(\frac{x'-x'_0}{w/2}\right)^2} \tag{2}$$

The boundary width is accepted to be the horizontal distance between the two points along the fitting

curve with a potential energy of the base per-atom energy plus 10% of the max peak height. Eq. 2 is

displayed with the coefficient -2.3025 in order allow the direct determination of *w* since $e^{-2.3025} \approx 0.1$.

This procedure is illustrated in Figure 4-4.
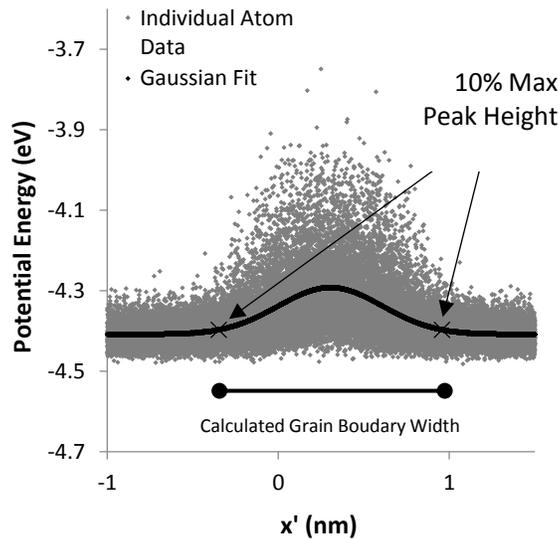
Figure 4-4: Demonstration of GB thickness determination. The Gaussian distribution curve in eq. 2 is fit to the scatterplot of Potential Energy vs. distance from the GB plane. The GB width is taken as the distance between the points on either side of the distribution where the fitted energy deviates from the bulk potential by 10% of the fitted curve height.

4.2.3 Grain Boundary Structure and Dislocation Content

To detect and quantify dislocations in the digital samples, we utilized the Dislocation Extraction

Algorithm (DXA) [37] in the OVITO software package [43]. DXA detects dislocations by identifying

perfect lattice atoms by the CNA method [44], constructing an "interface mesh" around regions full of

continuous perfect lattice atoms, and iteratively constructing Burgers circuits through the interface

mesh to identify dislocation cores. Adjacent cores are connected and considered dislocations. A full

description of this method can be found in a 2010 publication by Stukovski and Albe [37]. In doing so,

DXA detects the length, Burgers vector and screw/edge character of the dislocations and the orientation

of the surrounding lattice. DXA also identifies the special dislocations in FCC crystals: Shockley ⅙<112>,

Perfect ½<110>, Stair-Rod ⅙<110>, Hirth ⅓<100> and Frank ⅓<111>. Dislocations that are not of one of

these types are labeled "other". This analysis was run on all sample atoms within approximately 5nm of

the boundary excluding triple junctions.

The planar dislocation density of each boundary was studied individually.   Since a dislocation's type

have implications on mechanical behavior, the density of each special dislocation type and that of

"other" dislocations are reported separately. To determine the planar dislocation content of the grain

boundary, the total summed dislocation length, obtained from DXA is divided by the grain boundary

area, as follows:

$$\rho_d = \frac{1}{A_{GB}} \sum_{i=1}^{n} l_i \tag{3}$$

In the above equation ρ_d is the planar dislocation density, l_i is the length of dislocation i, n is the

number of dislocations in the sampled area, A_{GB}. This equation will give the dislocation density as total

length of dislocations contained in the boundary per unit area of the grain boundary. This is different

from the standard dislocation density in the bulk, which is total dislocation length per unit volume of

material.

In order to understand the effects of applied strain, both samples underwent virtual strain-controlled

tensile deformation, at 300K in the horizontal direction of figure 1. The strain rate used was 10^7/s. This

high strain rate is due to the limitations of the available computing power, and is relatively slow for MD

simulations. As the samples were strained, the dislocation content of each boundary was followed in

intervals of 0.05% strain. Dislocations were emitted from triple junctions and grain boundaries and were seen to arrive at grain boundaries at opposite sides of a given grain. This procedure allowed us to follow the evolution of the grain boundary dislocation content as the emission/absorption process takes place. Special attention was given to the role of the different relaxation states in this evolution.

4.3 Results

4.3.1 Average Grain Boundary Thickness and Energy for Different Relaxation Treatments

For the RTR relaxed sample the average grain boundary energy was 8.55eV/nm^2 (1.37J/m^2).   This average value can be compared with that obtained in studies of a number of individual grain boundaries Ni in several FCC materials. These ranged for 1 to 1.4 J/m^2 for the boundaries considered of general character in Ni [45]. The boundaries with the RS treatment, containing additional disorder had a higher average energy of 12.12 eV/nm^2 (1.94 J/m^2). The difference is surprisingly significant, amounting to about 40% of the relaxed grain boundary energy value. This large effect has to be connected to the differences in the grain boundary structure and defect content.

The grain boundary thickness results are shown in Figure 3 and clearly indicate that the boundaries subject to the RS treatment are significantly thicker than the relaxed ones. The RTR lower energy boundaries have an average thickness of 1.05 nm. This value is consistent with standard rule of thumb estimates of grain boundary thickness of about 1 nm. We note that this result is based on the assumptions used to estimate the width based on the Gaussian-like fit to the individual atom energy distribution. The critical result is that using the same assumptions, the RS boundary showed a significantly greater average thickness of 1.64nm. This is 60% greater than the corresponding thickness of the relaxed boundaries. We also note that these values are several standard deviations apart when the Gaussian fit is considered.

4.3.2   Dislocation Contents of Various Boundaries

These results are shown in Table 4-2 for the sample with the RTR boundaries and in Table 4-3 for the

sample with the RS boundaries. The first important feature of these results is that for both samples, the

dislocation densities in the individual boundaries varied greatly with an overall average of 5.35×10^8/m

and a standard deviation of 6.27×10^8/m for the relaxed RTR boundaries. The variation in dislocation

densities for various Burgers vector families also varied greatly. Average Shockley ⅙<112> and Perfect

½<110> dislocation densities were 2.56×10^8/m and 2.07×10^8/m, respectively with standard deviations

of 3.27×10^8/m and 2.4×10^8/m. No significant density of Stair-Rod ⅙<110>, Hirth ⅓<100> or Frank

⅓<111> dislocations were observed in these boundaries. These quantitative differences in density

between boundaries are illustrated by renderings of the DXA output in Figure 4-5. In these figures,

dislocations appear as colored lines, areas of crystal matching appear transparent and defect meshes,

outer limits of lattices where no dislocations could be resolved, appear grey. One can see that boundary

1-2, a boundary with high density of Shockley and perfect dislocations and a low density of other

dislocations, has a near-complete network of dislocations with very little defect mesh. Boundaries 2-4

and 4-6 have portions where no dislocation could be detected and no dislocations were detected in

boundary 3-4. This sampling of boundaries indicates the degree of variety in the types and densities of

dislocations detected in the boundaries.

Table 4-2: Calculated GB energy, thickness, average dislocation segment length and planar dislocation density for the 15 RTR GBs present in the investigated sample. GBs are identified by their neighboring grains, shown in figure 4-1.

Neighboring Grains	Boundary Energy (eV/nm^2)	Boundary Thickness (nm)	Average Dislocation Length (nm)	Planar Dislocation Density by Burger's Vector (10^8/m)				
				$\frac{1}{3}\langle111\rangle$	$\frac{1}{6}\langle112\rangle$	$\frac{1}{2}\langle110\rangle$	Other	Total
1-2	8.00	1.09	1.07	0.06	9.47	7.93	2.43	19.89
1-3	8.52	0.95	0.85	0.00	4.06	1.25	1.00	6.31
1-4	8.51	0.96	0.71	0.00	0.02	0.61	1.89	2.52
1-5	8.35	0.92	0.68	0.00	0.10	0.02	0.29	0.40
1-6	8.87	1.17	n/a	0.00	0.00	0.00	0.00	0.00
2-3	8.76	1.04	0.81	0.00	0.96	1.18	0.57	2.71
2-4	8.93	1.01	1.33	0.00	0.93	5.76	6.78	13.48
2-5	7.89	1.02	n/a	0.00	0.00	0.00	0.00	0.00
2-6	8.98	0.95	n/a	0.00	0.00	0.00	0.00	0.00
3-4	8.10	1.02	0.65	0.00	0.00	0.00	0.00	0.00
3-5	8.55	0.98	0.83	0.00	0.07	0.00	0.00	0.07
3-6	9.04	1.34	0.85	0.00	1.96	0.90	1.53	4.38
4-5	8.66	1.12	1.16	0.00	4.94	3.88	2.21	11.03
4-6	7.93	1.19	1.20	0.04	8.93	2.22	1.43	12.63
5-6	9.13	0.95	0.88	0.03	0.89	1.32	2.70	4.94
Average	8.55	1.05	0.92	0.01	2.56	2.07	1.36	5.35
Standard Deviation	0.42	0.12	0.22	0.02	3.27	2.4	1.8	6.27

Table 4-3: Calculated GB energy, thickness, average dislocation segment length and planar dislocation density for the 15 RS GBs present in the investigated sample. GBs are identified by their neighboring grains, identified in figure 4-1.

Adjacent Grains	Boundary Energy (eV/nm²)	Boundary Thickness (nm)	Average Dislocation Length (nm)	Dislocation Density by Burger's Vector (10⁸/m)				
				$\frac{1}{3}\langle 111 \rangle$	$\frac{1}{6}\langle 112 \rangle$	$\frac{1}{2}\langle 110 \rangle$	Other	Total
1-2	12.25	1.66	1.16	1.66	15.87	5.60	3.43	26.55
1-3	11.43	1.53	1.11	1.38	4.29	0.87	0.78	7.32
1-4	12.13	1.83	1.23	1.18	2.79	0.48	1.55	6.00
1-5	14.82	1.68	1.56	2.56	6.97	0.40	1.10	11.03
1-6	12.12	1.88	1.72	1.90	1.71	0.00	0.23	3.84
2-3	11.50	1.58	1.13	1.18	2.31	0.66	0.76	4.90
2-4	11.84	1.61	1.23	1.51	3.10	3.53	5.19	13.33
2-5	11.22	1.55	1.26	0.54	2.70	0.75	1.93	5.92
2-6	12.22	1.48	1.78	1.31	0.95	0.00	0.03	2.30
3-4	12.14	1.51	1.14	2.80	6.94	1.00	2.11	12.84
3-5	13.07	1.37	1.61	2.18	4.41	0.01	0.21	6.82
3-6	12.08	1.83	1.16	1.63	2.79	1.50	1.22	7.14
4-5	11.97	1.84	1.00	0.92	7.11	1.44	1.52	10.99
4-6	11.12	2.04	1.16	1.70	9.89	1.44	1.70	14.73
5-6	11.98	1.19	1.16	1.30	2.44	2.09	3.36	9.19
Average	12.12	1.64	1.29	1.58	4.95	1.32	1.67	9.53
Standard Deviation	0.89	0.22	0.25	0.60	3.92	1.50	1.41	5.95
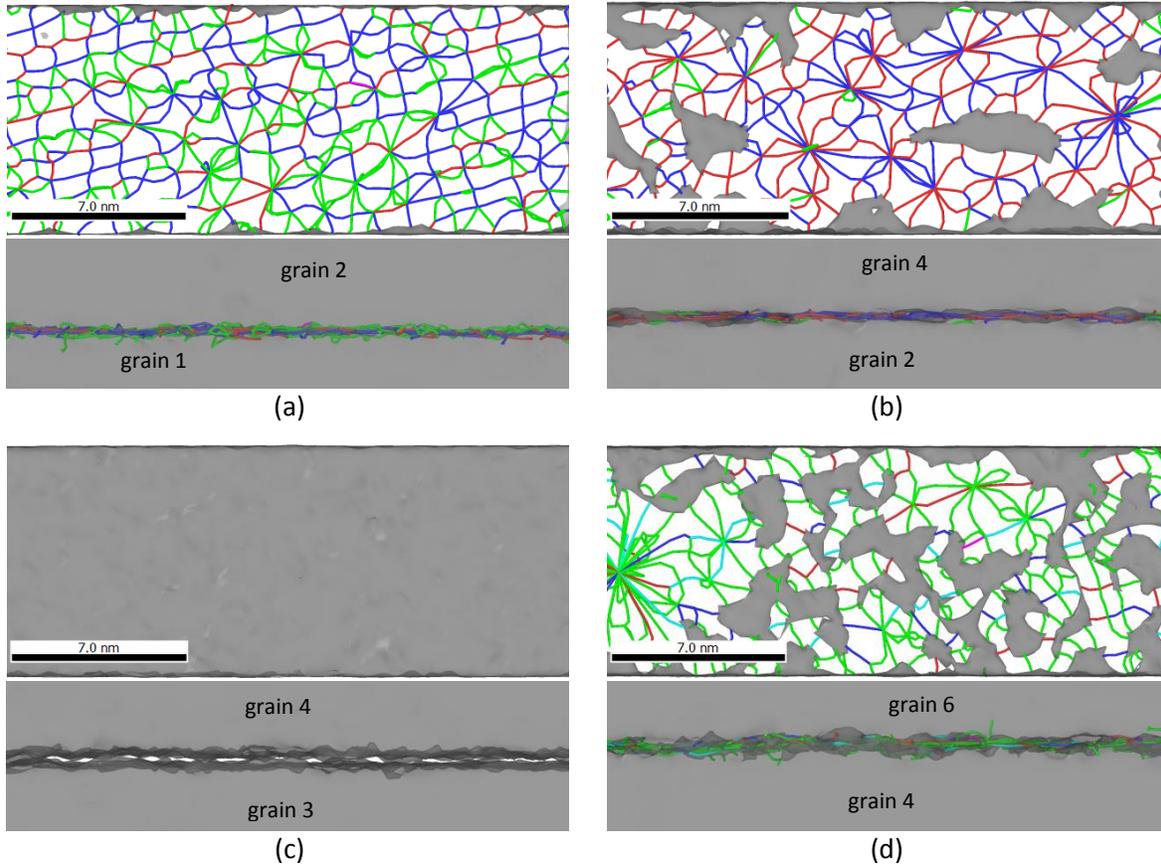
Figure 4-5: Renderings of DXA output of RTR boundaries (top to bottom) (a) 1-2, (b) 2-4, (c) 3-4 and (d) 4-6 (top) view perpendicular to grain boundary plane and (bottom) view perpendicular to sample surface.

An enlarged view of a small portion of boundary 1-3 is shown in Figure 4-6 with Burgers vectors overlaid.

From the figure, one can see that regions where dislocations are detected contain a number of

dislocations of various Burgers vectors, with lengths on the order of 1nm. All dislocations segments

begin and end at intersections with 2 or more other segments or a surface mesh. In boundaries 1-4, 2-4,

3-4 and 3-5 all dislocations were found to belong to just one of the adjacent grains. In boundaries 1-3,

1-5, 2-3, 3-6, 4-5 and 4-6 dislocations were detected that belong to both adjacent grains. In boundaries

1-2 and 5-6, dislocations were detected on a third lattice orientation, which was between the

orientations of the two adjacent grains. This behavior can be attributed to the fact that these two

particular boundaries were the ones with the smallest misorientation angles in the sample.
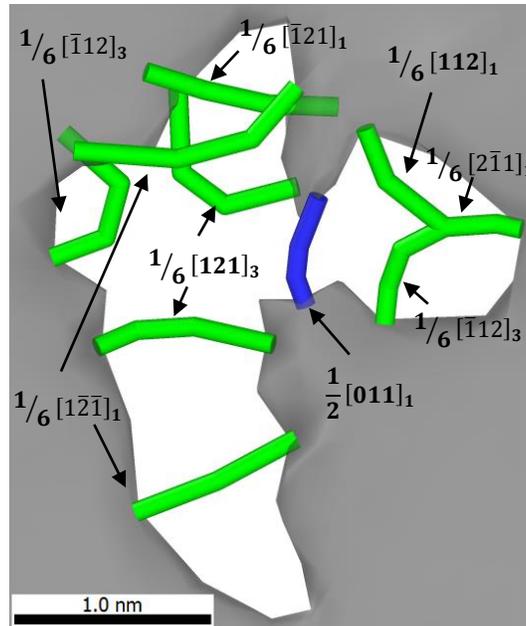
Figure 4-6: Detailed rendering of a small section of RTR GB 1-3. Markers indicated the Burger's vector of each dislocation with the subscript identifying the grain to which the dislocation belongs.

There was a similar degree of variation in dislocation densities in the RS boundaries. The full

quantitative data for this sample is in table 4-3. The RS boundaries consist of a network of short

dislocations and defect mesh within a mostly planar section plus sets of longer dislocations, extending

significantly more out of the grain boundary plane. Many of these out-of-plane defects lie outside of the

calculated thicknesses of these boundaries (1-2nm). RS boundaries 1-2, 2-4 and 4-6 have in-plane

dislocation networks visually similar to their RTR counter parts, with the addition of several longer out-

of-plane dislocations. In boundary RS 3-4, in-plane dislocations can be seen whereas in RTR 3-4, there

were none. This change was common in boundaries that had very low dislocation densities in their RTR

state. As mentioned above, in the RTR GBs, dislocations detected in RS 1-2 and 5-6 belonged to a lattice

orientation between that of the adjacent grains. In all other GBs, dislocations were detected on both

71

lattice orientations. In contrast to the RTR sample, a small number of dislocations were detected in the

RS GBs that belonged to the lattice of neither grain but an fcc lattice with a third orientation. This is

likely due to highly localized lattice straining, and is another indicator of disorder in the RS sample.
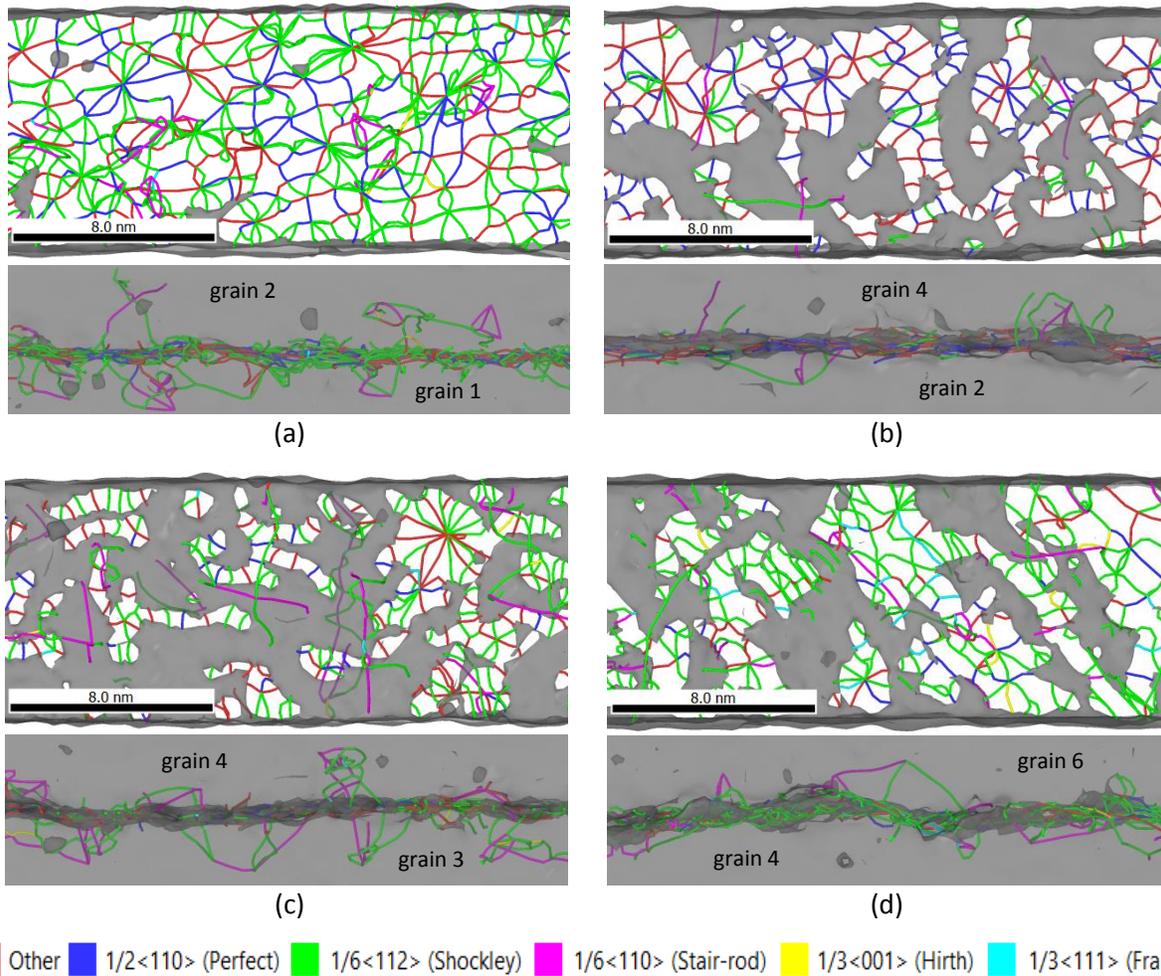
Figure 4-7: Renderings of DXA output of RS boundaries (a) 1-2, (b) 2-4, (c) 3-4, and (d) 4-6 from (top) view perpendicular to grain boundary plane and (bottom) view perpendicular to sample surface.

The average length of dislocations in the RS boundary (1.29nm) was greater on average than that of the

RTR boundary (0.92nm). These were roughly one standard deviation apart. Full quantitative results are

reported in tables 4-2 and 4-3. A distribution of the thicknesses is shown in Figure 4-8.

72
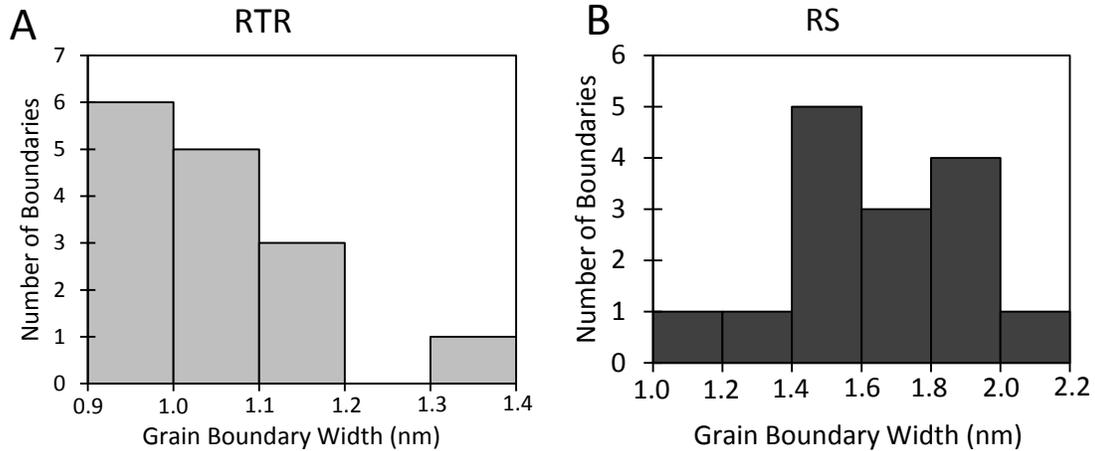
Figure 4-8: Histograms of (A) RTR and (B) RS GB thicknesses

The calculated planar dislocation density was significantly higher in the RS boundaries than the RTR

boundaries. When corrected for the calculated thickness, however, the volumetric dislocation content

was roughly the same. The density of Shockley and Stair-Rod dislocations was significantly higher in the

RS boundaries, while the density of Perfect and other dislocations was roughly the same in both types.

No significant density of Hirth ⅓<100> or Frank ⅓<111> dislocations were observed. This is illustrated in

Figure 4-9. This indicates higher densities of dislocations when boundaries are more disordered, as

formed by quenching as opposed to the relaxed boundaries. No correlation was observed between GB

dislocation content and GB energy.
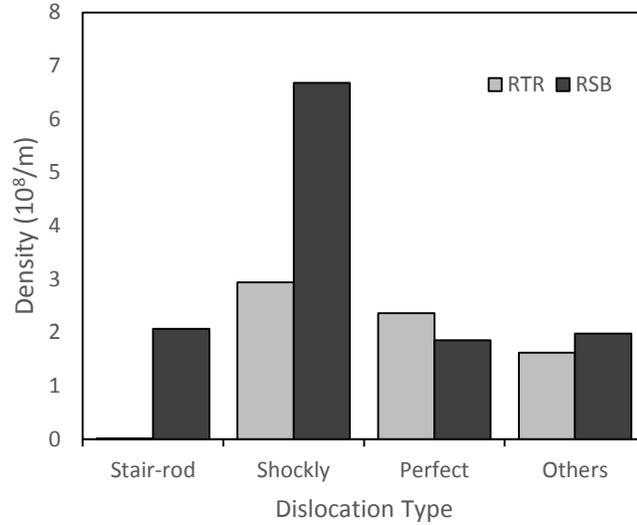
Figure 4-9: Histogram of dislocation density by type in both samples.

4.3.3 Response to Applied Strain

Figure 4-10 shows the stress-strain behavior for both samples studied. The sample with the more

disordered RS boundaries was slightly softer than the sample with relaxed RTR boundaries. The impact

of the more defective boundary structure is to make plastic deformation easier. Grain boundary

accommodation of strain can occur to a higher degree in the RS sample than in the RTR boundaries. The

RS boundaries contain more long Shockley partial dislocations, which are highly mobile in FCC materials

[46]. An increase in their activity could also contribute to the increase in boundary strain

accommodation and a general softening.
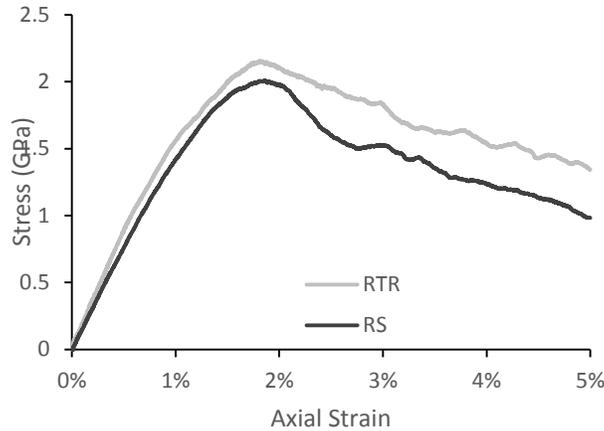
Figure 4-10: Stress response of investigated sample with RTR and RS GBs during strain controlled virtual tensile tests up to 5%

Strain in the system caused the boundary dislocation densities to evolve non-uniformly. Figure 4-11 shows some examples of this evolution. The density of Shockley partial dislocations showed the greatest variability with strain. The planar density of Shockley partial dislocations in many boundaries such as the GB between grains 1 and 3 in the RTR sample (given the shorthand RTR 1-3) as shown in Figure 4-11a gradually increases with strain. In other boundaries such as RS 1-5 shown in Figure 4-11b, the density of Shockley partial dislocations gradually decreases. The density of Perfect and other dislocations remained mostly constant with straining. Stair-rod density consistently decreased in with straining in the RS boundaries and increased in the RTR boundaries. The average dislocation density evolution of all boundaries during straining is shown in Figure 4-12. Note that the values at 0 strain do not match those of the averages in tables 2 and 3 because the values in Figure 4-12 are an overall density and those in the tables are averages of individual GB dislocation densities. In the RTR sample, boundary Shockley density increases fairly steadily. Small trends may exist in the density of "other" dislocations but they do not appear significant with the amount of noise in the data. In the RS sample, the densities of Shockley and Stair-rod dislocations decrease steadily during the first 3% of axial straining, at which point Shockley dislocation density begins to increase and stair rod density becomes

75

fairly consistent. As in the RTR boundary, no significant change was observed in the "Perfect" or

"Other" planar dislocation densities. Both stayed at roughly 2×10^8/m throughout.
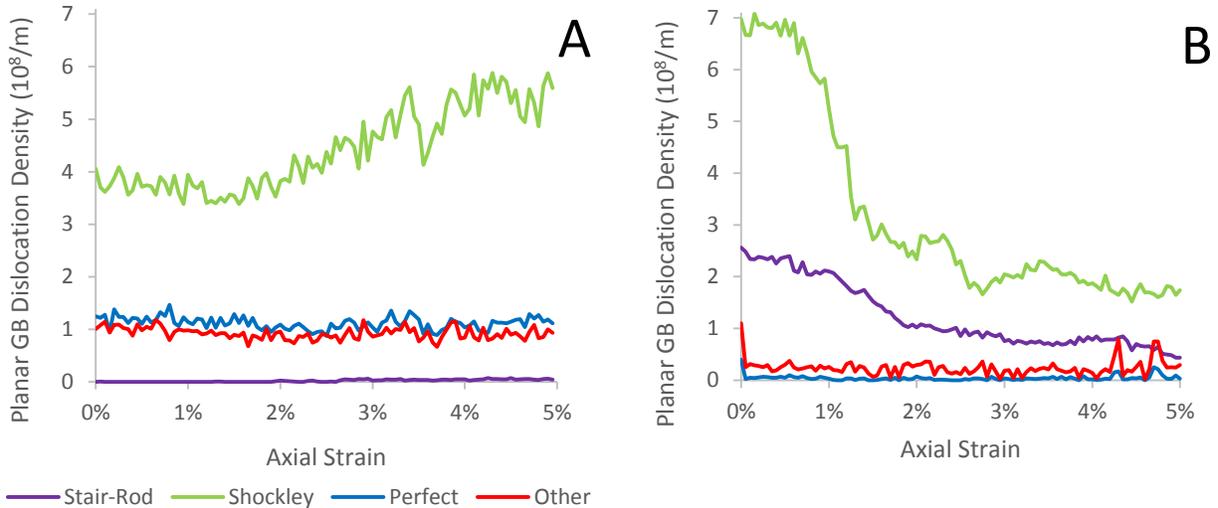
Figure 4-11: Evolution of planar Shockley partial (green), Stair-rod partial (purple), Perfect (blue) and Other (red) dislocation density for (A) RTR 1-3 and (B) RS 1-5 GBs during straining.
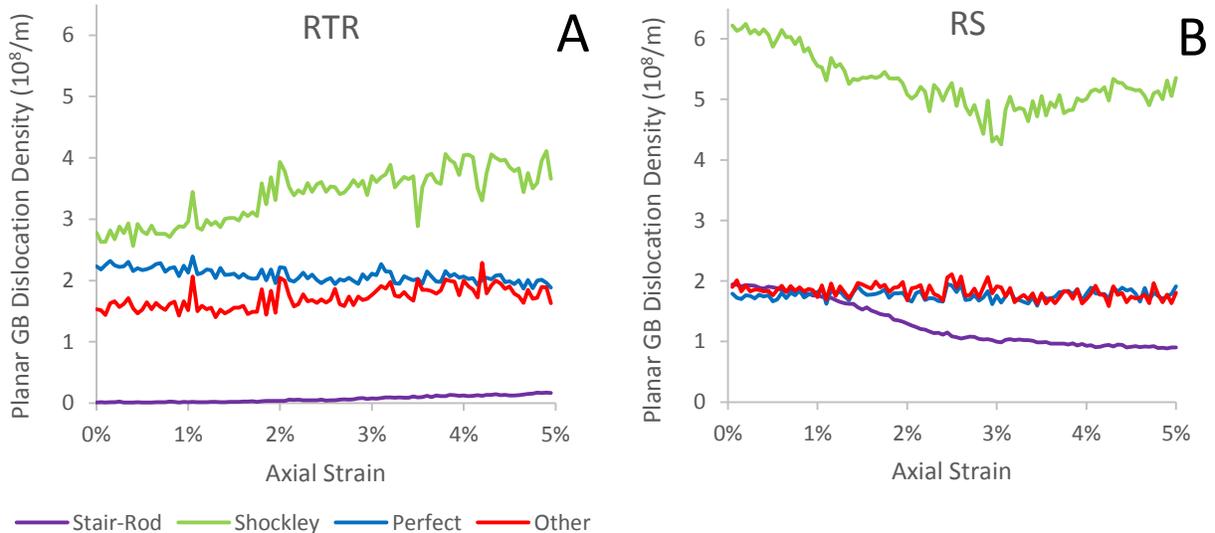
Figure 4-12: Evolution of overall planar Shockley partial (green), Stair-rod partial (purple), Perfect (blue) and Other (red) dislocation density for (A) RTR and (B) RS GBs during straining.

The divergence in the trend of GB dislocation density with applied strain between the RTR and RS

boundaries indicates that a GB's response to strain depends strongly on its initial relaxation state. These

trends were not found to correlate to dislocation emission from or absorption in the boundaries. In most observable cases, intergranular dislocations encountering the boundary during straining were undetectable after being absorbed and did not contribute to the boundary dislocation region. Examples of this behavior can be view in Video 4-1 and 4-2 in the supplemental material. Likewise, the few dislocations that were emmited from the RTR boundaries were not observed to be part of the original boundary dislocation structure. An example can be seen in Video 4-3. Video 4-4 shows a dislocation encountering the grain boundary and interacting with boundary dislocations. This behavior was only seen in boundary RTR 1-2 where the misorientation angle was low. Intergranular slip was observed to occur easily in this boundary.

4.4 Discussion

These results indicate that random grain boundaries contain dislocations that can, in digital samples, be resolved and quantified without assumptions from continuum solutions. As expected, we found a high density of dislocations in the boundaries that within our random set represent the lowest misorientation angle.

We searched for correlations of the dislocation content with grain boundary energy and no clear connection was found, except that in all cases both dislocation content and grain boundary energy values were significantly higher in the more disordered RS boundaries than in the relaxed RTR boundaries. In addition, it is worth noting that the grain boundary thickness and the average dislocation length were higher in the more disordered boundaries.

The relaxation state of the boundaries affected their plastic response in significant ways. This is consistent with previous work by Tucker et al. that studied deformation response as a function of non-equilibrium state of the boundary during both tensile and shear simulations [7]. Hasnaoui et al. also reported a reduction in plastic strain when grain boundaries and triple junction regions approach more

equilibrium conditions [47]. More recently, Han et al. investigated the nature of GB metastability and its

impact on material properties, demonstrating that the multiplicity of metastable GB states is, in

general, very large [2]. Our results indicate that the effects of this large multiplicity of structures can be

significant in the plastic response and the dislocation content of the boundaries.

In the present work, we searched for correlations among the dislocation content of the boundaries and

the ease of dislocation emission from the boundaries. It may seem reasonable to expect that the

dislocations that are already part of the grain boundary structure may be the first ones to be emitted

from the boundary as a response to stress.   We could not demonstrate such correlation in a statistically

significant way, possibly due to the fact that the triple junctions constituted such a common site of

emission in our simulations, limiting our statistics of emission events from the grain boundary away

from triple junctions. We did observe easier dislocation emission from the more disordered RS

boundaries. Tucker et al. analyzed the role of interface structure, stress state and initial free volume on

dislocation nucleation and found that particular free volume distributions show a greater propensity for

collective atomic migration during inelastic deformation [48]. Burberry et al demonstrated a

statistically valid relationship linking GB energy and free volume with the critical resolved shear stress

for dislocation nucleation under compressive loading [7, 49].

We found that the grain boundary structure and the corresponding dislocation content evolves as a

result of deformation in complex ways given by the emission and absorption of dislocations by the grain

boundaries. Yu et al. reported that deformation can drive GBs to higher energy states with highly

disordered structures [50]. Conversely, Rupert and co-workers showed that when GB processes

dominate deformation, boundary energy can trend downward during deformation [51]. In our results

the applied strain had opposite effects on the dislocation densities of various grain boundaries,

indicating that the effect depended on the individual grain boundary structure and relaxation state. In

general, the dislocation content of the more relaxed RTR boundaries increased with applied strain, whereas that of the more disordered RS GBs decreased.

Dislocation networks within GBs are difficult to study experimentally. However, some recent experimental work using transmission electron microscopy (TEM) has been reported [52-55]. Hong et al observed networks of "Perfect" dislocations (Burger's vector <110>/2) in boundaries with small inclination to {111} planes in rolled Al [12]. The propensity for perfect dislocations, as opposed to the higher densities of Shockley partials observed in the present study, is likely due to the higher stacking fault energy of Al (~140mJ/m^2)[46] as compared to Ni (~62mJ/m^2 in this potential)[56]. Perfect dislocations in in high stacking fault materials are less likely to dissociate into partial dislocations. In a subsequent study by Winther et al, FBE with dislocation types from TEM observations was employed to predict the density of these dislocation boundaries [57]. Qualitative and quantitative comparison led to the conclusion that in certain circumstances, dislocation networks observed via TEM matched these predictions. The reported total planar dislocation densities in the range of 1.9 to 6.6 10^7/m are lower than those found in this work, with averages of 5.35 x10^8/m and 9.53x10^8/m in our two GB types. This difference could be due to several factors including the material considered, the type of boundary and the method of analysis.

4.5 Conclusions

The dislocation content within the structure of random grain boundaries in an FCC polycrystal was investigated through Molecular Dynamics modeling and the Dislocation Extraction Algorithm (DXA) for detecting lattice dislocations. Using this technique, dislocations have been detected in a large fraction of randomly oriented boundaries without assumptions from continuum calculations.

DXA analysis of our samples shows the presence of Shockley partial dislocations in most boundaries, despite their random nature. As expected, higher densities of these partial dislocations appeared for

the boundaries with relatively low misorientation angles. The observed dislocation content varied widely depending on specific boundary geometrical parameters and relaxation state, with more dislocations appearing in less relaxed boundaries.

A comparison of the results for two different grain boundary relaxation states yielded important qualitative information. The first relaxation state, a conventional room temperature relaxation procedure yielded lower grain boundary energies and lower grain boundary widths. Boundaries containing additional disorder resulting from local melting and rapid solidification (RS) had increased energies, increased width and higher dislocation content as part of their structure. Though additional disorder caused an increase in both GB energy and dislocation content, the two properties were not found to correlate to one another across all boundaries.

Virtual tensile straining of these samples revealed how the dislocation content changed as a function of the strain applied to the sample. Under room temperature axial loading, GB dislocation content decreased in the sample with more disordered boundaries and higher dislocation content, and increased in the sample with more relaxed boundaries. These trends were not found to be caused by the absorbtion and emission of dislocations in the boundaries during straining.

Acknowledgements

References

1. King, A.H. and S. Shekhar, *What does it mean to be special? The significance and application of the Brandon criterion.* Journal of Materials Science, 2006. **41**(23): p. 7675-7682.
2. Han, J., V. Vitek, and D.J. Srolovitz, *Grain-boundary metastability and its statistical properties.* Acta Materialia, 2016. **104**: p. 259-273.
3. Frolov, T., M. Asta, and Y. Mishin, *Phase transformations at interfaces: Observations from atomistic modeling.* Current Opinion in Solid State & Materials Science, 2016. **20**(5): p. 308-315.
4. Dillon, S.J., K.P. Tai, and S. Chen, *The importance of grain boundary complexions in affecting physical properties of polycrystals.* Current Opinion in Solid State & Materials Science, 2016. **20**(5): p. 324-335.
5. Rupert, T.J., *The role of complexions in metallic nano-grain stability and deformation.* Current Opinion in Solid State & Materials Science, 2016. **20**(5): p. 257-267.
6. Harmer, M.P. and G.S. Rohrer, *Grain boundary complexions - current status and future directions.* Current Opinion in Solid State & Materials Science, 2016. **20**(5): p. Iv-V.
7. Tucker, G.J. and D.L. McDowell, *Non-equilibrium grain boundary structure and inelastic deformation using atomistic simulations.* International Journal of Plasticity, 2011. **27**(6): p. 841-857.
8. Beamish, E., C. Campana, and T.K. Woo, *Grain boundary sliding in irradiated stressed Fe-Ni bicrystals: a molecular dynamics study.* Journal of Physics-Condensed Matter, 2010. **22**(34).
9. Pan, Z.L. and T.J. Rupert, *Amorphous intergranular films as toughening structural features.* Acta Materialia, 2015. **89**: p. 205-214.
10. Sutton, A.P. and V. Vitek, *On the Structure of Tilt Grain Boundaries in Cubic Metals II. Asymmetrical Tilt Boundaries.* Philosophical Transactions of the Royal Society of London. Series A, Mathematical and Physical Sciences, 1983. **309**(1506): p. 37-54.
11. Read, W.T. and W. Shockley, *Dislocation Models of Crystal Grain Boundaries.* Physical Review, 1950. **78**(3): p. 275-289.
12. Hong, C.S., X.X. Huang, and G. Winther, *Dislocation content of geometrically necessary boundaries aligned with slip planes in rolled aluminium.* Philosophical Magazine, 2013. **93**(23): p. 3118-3141.
13. Frank, F.C., *Martensite.* Acta Metallurgica, 1953. **1**(1): p. 15-21.
14. Bilby, B.A., R. Bullough, and E. Smith, *Continuous Distributions of Dislocations: A New Application of the Methods of Non-Riemannian Geometry.* Proceedings of the Royal Society of London. Series A. Mathematical and Physical Sciences, 1955. **231**(1185): p. 263-273.
15. Rezvanian, O., M.A. Zikry, and A.M. Rajendran, *Statistically stored, geometrically necessary and grain boundary dislocation densities: microstructural representation and modelling.* Proceedings of the Royal Society a-Mathematical Physical and Engineering Sciences, 2007. **463**(2087): p. 2833-2853.
16. Sutton, A.P. and R.W. Balluffi, *Interfaces in Crystalline Materials.* 1996: Clarendon Press.
17. Wang, J., et al., *Characterizing interface dislocations by atomically informed Frank-Bilby theory.* Journal of Materials Research, 2013. **28**(13): p. 1646-1657.
18. Wang, J., et al., *Interface dislocation patterns and dislocation nucleation in face-centered-cubic and body-centered-cubic bicrystal interfaces.* International Journal of Plasticity, 2014. **53**: p. 40-55.
19. Cheng, Y.F., D. Weygand, and P. Gumbsch, *Simulation of small-angle tilt grain boundaries and their response to stress.* Computational Materials Science, 2009. **45**(3): p. 783-787.
20. Lim, A.T., D.J. Srolovitz, and M. Haataja, *Low-angle grain boundary migration in the presence of extrinsic dislocations.* Acta Materialia, 2009. **57**(17): p. 5013-5022.

21.   Sheikh-Ali, A.D., *On the contribution of extrinsic grain boundary dislocations to grain boundary sliding in bicrystals.* Acta Materialia, 1997. **45**(8): p. 3109-3114.

22.   Sheikh-Ali, A.D., *Coupling of grain boundary sliding and migration within the range of boundary specialness.* Acta Materialia, 2010. **58**(19): p. 6249-6255.

23.   Cahn, J.W., Y. Mishin, and A. Suzuki, *Duality of dislocation content of grain boundaries.* Philosophical Magazine, 2006. **86**(25-26): p. 3965-3980.

24.   Bernstein, N., *The influence of geometry on grain boundary motion and rotation.* Acta Materialia, 2008. **56**(5): p. 1106-1113.

25.   Van Swygenhoven, H., P.M. Derlet, and A. Hasnaoui, *Atomic mechanism for dislocation emission from nanosized grain boundaries.* Physical Review B, 2002. **66**(2): p. 024101.

26.   Kinoshita, K., T. Shimokawa, and T. Kinari, *Grain Boundary Structure Dependence of Extrinsic Grain Boundary Dislocation Emission Phenomena: A Molecular Dynamics Study.* Materials Transactions, 2012. **53**(1): p. 147-155.

27.   Song, T. and B.C. De Cooman, *Martensite Nucleation at Grain Boundaries Containing Intrinsic Grain Boundary Dislocations.* Isij International, 2014. **54**(10): p. 2394-2403.

28.   Khater, H.A., et al., *The disconnection mechanism of coupled migration and shear at grain boundaries.* Acta Materialia, 2012. **60**(5): p. 2007-2020.

29.   Van Swygenhoven, H., P.M. Derlet, and A.G. Frøseth, *Nucleation and propagation of dislocations in nanocrystalline fcc metals.* Acta Materialia, 2006. **54**(7): p. 1975-1983.

30.   Bieler, T.R., et al., *The role of heterogeneous deformation on damage nucleation at grain boundaries in single phase metals.* International Journal of Plasticity, 2009. **25**(9): p. 1655-1683.

31.   Swiatnicki, W.A., et al., *Thermal stability of extrinsic dislocations in near Sigma 11 grain boundaries in nickel.* Acta Materialia, 1998. **46**(5): p. 1711-1717.

32.   Farkas, D., *Atomistic simulations of metallic microstructures.* Current Opinion in Solid State & Materials Science, 2013. **17**(6): p. 284-297.

33.   Hirth, J.P., R.C. Pond, and J. Lothe, *Spacing defects and disconnections in grain boundaries.* Acta Materialia, 2007. **55**(16): p. 5428-5437.

34.   Wang, J., I.J. Beyerlein, and C.N. Tome, *Reactions of lattice dislocations with grain boundaries in Mg: Implications on the micro scale from atomic-scale calculations.* International Journal of Plasticity, 2014. **56**: p. 156-172.

35.   Shimokawa, T., et al., *Effect of Extrinsic Grain Boundary Dislocations on Mechanical Properties of Ultrafine-Grained Metals by Molecular Dynamics Simulations.* Materials Transactions, 2009. **50**(1): p. 2-10.

36.   Bieler, T.R., et al., *Grain boundaries and interfaces in slip transfer.* Current Opinion in Solid State and Materials Science, 2014. **18**(4): p. 212-226.

37.   Stukowski, A. and K. Albe, *Extracting dislocations and non-dislocation crystal defects from atomistic simulation data.* Modelling and Simulation in Materials Science and Engineering, 2010. **18**(8).

38.   Plimpton, S., *Fast Parallel Algorithms for Short-Range Molecular-Dynamics.* Journal of Computational Physics, 1995. **117**(1): p. 1-19.

39.   Bussi, G., T. Zykova-Timan, and M. Parrinello, *Isothermal-isobaric molecular dynamics using stochastic velocity rescaling.* Journal of Chemical Physics, 2009. **130**(7).

40.   Daw, M.S. and M.I. Baskes, *Embedded-Atom Method - Derivation and Application to Impurities, Surfaces, and Other Defects in Metals.* Physical Review B, 1984. **29**(12): p. 6443-6453.

41.   Voter, A.F., Chen, S.P, *High temperature ordered intermetallic alloys.* MRS Symposia Proceedings, 1987. **82**: p. 175.

42.   Kelchner, C.L., S.J. Plimpton, and J.C. Hamilton, *Dislocation nucleation and defect structure during surface indentation.* Physical Review B, 1998. **58**(17): p. 11085-11088.

43.   Stukowski, A., *Visualization and analysis of atomistic simulation data with OVITO-the Open Visualization Tool.* Modelling and Simulation in Materials Science and Engineering, 2010. **18**(1).
44.   Frank, F.C., *Crystal Dislocations - Elementary Concepts and Definitions.* Philosophical Magazine, 1951. **42**(331): p. 809-819.
45.   Holm, E.A., D.L. Olmsted, and S.M. Foiles, *Comparing grain boundary energies in face-centered cubic metals: Al, Au, Cu and Ni.* Scripta Materialia, 2010. **63**(9): p. 905-908.
46.   Hull, D. and D.J. Bacon, *Introduction to dislocations*. 3rd ed. International series on materials science and technology. 1984, Oxford Oxfordshire ; New York: Pergamon Press. xiii, 257 p.
47.   Hasnaoui, A., H. Van Swygenhoven, and P.M. Derlet, *On non-equilibrium grain boundaries and their effect on thermal and mechanical behaviour: a molecular dynamics computer simulation.* Acta Materialia, 2002. **50**(15): p. 3927-3939.
48.   Tucker, G.J., M.A. Tschopp, and D.L. McDowell, *Evolution of structure and free volume in symmetric tilt grain boundaries during dislocation nucleation.* Acta Materialia, 2010. **58**(19): p. 6464-6473.
49.   Burbery, N.J., R. Das, and W.G. Ferguson, *Modelling with variable atomic structure: Dislocation nucleation from symmetric tilt grain boundaries in aluminium.* Computational Materials Science, 2015. **101**: p. 16-28.
50.   Yu, W.S. and S.P. Shen, *Energetics of point defect interacting with grain boundaries undergone plastic deformations.* International Journal of Plasticity, 2016. **85**: p. 93-109.
51.   Rupert, T.J. and C.A. Schuh, *Mechanically driven grain boundary relaxation: a mechanism for cyclic hardening in nanocrystalline Ni.* Philosophical Magazine Letters, 2012. **92**(1): p. 20-28.
52.   Pond, R.C., D.L. Medlin, and A. Serra, *A study of the accommodation of coherency strain by interfacial defects at a grain boundary in gold.* Philosophical Magazine, 2006. **86**(29-31): p. 4667-4684.
53.   Couillard, M., G. Radtke, and G.A. Botton, *Strain fields around dislocation arrays in a sigma 9 silicon bicrystal measured by scanning transmission electron microscopy.* Philosophical Magazine, 2013. **93**(10-12): p. 1250-1267.
54.   Lartigue-Korinek, S., et al., *Analysis of dissociated dislocations in a deformed bicrystal close to the rhombohedral twin orientation in -alumina.* Philosophical Magazine, 2013. **93**(10-12): p. 1182-1196.
55.   Lartigue-Korinek, S., et al., *Disconnection arrays in a rhombohedral twin in alpha-alumina.* Philosophical Magazine, 2008. **88**(10): p. 1569-1579.
56.   Zimmerman, J.A., H.J. Gao, and F.F. Abraham, *Generalized stacking fault energies for embedded atom FCC metals.* Modelling and Simulation in Materials Science and Engineering, 2000. **8**(2): p. 103-115.
57.   Winther, G., C.S. Hong, and X. Huang, *Low-Energy Dislocation Structure (LEDS) character of dislocation boundaries aligned with slip planes in rolled aluminium.* Philosophical Magazine, 2015. **95**(13): p. 1471-1489.

CHAPTER 5: ATOMISTIC STUDIES OF HYDROGEN EFFECTS ON GRAIN BOUNDARY STRUCTURE AND DEFORMATION RESPONSE IN FCC NI

Bryan Kuhr[1], Diana Farkas[1] and Ian M. Robertson[234]

[1]Department of Materials Science and Engineering, Virginia Polytechnic Institute and State University, Blacksburg, VA 24061

[2]Department of Materials Science and Engineering, University of Wisconsin, Madison, WI 53706

[3]Department of Engineering Physics, University of Wisconsin, Madison, WI 53706

[4]International Institute for Carbon-Neutral Energy Research (WPI-I2CNER), Kyushu University, 744 Motooka, Nishi-ku, Fukuoka, Fukuoka 819-0395, Japan

Abstract

The effect of hydrogen in the grain boundary on the mechanical response of random microstructures was studied by using atomistic simulation techniques and model interatomic potentials. The model interatomic potentials mimic properties of interstitial H in fcc materials within the limitations of empirical force laws. We report fully three-dimensional atomistic molecular dynamics studies of the mechanical response of identical samples with and without H in the grain boundaries. H content changes the structure of the grain boundaries and plays a critical role in the emission of dislocations from the grain boundaries under an applied stress. For lower deformation levels, the presence of H increased the yield strength of the samples, whereas for higher deformation levels, increased dislocation emission from grain boundary sources resulted in an increase in the number of dislocations in the pile-up at the grain boundaries. Increasing the H content resulted in increasingly larger cracks being formed on the grain boundaries, consistent with decreased grain boundary cohesion. Our results support a picture of hydrogen embrittlement resulting from the combined effects of hydrogen on plasticity as well as grain boundary decohesion.

Comments

This manuscript was published in Computational Materials Science [1]. It has been lightly edited for formatting

1. Kuhr, B., D. Farkas, and I.M. Robertson, *Atomistic studies of hydrogen effects on grain boundary structure and deformation response in FCC Ni.* Computational Materials Science, 2016. **122**: p. 92-101.

5.1 Introduction

Hydrogen embrittlement, the sudden and catastrophic failure of a metal at low applied load in the presence of hydrogen, is well documented and several mechanisms have been proposed to account for it [1, 2]. One manifestation of hydrogen-induced failure is that in some systems it can result in a transition in the failure mode from ductile transgranular to intergranular. Until recently this transition was interpreted as being driven by hydrogen segregated to the grain boundary reducing the cohesive strength of the grain boundary such that it became the weakest link in the system [3-5]. Here it was noted that there was evidence for plasticity but the role, if any, of it in the hydrogen-induced intergranular failure was not ascertained. However, recent experimental observations of the microstructure associated with hydrogen-induced intergranular failure in Ni [6] and Fe [7] have suggested that although the hydrogen-induced reduction in the cohesive strength is ultimately the cause of the failure, the conditions for establishing this failure mode are driven by hydrogen-enhanced plasticity processes. These include the ensuing changes in the grain boundary structure and in hydrogen content associated with slip transfer across it as well as the increase in the local stress state around the grain boundary due to the hydrogen-accelerated plasticity that occurs prior to the initiation of an intergranular crack [8].

However, full understanding of the hydrogen-induced failure mechanisms requires studies at the atomistic scale that are very difficult experimentally. Computer simulation techniques have been used for several decades now to investigate the mechanical response of nano-crystalline materials [9-13]. In these materials, grain boundaries contribute to the deformation process through the emission and/or absorption of Shockley partial dislocations. Additional mechanisms of accommodation of the stress at the grain boundaries have been uncovered, such as grain boundary sliding and strain-driven grain boundary migration.

For example, Sansoz and Molinari performed a series of quasi-continuum simulations at 0 K of a grain boundary, GB, in nano-sized Cu and Al bicrystals deformed under shear [14]. They emphasized that despite the importance of the GB structure for intergranular and intragranular deformation in nanocrystalline metals, the relation between the GB structure and their mechanical response is not well understood [15]. An important role of atomistic simulations is to inform the development of large-scale models of the behaviour of the interface between crystals [16]. Cao and Wei [17] performed large scale MD simulations of pure nanocrystalline, nc, Ni, subjected to uniaxial tensile loading and observed that the strain is mainly localized at GBs, with GB plasticity being a major contribution to the overall plastic deformation. Vo et al. [18] performed MD simulations of tension tests at different strain rates for polycrystalline Cu with grain sizes in the range of 5-20 nm. The contributions to plastic deformation due to dislocation activity and GB sliding were quantified. They found that dislocation activity increased with grain size but decreased with increasing strain rates. These examples are part of a large body of literature that has studied the connections between grain boundaries and microstructure and mechanical behaviour in pure fcc materials with general grain boundaries [19].

In parallel efforts, simulations have been utilized to understand the influence of H on the mechanical response of materials [20-27]. These studies have addressed H interstitials in bulk fcc materials [28, 29] and bicrystals [30]. The embrittling and strengthening effects of hydrogen, boron, and phosphorus on a Σ=5 (210) [100] nickel grain boundary were investigated by means of the full-potential linearized augmented plane-wave method [31]. Hickel et al. aimed at understanding segregation and diffusion mechanisms of H in steels using ab initio methods and discussed the advantages and shortcomings of the technique [32]. Furthermore, there have been significant efforts to model hydrogen embrittlement using continuum approaches and multi-scale methods [33-38] .

The current state of knowledge postulates that in the case of hydrogen-induced intergranular failure, hydrogen located at the grain boundary lowers the grain boundary cohesive energy but there is also

strong experimental evidence that H significantly affects the plastic response of the material [8].

Through in-situ straining experiments in a controlled environment transmission electron microscope it

has been shown that H increases the dislocation mobility, the dislocation generation rate and decreases

the separation distance between dislocations in a pile-up against an obstacle such as a grain boundary;

this work is summarized and reviewed by Robertson et al [39]. Interestingly, the effect on the behavior

of dislocations was ubiquitous, occurring in pure fcc, bcc and hcp metals as well as alloys based on them.

Hydrogen-enhanced plasticity has been used to explain the response of mechanical property tests

designed to assess the activation energy and volume of dislocation slip [40, 41]. The effect on the

dislocation mobility was explained by hydrogen attached to a dislocation modifying the stress field of

the dislocation such that in some directions the stress field was decreased and in others it was increased

– this hydrogen shielding effect is the basis for the hydrogen-enhanced localized plasticity mechanism

[33]. Song and Curtin [23, 24, 42] performed atomistic simulations of the effects of H on edge dislocation

mobility and pile-ups in order to investigate possible nanoscale mechanisms for hydrogen-enhanced

localized plasticity. In contrast to the experimental findings they found that the Cottrell-like hydrogen

atmospheres following the moving dislocations, leads to a resistance to dislocation motion that is

consistent with solute drag theory. They also found that these atmospheres do not affect the

equilibrium spacing of dislocations in a pile-up, which contradicts experimental observations [39].

Finally, Song and Curtin pointed out that a mechanistic understanding of H-enhanced localized plasticity

requires the evaluation of more complex H-dislocation interactions [23]. Li and co-workers utilized

multi-scale simulations to study the role of H-vacancy complexes [43]. They performed large-scale

molecular dynamics simulations to show that H-vacancy complexes are quite stable and tend to grow in

size. Chandler and co-workers [27] performed molecular dynamics (MD) simulations to study hydrogen

effects on nano-void nucleation in a nickel low-angle and high-angle symmetrical [001] tilt grain

boundaries. The results showed that hydrogen atoms were trapped at the grain boundaries and

enhanced nano-void nucleation. These simulations could explain the nano-voids experimentally observed in the H induced failure of Fe and steels [44, 45]. Here it is important to note that as the nano-void features were confined to the fracture surface and not observed sub-surface, an alternate explanation for the formation of these surface features has been put forth [46].

The present work constitutes a study of fully 3D samples containing randomly generated grain boundaries, created with and without various levels of intergranular H impurities. As the timescale of the simulations cannot account for lattice diffusion of hydrogen or hydrogen transport by the mobile dislocations, this study considered only the effect of hydrogen on the grain boundary structure and the emission of dislocations from it. The grain boundaries in the digital samples are random boundaries and the study focuses on the response of the polycrystal to an applied tensile deformation in a strain-controlled virtual tensile test. The results presented in this paper are organized as follows: First, we analyze the effects of H content on the structure of these random grain boundaries. The effect of hydrogen removal from the grain boundary by the emitted dislocations is not considered, the hydrogen concentration on the grain boundary is kept constant. Next, we discuss the effect of the intergranular H on the emission of dislocations from grain boundaries and the resulting dislocation pile ups at the boundaries. Finally, we present our results on the effect of the H in the grain boundary on the nucleation and propagation of intergranular cracks in these polycrystalline microstructures.

5.2 Simulation Procedure

5.2.1 Interatomic potentials

The deformation behavior under tension was modeled using molecular dynamics and embedded atom (EAM) interatomic potentials [47] developed for dilute interstitial H impurities [29]. These potentials are used as model potentials and are subject to the limitations of empirical potentials and, in particular, the central nature of the Embedded Atom Method [48]. The particular potentials used here were developed based on the heat and volume of solution of H in Ni (0.18 eV and 0.0023 nm^3) [29]. The migration energy

of H in the Ni lattice given by the potential is 0.35eV. These values are very similar to those given by the

potential of Baskes and co-authors [48]. In the potentials used here, Ni is represented by the potential

of Voter and Chen [49]. The potentials selected reproduce in a simple way the length and strength of

the H-Ni bond. They therefore crudely capture the basic size effects of the interaction of H with the fcc

host material as well as the magnitude of the chemical interaction. We note that the potentials are

appropriate for low H concentrations only [50]. As mentioned above, our results are subject to the

general limitations intrinsic to empirical potentials, and are indicative of trends only.

5.2.2 Sample generation and relaxation

The digital samples studied here have a polycrystalline thin-film configuration with randomly oriented

grain boundaries. All samples were created using a Voronoi tessellation method [19]. The samples

contain 6 grains (see Figure 5-1) with an average size of 40 nm [51]. For reference purposes the grains

are identified numerically in each of the figures. This grain size, chosen to avoid nano-size effects, is still

too small to support Frank-Read dislocation sources and dislocation multiplication. Therefore, the

dislocations observed are generated from grain boundary dislocation sources. Each sample contained

roughly 10 million atoms and had a thickness of about 8nm. The samples are periodic in the x- and y-

directions with free surfaces in the z-direction.
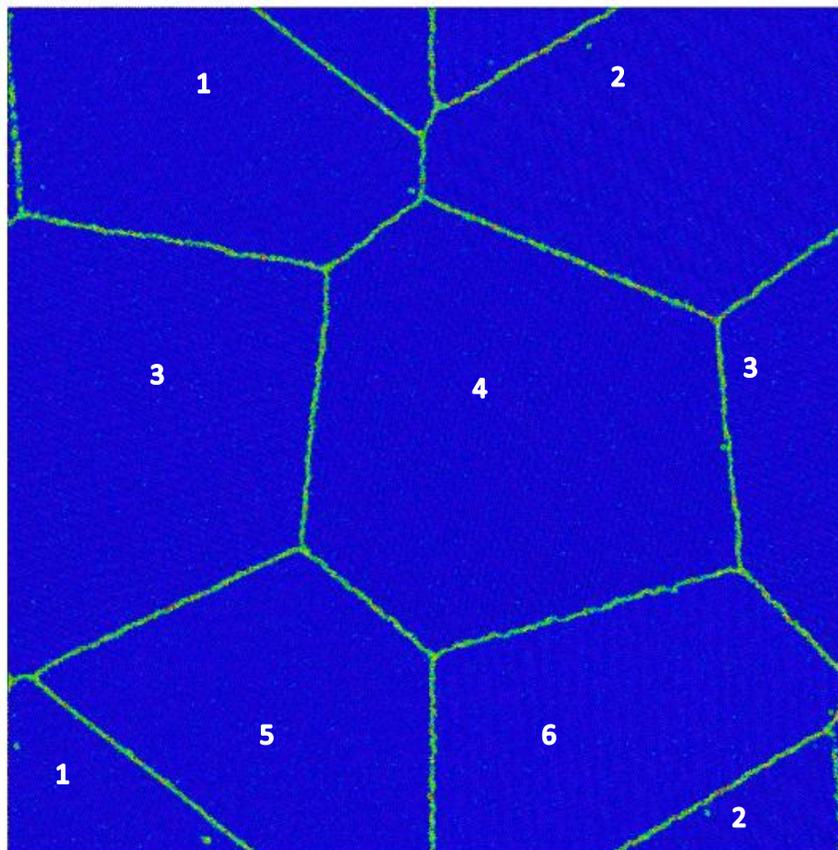
Figure 5-1: Microstructure the sample colored by centro-symmetry parameter.

The grain centers and orientations were chosen at random and the resulting grain boundaries are all

high-angle random boundaries, except for the boundary between grains 4 and 6, which was close to a Σ

= 3 misorientation. Grain boundary relaxation was achieved using molecular dynamics [52] in the

LAMMPS implementation [53] by increasing the temperature to 700K for 50ps and then returning to

300K for 50ps. An atom was determined to be a boundary atom if its centro-symmetry parameter was

above 3 and it was 1 nm away from the sample surface [54]. In order to determine the dependence of

intergranular failure on the hydrogen coverage on grain boundaries, the hydrogen coverage, expressed

as H atoms per nm^2 (H/nm^2) of grain boundary, was varied up to $8H/nm^2$. Our maximum hydrogen

coverage level corresponds to approximately half of a monolayer. All grain boundaries in the system

had roughly the same level of hydrogen coverage. The hydrogen atoms were positioned adjacent to

grain boundary atoms, and the system allowed to relax for 34.5ps at 300K.

5.2.3 Virtual tensile testing

After relaxation, all samples underwent virtual strain-controlled tensile deformation at 300K and a strain

rate of $3x10^8$/s. The LAMMPS code [53] was used for this part of the work, with a Nose-Hoover barostat

and thermostat. Periodicity in the direction of the tensile axis was used to control the deformation level

while pressure was maintained at zero in the direction perpendicular to it. The tensile axis was chosen

to be in the horizontal direction in Figure 5-1. It is appreciated that the strain rate used in the

simulations is several orders of magnitude higher than those used in experiments. This is an intrinsic

limitation of the technique. However, it will be shown that for the same simulation parameters, the

presence of hydrogen on the grain boundaries influences the response of the system and the differences

have parallels to experimental observations of the hydrogen-induced transition from transgranular to

intergranular failure. Specifically, this effort addresses the impact of hydrogen on the basic processes of

dislocation emission from grain boundaries as well as crack nucleation and propagation along grain

boundaries.

5.2.4 Analysis and Visualization

Visualization of the results was achieved by tracking the centro-symmetry [54] parameter of each atom

as deformation proceeded. Detailed visualization of results is achieved by color coding according to this

parameter at each stage of deformation and utilizing Ovito [55]. The dislocation extraction algorithm

(DXA) written by Alexander Stukovski [56] was used to detect and characterize dislocations in our

samples. This algorithm was run at 0.5% strain increments. Representations of these dislocations in the

sample were generated by color coding the observed dislocations by Burgers vector against the back

surface of the sample using the Paraview visualization suite [57]. These dislocations were sorted by

Burgers vector and line length, and counted to calculate dislocation density evolution during straining.

5.3 Results

5.3.1 Structure of grain boundaries with segregated hydrogen

During the relaxation of the randomly distributed hydrogen atoms in the grain boundary, the hydrogen atoms diffused along the grain boundary to occupy low energy sites.   The presence of H in the grain boundaries resulted in significant changes in the atomic structure of the grain boundary. The differences are shown in Figure 5-2 for the grain boundary between grains 1 and 5. The atoms are colored according to their centro-symmetry parameter, except for the H atoms which are colored black. With increasing hydrogen coverage more grain boundary atoms have higher centro-symmetry parameters (>10) (colored red) as well as larger distorted environments.   This result suggests that the impact of hydrogen on the grain boundary cohesive strength has contributions from both compositional as well as structural changes. The compositional effect is well documented and would manifest itself as a reduction of the cohesive strength because of H-bonding effects with Ni. However, it is only recently that the structural component has been recognized as being a contributor [8].

(a)   (b)
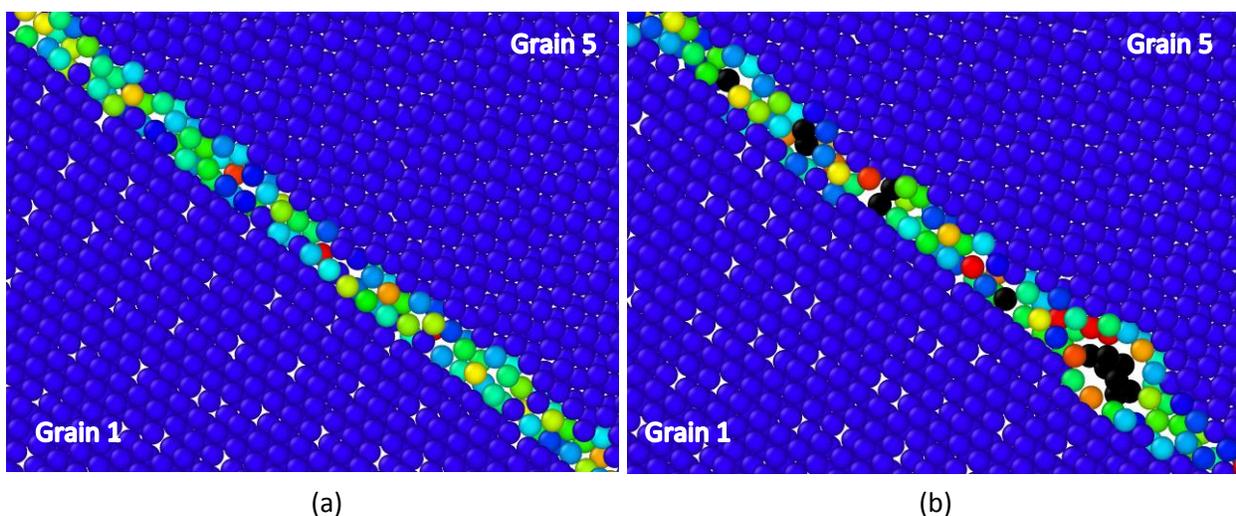
Figure 5-2: Detail of the grain boundary between grains 1 and 5. (a) without and (b) with H impurities showing significant changes in the grain boundary structure and H clustering.

Our results showed that within the times accessible to molecular dynamics the H that was initially located at the grain boundaries did not diffuse to the bulk, as expected from estimates of the H diffusivity in bulk Ni. However, our simulation times are indeed enough for H transport to occur within the grain boundary. This is in agreement with experimental and simulation work showing that grain boundary diffusion of H in nickel grain boundaries is significantly accelerated from the bulk values [58-63]. Therefore, our structures can represent an equilibrium distribution of H within the grain boundary but equilibrium with H in the bulk is not attained.

Some of the H atoms formed clusters of a few atoms and in association with regions of high free volume within the grain boundary. An example of such a cluster within the grain boundary can be seen in Figure 5-2. Figure 5-3 shows the distribution of hydrogen in the grain boundary between grains 3 and 4, viewed along the grain boundary plane. After a relaxation time of 35 ps, the cluster distribution remained constant with an average cluster size between 1.2 and 2.2 atoms. The average cluster size increased with H coverage, as shown in Figure 5-4. The cluster distribution remained stable for relaxation times up to 0.6ns at room temperature, confirming that the system has arrived at an equilibrium distribution of H in random boundaries. Therefore, the relaxation times possible in the molecular dynamics technique allow for sufficient mobility of the H atoms in the grain boundary to reach this equilibrium at room temperature. The particular location of the H atoms and clusters depends on the structure of the individual grain boundary at a local level, with disordered large free volume regions preferred for H occupation.
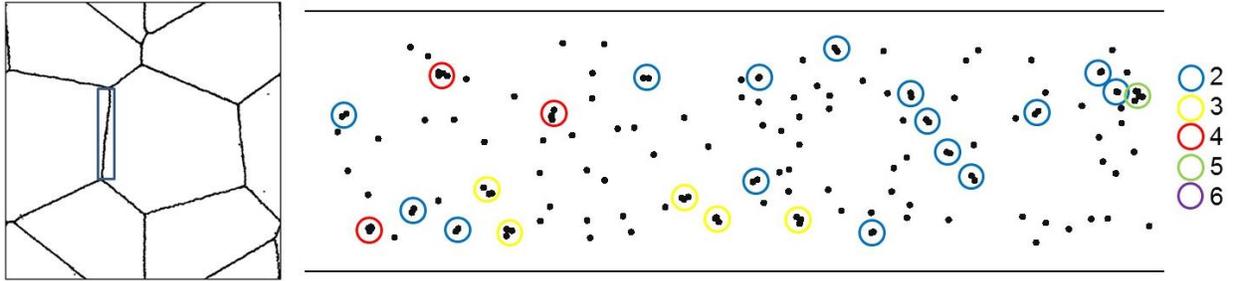
Figure 5-3: Clustering of H in selected boundary of 6.4H/nm² sample with Ni atoms deleted. The Ni atoms are deleted for clarity and the clusters are highlighted by circles of varying colors according to the number of H atoms in the cluster.
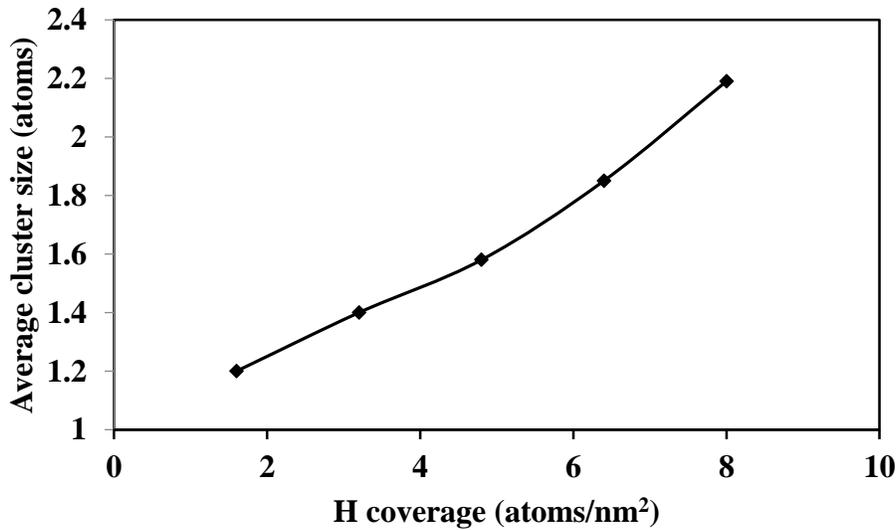
Figure 5-4: Average cluster size in the relaxed grain boundaries as a function of H coverage.

The frequency distribution of cluster sizes is shown in Figure 5-5 for the relaxed sample containing 8.0H atoms /nm² in the grain boundaries. We note that even if most of the H in the grain boundary remains as single atoms or two atom clusters there are a few clusters with up to 6 or 7 H atoms. The fraction of such clusters is quite small but they can have an important impact if they constitute preferred sites for dislocation emission and crack nucleation. The separation distance between H atoms within the clusters was on average 0.2 nm. This is much larger than the distance between H atoms in the H_2 molecule (0.074 nm) indicating that the formation of the clusters is driven by the H-Ni interaction and not the

94

interaction between H atoms to form the H_2 molecule. The tendency to form clusters of several H

atoms has been discussed for the case of vacancies in Fe [43, 64] and Ni [27].
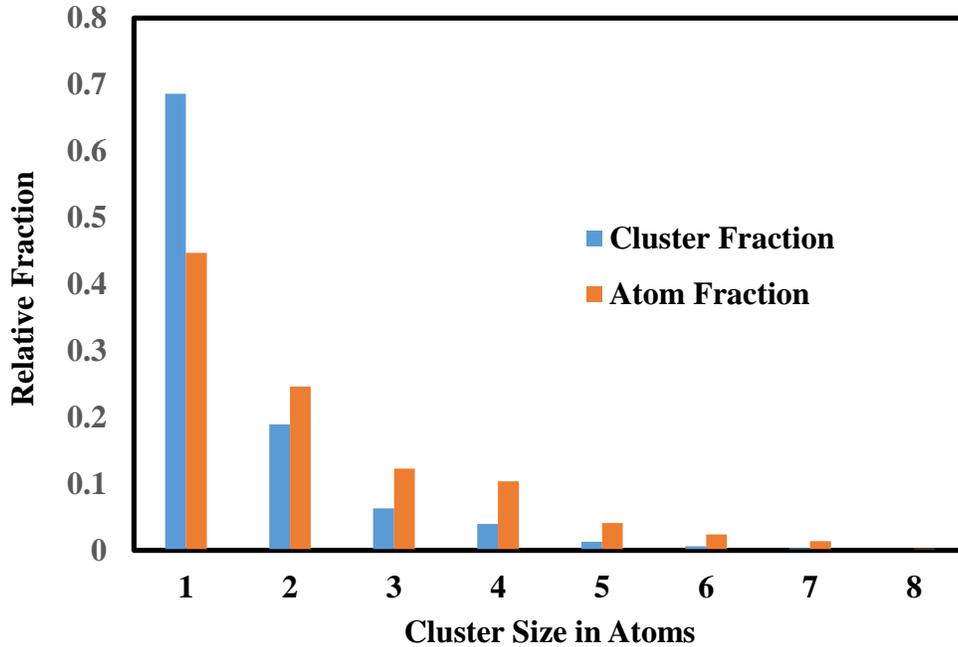
Figure 5-5: Frequency of grain boundary H clusters in the sample with grain boundary coverage of 8.0 H atoms/nm^2

Overall, the results of the simulations suggest that increased H concentrations in the grain boundary

produces a more disordered grain boundary structure, with H atoms clustering in regions of high free

volume. This is in agreement with simulations by Yu and co-authors [21] who performed a radial

distribution function analysis and reported that a high local grain boundary concentration of H at 900 K

can lead to a more disordered grain boundary.

5.3.2 Tensile behavior

The stress-strain curves for the H-free sample and for samples with different hydrogen coverages on the

grain boundary are presented in Figure 5-6. In all samples, irrespective of hydrogen coverage on the

grain boundaries, the stress-strain curves show an upper and lower yield point, which is followed by an

increase in stress with the curves falling to a common value. They also show that the 0.2% offset yield

strength increases with hydrogen coverage on the grain boundaries. This increase in yield strength is

quantified in Figure 5-7, which shows the observed values of the yield strength as a function of H

coverage in the grain boundaries. In order to understand this effect of hydrogen on the grain boundary,

the changes in the grain boundary structure, dislocation emission and crack nucleation and propagation

occurring during the loading were studied. We found that as the emission of dislocations from the grain

boundary proceeds, the tendency for clustering of the H atoms increases. The change in the average

cluster size as a function of strain level is compared with that achieved during the simulation time in the

system with a grain boundary coverage of 4.8 H/nm^2. Only in the presence of strain (see figure 5-8) does

the average number of hydrogen atoms in a cluster increase, there is no change with simulation time.

This comparison indicates that the cluster sizes was not determined by kinetics and that our relaxation

times are adequate.   The dependence of the increase in the average cluster size during loading as a

function of grain boundary hydrogen coverage is shown in Figure 5-9. The higher the coverage the

greater the increase in the average cluster size. This effect is attributed to dislocation emission from the

grain boundary creating additional free volume, which permits larger clusters of hydrogen to form.
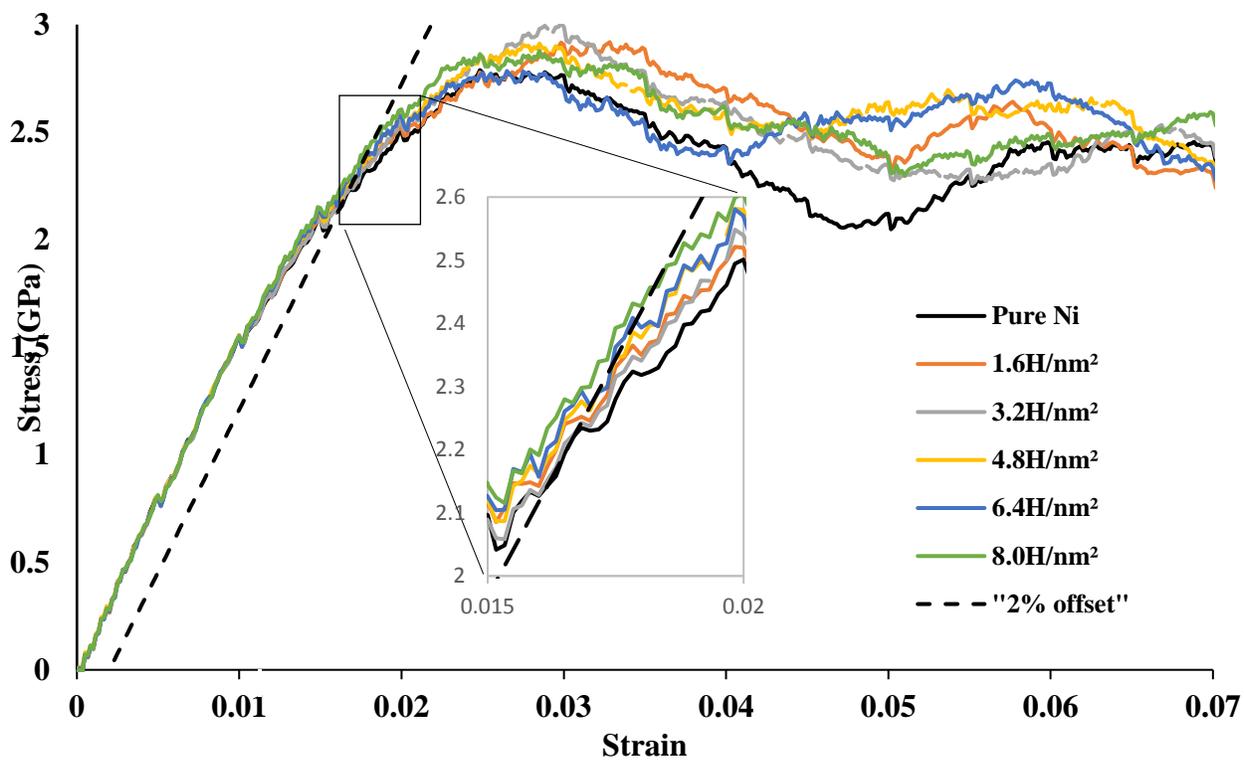
Figure 5-6: Stress-strain behavior of samples with different H coverage levels in the grain boundaries.
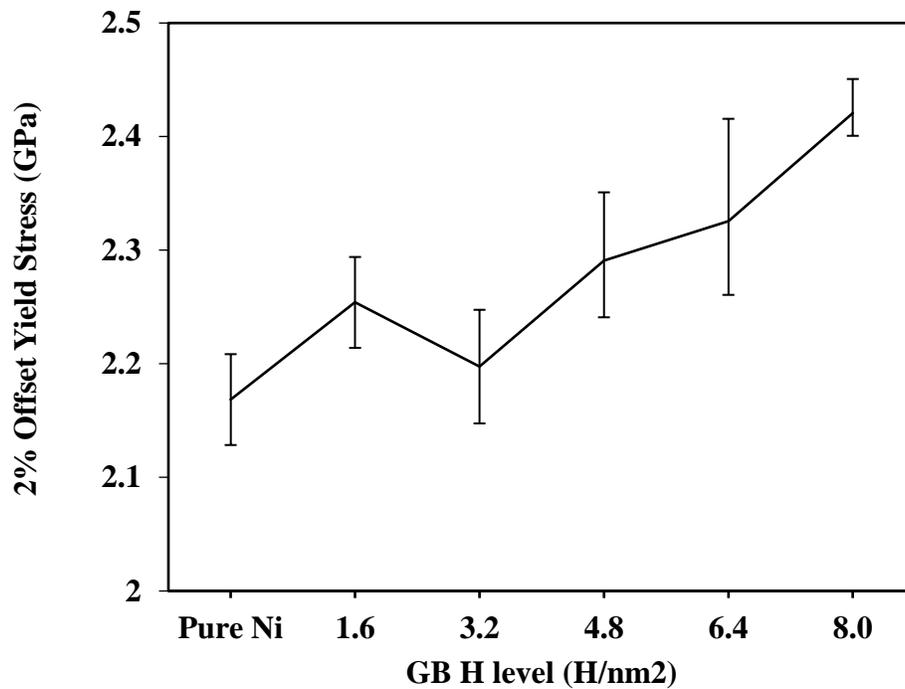
Figure 5-7: Yield stress observed as a function of H coverage in the grain boundary.
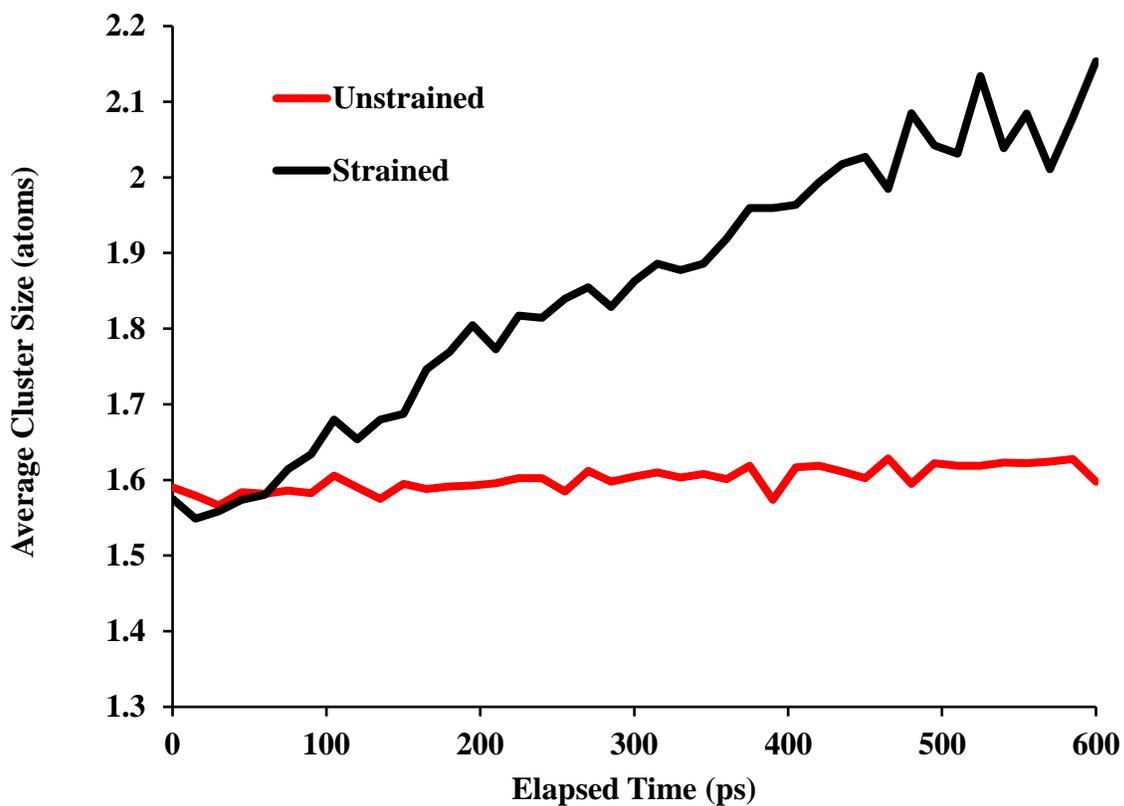
Figure 5-8: Average cluster size in the s ample with 4.8H/nm^2 grain boundary coverage as a function of simulation time with and without applied strain
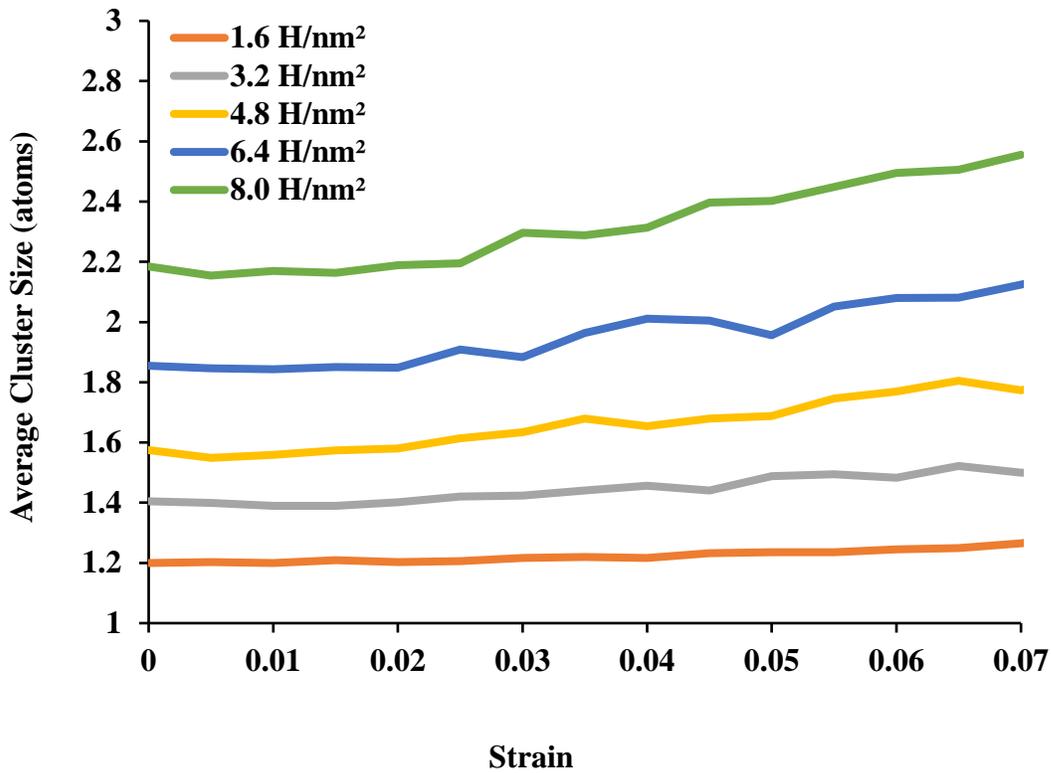
Figure 5-9: Change in average grain boundary hydrogen cluster size as a function of H coverage and applied strain.

5.3.3 Dislocation emission from the grain boundaries

Shockley partial dislocations with Burgers vector of the type <112>/6 were emitted from the grain

boundaries and moved across the grain during loading. This is the typical behavior observed in

simulations without hydrogen, with regions of high free volume in the grain boundary or triple junctions

acting as preferential sites for emission [32, 65]. Figure 5-10a shows an example of the emission of a

Shockley partial dislocation from a site on a grain boundary with a high free volume and hydrogen (black

atoms); the arrows indicate the direction of dislocation motion.   For comparison, the same area is

shown in Figure 5-10b for the sample without hydrogen.
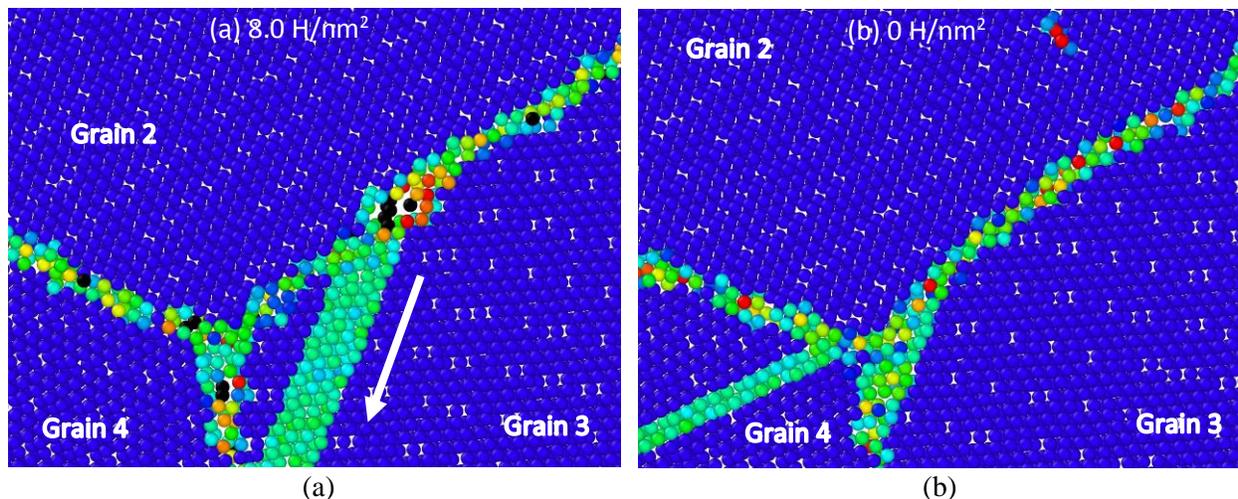
Figure 5-10: (a) A dislocation emitted from H clusters in a grain boundary for 8H/nm^2 grain boundary coverage and 3% strain (a) Emission into grain 3 from the grain boundary between grains 2 and 3. The arrow indicates the direction of motion. (b) The same area for the sample without H.

In order to study the qualitative effects of grain boundary hydrogen, the dislocation density was determined as the deformation proceeds for different H coverage of the grain boundaries. The results are shown in Figure 5-11. Significant plasticity was observed in all samples. The pure Ni sample seems to have a higher dislocation density at very low strain levels, particularly at 1.5%, when only the pure Ni sample has a non-zero mobile dislocation density. This cannot be stated conclusively due to limited resolution, but it is consistent with the finding of an increasing yield stress as the H content of the grain boundary is increased. At strain levels of 2% and above, this is no longer the case and the trend is for the dislocation content to increase with higher H content on the grain boundary. These results support the idea of hydrogen-enhanced generation of dislocations from grain boundary sources, which is consistent with the hydrogen-enhanced plasticity model [8]. As the deformation proceeds, the total dislocation density increased slightly with increased hydrogen coverage.
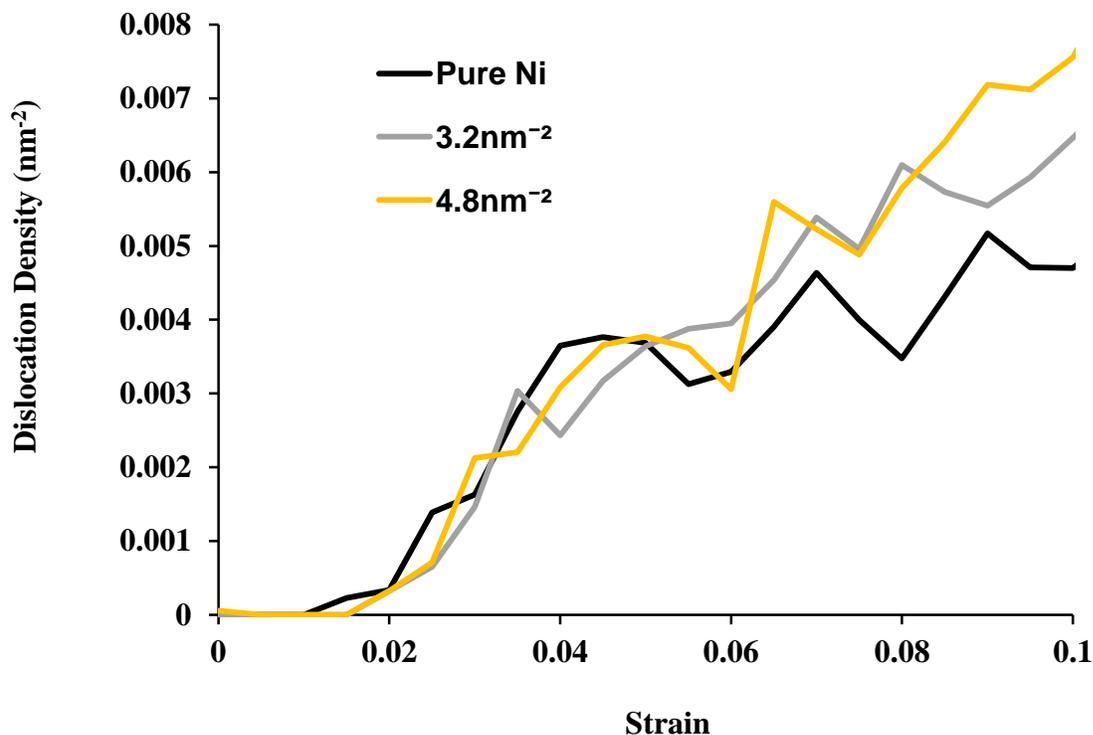
Figure 5-11: Evolution of the dislocation density as a function of strain for samples without H and two different levels of H grain boundary coverage.

The overall distribution of dislocations in the H-free sample is compared to that in samples with

hydrogen coverages of 3.2 H/nm^2 and 4.8 H/nm^2 in Figure 5-12. The dislocations are identified using the

DXA algorithm [56] and colored according to the magnitude of their Burgers vector; Shockley partial

dislocations (Burgers vector ⅙<112>) are colored yellow, perfect dislocations (½<110>) in green and

Lomer-Cottrell sessile dislocations (⅙<110>) in red. In comparing the H-free to the H-containing cases it

is seen that the slip system activation sites in the grain boundary are not necessarily the same and those

that are common are not activated at the same levels of strain. For example, by comparing the

deformation in each grain at strains of 10 and 15%, it can be seen that the number of slip systems

activated as well as the number of events is greater in the sample with 3.2H/nm^2 than in H-free material

especially in grains 1, 3 and 4. In contrast, the dislocation activity in grain 2 is highest in the H-free case.

102

The near $\sum$ = 3 grain boundary (between grains 4 and 6) shows little activity irrespective of the presence of hydrogen although it is noted that the plane normal of this grain boundary is perpendicular to the loading direction. Assessing the influence on the deformation processes of increasing the hydrogen coverage to 4.8 H/nm^2 is complicated as at 10% strain a crack nucleates on the junction between grains 1, 2, 4 and 5. Nevertheless the majority of dislocation activity still occurs in grains 1, 3 and 4. However, this comparison indicates that the grain boundary cracking occurs at lower strains with increasing coverage of hydrogen.
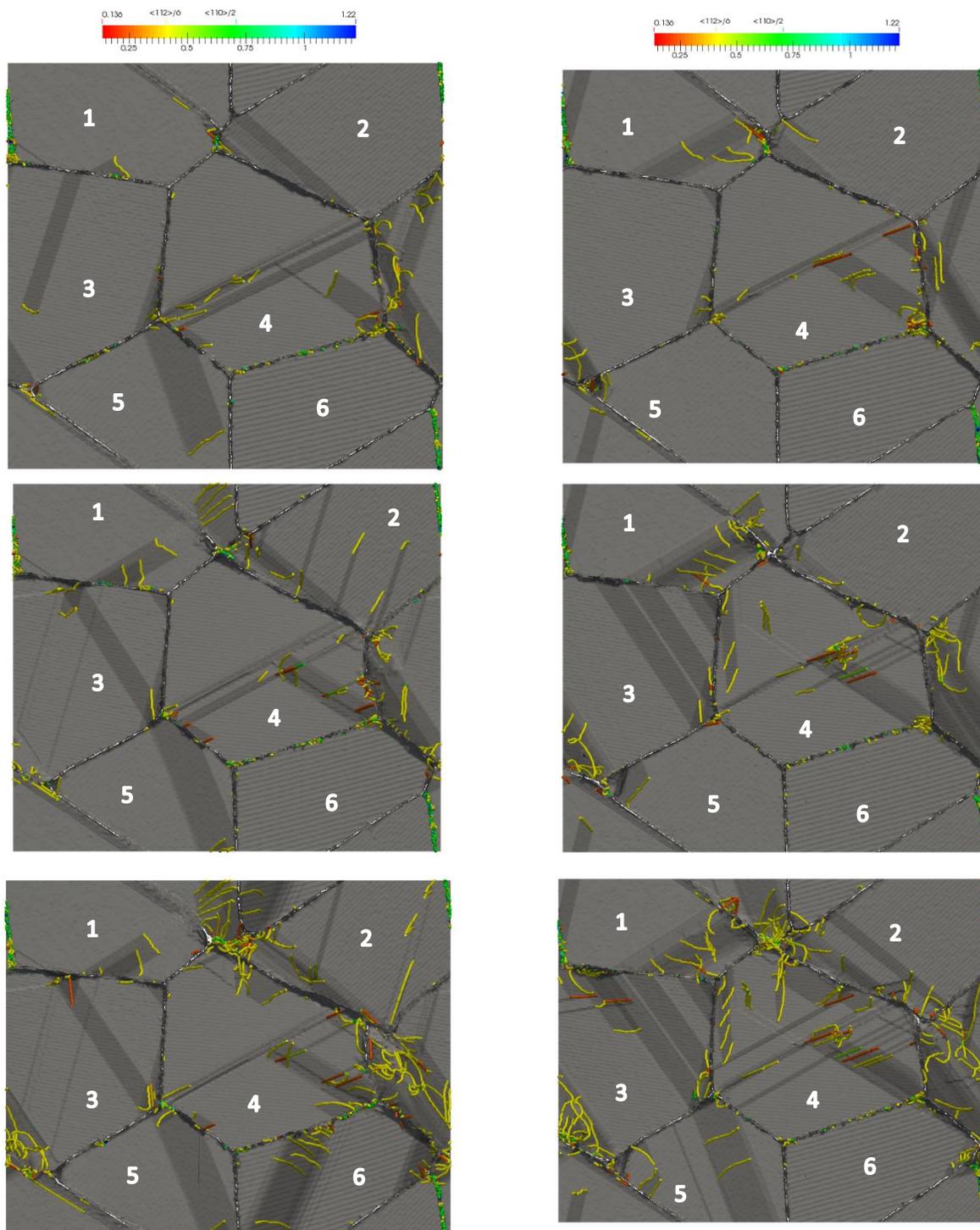
Figure 5-12: Dislocation structures observed for samples without grain boundary H (left) and 3.2 H/nm² (right). Dislocations with burgers vector ⅙<112> are yellow, ½<110> are green, and ⅙<110> are red. Darker gray shaded areas are stacking faults. Deformation levels are 5% 10% and 15% from top.

5.3.4 Crack Initiation and propagation

In assessing the influence of hydrogen on intergranular fracture it is necessary to separate the effects on

crack nucleation and crack propagation. As demonstrated in Figure 5-13, crack initiation on the grain

boundary was relatively insensitive to hydrogen coverage, with embryonic cracks or excess free volume

of length 1 to 2 nm starting to appear at a strain level of about 5% irrespective of hydrogen content. It

should be noted that all observed cracks were surface cracks that nucleated at triple junctions. As

demonstrated in Figure 5-13, crack initiation on the grain boundary was relatively insensitive to

hydrogen coverage, with embryonic cracks or excess free volume of length 1 to 2 nm starting to appear

at a strain level of about 5% irrespective of hydrogen content. This stands in contrast to the results of

Chandler and coworkers, who found that the presence of H reduced the strain at which interior void

nucleation occurred from around 0.25 to as little as 0.15 [27].   In the current work, the crack

propagation rate was influenced by the hydrogen coverage on the grain boundary, increasing with

increasing hydrogen coverage. These effects are captured in Figure 5-13, which shows the length of the

largest crack observed as a function of hydrogen coverage and strain level. Furthermore, at a hydrogen

coverage of 8 H/nm^2 a crack propagated through the sample thickness after 7% strain as opposed to

20% strain in the H-free case. The cracks develop in a "quasi-brittle" manner, growing intergranularly

but with significant plasticity associated with crack advance; this result is consistent with findings both

experimental [66] and simulated [26, 67].   The snapshots presented in Figure 5-14 show crack

nucleation and growth in the sample with hydrogen coverage of 4.8 H/nm^2. The first crack (Fig. 5-14a)

develops at 10% deformation at the junction between grains 1, 2, 4, and 5. A larger crack is shown in

Figure 5-14b, which nucleated between grains 2, 3 and 6 and propagated along the grain boundary

between grains 3 and 4, and for a short distance along the boundary between grains 4 and 2.   Both

cracks nucleate in a region of high dislocation activity and close to the location at which a dislocation

105

pile-up forms against the boundary between grains 2 and 3.   We have observed a limited number of

cracks, but these examples point out to the fact that they tend to develop in regions where there are

dislocation pile-ups against the H containing boundary or triple junction.
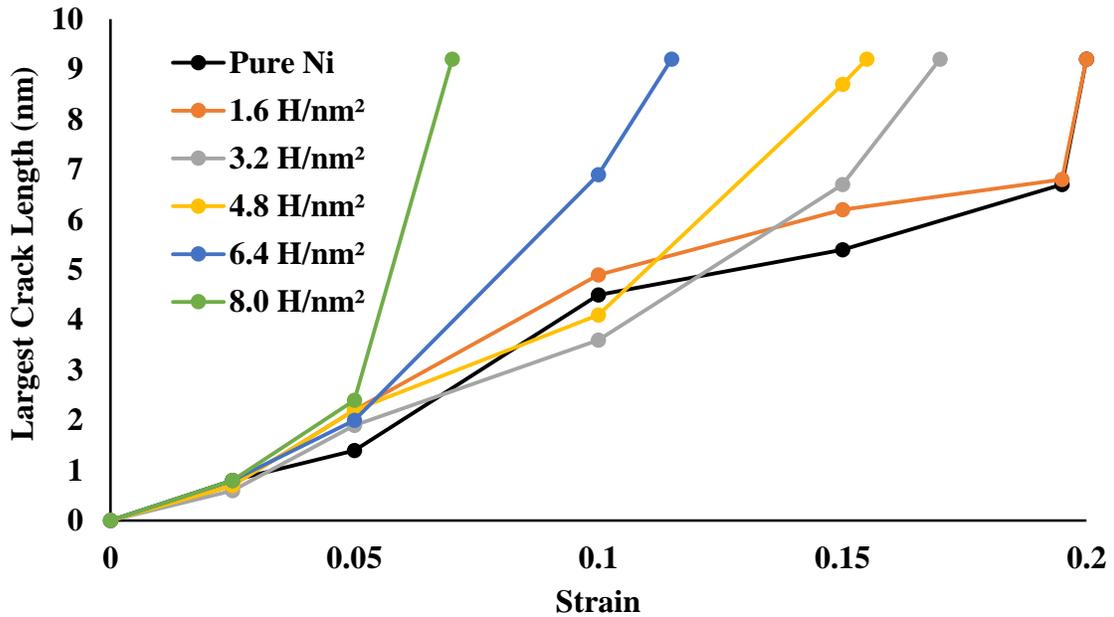
Figure 5-13: Crack initiation and growth as a function of applied strain for various levels of H coverage of the grain boundary.
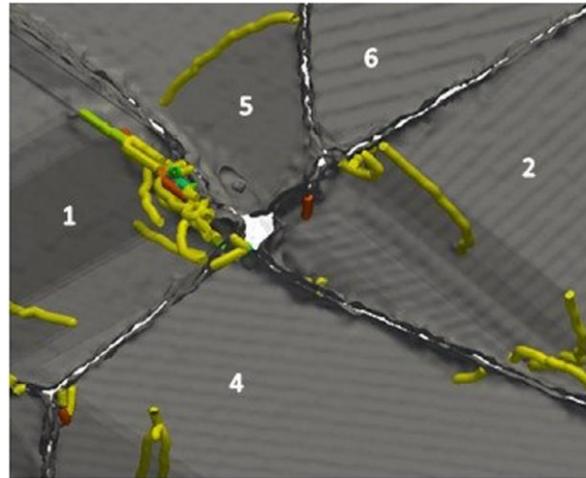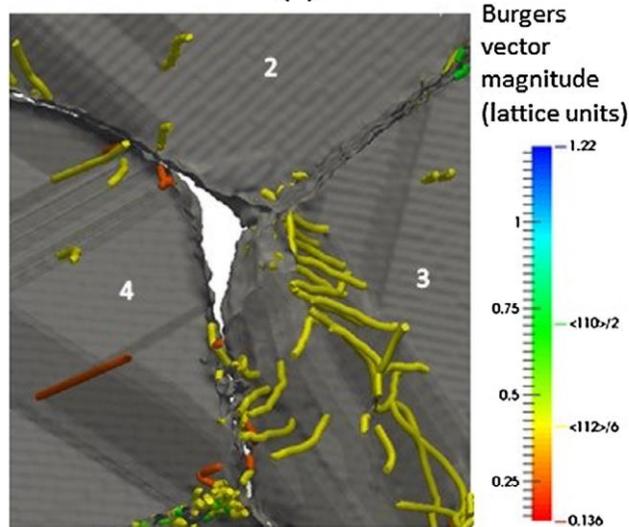
Figure 5-14: Dislocation pile ups and crack initiation observed (a) 4.8 H/nm² deformed 10% a crack starts to nucleate near the triple junction of grains 1, 2 and 4 (b) 4.8 H/nm² deformed 15% . A crack nucleates and grows near the triple junction of grains 2,3 and 4. Dislocations with Burgers vector ⅙<112> are yellow, ½<110> are green, and ⅙<110> are red. Darker gray shaded areas are stacking faults. Both cracks appear at sites where dislocations pile up against a boundary.

5.4 Discussion

The results presented in this work represent the first study of the dependence of grain boundary

hydrogen coverage on the deformation and failure response on a Ni polycrystalline sample. Although

subject to the intrinsic limitations of empirical interatomic potentials and the molecular dynamics simulation technique, the simulations indicate that the presence of hydrogen on the grain boundaries has the following consequences:

1. The introduction of hydrogen on a grain boundary results in changes to the grain boundary structure.

2. Hydrogen clusters form in regions of high free volume in the grain boundary.

3. The yield strength increases with increasing hydrogen coverage on the grain boundary. All samples irrespective of the hydrogen content on the grain boundary show the presence of an upper and lower yield point.

4. After yielding, the emission of dislocations from some grain boundaries is enhanced by the presence of hydrogen.

5. The free volume available in the grain boundary can change with dislocation emission, which in turn influences the clustering of hydrogen in the grain boundary and the emission of dislocations.

6. Crack propagation along the grain boundary but not crack initiation is enhanced by the presence of hydrogen.

7. The strain to failure, or for an intergranular crack to extend through the simulation sample, decreased in the presence of hydrogen and was dependent on the hydrogen coverage in the grain boundary.

Before considering these findings it is instructive to compare them with experimental observations of hydrogen effects on the deformation and failure of Ni. Experimentally it is found that the presence of hydrogen in Ni can cause the transition in failure mode from transgranular to intergranular and that the

percentage of intergranular fracture is dependent on the hydrogen concentration on the grain boundaries [68, 69], although the specific hydrogen concentration needed on each grain boundary to cause intergranular failure remains unknown. The results of these simulations show the same trend. The presence of hydrogen has been shown to cause a loss of ductility, an increase in flow stress and in increase in the work hardening rate of polycrystalline Ni. [70]. These effects were not apparent in the simulation results, likely due to the highly localized nature of atomistic simulation in contrast to the average of many local effects seen in experiment. In-situ straining of Ni in a controlled environment transmission electron microscope shows an increase in the generation of dislocations and an increase in the dislocation mobility [71]. A transition in the failure mode occurred in these in-situ experiments when S was present in the grain boundaries [72]. These effects of hydrogen are combined to explain the observation that the evolved dislocation structure beneath hydrogen-induced intergranular facets in Ni are more refined and the dislocation density higher than expected for the observed strain to failure [6]. This study proposed that the structure and hydrogen content of the grain boundary were altered by the interactions of hydrogen-bearing dislocations with the grain boundary during the process of slip transfer. The hydrogen-enhanced dislocation generation and mobility was responsible for accelerating the evolution of the microstructure observed beneath the striations and thereby altering the local stress state on the grain boundary.

The differences in the stress-strain behavior between these simulations and the experimental results can be attributed to the differences in the methodology, the form of the samples, locating the hydrogen only on the grain boundaries, retaining the hydrogen coverage in the grain boundary constant, and the test conditions. The initial increase in the stress required to emit a dislocation from a grain boundary can be attributed to hydrogen occupying sites of free volume, which have been shown to be the sites for dislocation emission in the absence of hydrogen [65]. However, once activated these sites emit more dislocations when hydrogen is present although this is not due to a decrease in the stress to activate the

grain boundary dislocation source as the lower yield point does not change significantly with hydrogen coverage. This finding is consistent with experimental findings of hydrogen-enhanced dislocation generation [39, 73] as well as slip transfer across grain boundaries [6, 7, 74]. However, both the simulations and experiments find that the strain to failure is reduced in the presence of hydrogen on the grain boundaries and decreases with increasing hydrogen concentration. For example, Ni-201 containing 2000 ppm of internal hydrogen, exhibited a strain to failure of just 13% [70].

The change in the structure of the grain boundary simply due to the introduction of hydrogen and its further modification through the emission of dislocations provides new insight as to how hydrogen and the plasticity could combine to cause the cohesive strength of a specific grain boundary to become the weak link in the system and therefore the preferred site for crack nucleation. Experimentally the increase in disorder or free volume in the grain boundary is inferred from observed structural changes in the grain boundary following dislocation interactions with it. However, the connection of dislocation emission to regions of high free volume has not been achieved experimentally. Once nucleated a crack propagates along the weakest grain boundary provided it experienced an appropriate level of stress. This observation raises the interesting question about the level of coverage of hydrogen that is needed on the grain boundary for the presence of hydrogen alone to reduce the cohesive strength sufficiently to make it the weakest link in the system. It also suggests that the reduction in the cohesive strength necessary to make a grain boundary the weakest link is, for the same hydrogen coverage, dependent on the grain boundary type. Unfortunately, studies to assess the magnitude of the grain boundary cohesive energy as a function of hydrogen content and grain boundary type are not common. Most studies have shown that the ideal work of separation decreases almost linearly with increasing hydrogen coverage, dropping by ~45% at one-half monolayer of hydrogen coverage [75, 76]. However, these studies neglect plasticity effects prior to crack initiation and have not been conducted as a function of grain boundary type. Shuai et al. have reported that the magnitude of the reduction of the cohesive energy of grain

boundaries as a function of hydrogen coverage in Fe is sensitive to the grain boundary type [77]. They have questioned if the levels attainable under experimental hydrogen charging conditions will yield the coverages necessary to reduce the cohesive strength sufficiently. Our results show that significant effects on dislocation emission are already observed for a coverage of 3.2 H/nm^2 corresponding to approximately 15% of a monolayer.

Our results indicate that beyond the compositional effect of hydrogen on the grain boundary cohesion, structural effects on the grain boundary due to hydrogen and the deformation process can play a critical role. Martin et al. [6] and Wang et al. [7] introduced the concept of a increased structural disorder due to hydrogen-enhanced slip transfer across grain boundaries as contributing to the reduction of the cohesive strength of the grain boundary. Similarly, in the case of liquid metal embrittlement it has been suggested that structural as well as compositional changes to the grain boundary are responsible for the failure path being along grain boundaries [78, 79].

Our results also suggest preferential crack growth at sites at which a dislocation pile-up impinges on the grain boundary and the dislocations are not accommodated in the grain boundary. For random boundaries, these pile-ups contain increased number of dislocations for increased hydrogen coverage. As the magnitude of the stress ahead of a dislocation pile-up is related to the number of dislocations in it, this result implies an increase in the local stress state at the grain boundary. As the simulations only allow for faster dislocation emission from grain boundary sources, the actual effect is expected to be greater and to develop more rapidly when the effect of hydrogen on the dislocation mobility is included. This increase in the local stress at the grain boundary supports the interpretation of experimental findings summarized recently by Robertson [8].

5.5 Conclusions

Based on these simulations the following conclusions can be drawn: H impurities that segregate to the grain boundaries change the grain boundary structure, creating regions of high free volume at the sites of H clusters. H in the grain boundaries, especially at regions of high free volume, constitute favored sites for dislocation nucleation. A positive trend in yield strength was observed, wherein more H caused initial yield to occur at higher stress levels. This effect can be caused by H occupying the free volume in the boundaries. This trend seems to be reversed for higher deformation levels with dislocation density values enhanced by the addition of hydrogen in the sample grain boundaries. This occurs for stresses when the H filled sites are activated for dislocation emission. Once cracks are nucleated in the grain boundaries, their growth is greatly enhanced by the presence of intergranular hydrogen. The presence of dislocation pile-ups in random grain boundaries is enhanced by hydrogen. Significant plasticity due to enhanced emission of dislocations from grain boundary sources is observed in the presence of hydrogen, even as cracks nucleate and grow. Crack growth seems to be enhanced in locations where the dislocations pile up against the boundaries.

Acknowledgements:

References

1.   Gangloff, R.P., *Science-based prognosis to manage structural alloy performance in hydrogen*, in *Proceedings of the 2008 International Hydrogen Conference - Effects of Hydrogen on Materials*, B. Somerday, P. Sofronis, and R. Jones, Editors. 2009, ASM International: Jackson Hole, Wyoming. p. 1-21.

2.   Robertson, I.M., D. Lillig, and P.J. Ferreira, *Revealing the fundamental processes controlling hydrogen embrittlement.*, in *Proceedings of the 2008 International Hydrogen Conference - Effects of Hydrogen on Materials*, B. Somerday, P. Sofronis, and R. Jones, Editors. 2009, ASM International: Jackson Hole, Wyoming. p. 22 -37.

3.   Bechtle, S., et al., *Grain-boundary engineering markedly reduces susceptibility to intergranular hydrogen embrittlement in metallic materials.* Acta Materialia, 2009. **57**(14): p. 4148-4157.

4.   McMahon Jr, C.J., *Hydrogen-induced intergranular fracture of steels.* Engineering Fracture Mechanics, 2001. **68**(6): p. 773-788.

5.   McMahon Jr, C.J., *Brittle fracture of grain boundaries.* Interface Science, 2004. **12**(2-3): p. 141-146.

6.   Martin, M.L., et al., *Hydrogen-induced intergranular failure in nickel revisited.* Acta Materialia, 2012. **60**(6-7): p. 2739-2745.

7.   Wang, S., et al., *Hydrogen-induced intergranular failure of iron.* Acta Materialia, 2014. **69**: p. 275-282.

8.   Robertson, I.M., et al., *Hydrogen Embrittlement Understood.* Metallurgical and Materials Transactions a-Physical Metallurgy and Materials Science, 2015. **46A**(6): p. 2323-2341.

9.   Van Swygenhoven, H., A. Caro, and D. Farkas. *Grain boundary structure and its influence on plastic deformation of polycrystalline FCC metals at the nanoscale: A molecular dynamics study*. in *5th International Conference on Nanostructured Materials (NANO 2000)*. 2000. Sendai, Japan.

10.   Van Swygenhoven, H., A. Caro, and D. Farkas. *A molecular dynamics study of polycrystalline fcc metals at the nanoscale: grain boundary structure and its influence on plastic deformation*. in *International Conference on the Fundamentals of Plastic Deformation*. 2000. Gaithersburg, Maryland.

11.   Van Swygenhoven, H., D. Farkas, and A. Caro, *Grain-boundary structures in polycrystalline metals at the nanoscale.* Physical Review B, 2000. **62**(2): p. 831-838.

12.   Wolf, D., et al., *Deformation of nanocrystalline materials by molecular-dynamics simulation: Relationship to experiments?* Acta Materialia, 2005. **53**(1): p. 1.

13.   Wolf, D., et al., *Deformation mechanism and inverse Hall-Petch behavior in nanocrystalline materials.* Zeitschrift Fur Metallkunde, 2003. **94**(10): p. 1091-1097.

14.   Sansoz, F. and J.F. Molinari, *Mechanical behavior of Sigma tilt grain boundaries in nanoscale Cu and Al: A quasicontinuum study.* Acta Materialia, 2005. **53**(7): p. 1931-1944.

15.   Mishin, Y., M. Asta, and J. Li, *Atomistic modeling of interfaces and their impact on microstructure and properties.* Acta Materialia, 2010. **58**(4): p. 1117-1151.

16.   McDowell, D.L., *A perspective on trends in multiscale plasticity.* International Journal of Plasticity, 2010. **26**(9): p. 1280-1309.

17.   Cao, A.J. and Y.G. Wei, *Molecular dynamics simulation of plastic deformation of nanotwinned copper.* Journal of Applied Physics, 2007. **102**(8).

18.   Vo, N.Q., et al., *Quantitative description of plastic deformation in nanocrystalline Cu: Dislocation glide versus grain boundary sliding.* Physical Review B, 2008. **77**(13).

19.   Farkas, D., *Atomistic simulations of metallic microstructures.* Current Opinion in Solid State & Materials Science, 2013. **17**(6): p. 284-297.

20.   Piaggi, P.M., et al., *Hydrogen diffusion and trapping in nanocrystalline tungsten.* Journal of Nuclear Materials, 2015. **458**: p. 233-239.

21.   Yu, Y., et al., *Molecular dynamics simulation of hydrogen dissolution and diffusion in a tungsten grain boundary.* Journal of Nuclear Materials, 2014. **455**(1-3): p. 91-95.

22.   Wang, H., D.S. Xu, and R. Yang, *Atomic modelling of crack initiation on twin boundaries in alpha-titanium under external tensile loading along various orientations.* Philosophical Magazine Letters, 2014. **94**(12): p. 779-785.

23.   Song, J. and W.A. Curtin, *Mechanisms of hydrogen-enhanced localized plasticity: An atomistic study using alpha-Fe as a model system.* Acta Materialia, 2014. **68**(15): p. 61-69.

24.   Song, J. and W.A. Curtin, *Atomic mechanism and prediction of hydrogen embrittlement in iron.* Nature Materials, 2013. **12**(2): p. 145-151.

25.   Shim, J.H., et al., *Atomistic simulation of hydrogen diffusion at tilt grain boundaries in vanadium.* Metals and Materials International, 2013. **19**(6): p. 1221-1225.

26.   Solanki, K.N., D.K. Ward, and D.J. Bammann, *A Nanoscale Study of Dislocation Nucleation at the Crack Tip in the Nickel-Hydrogen System.* Metallurgical and Materials Transactions a-Physical Metallurgy and Materials Science, 2011. **42a**(2): p. 340-347.

27.   Chandler, M.Q., et al., *Hydrogen effects on nanovoid nucleation at nickel grain boundaries.* Acta Materialia, 2008. **56**(3): p. 619-631.

28.   Ruda, M., D. Farkas, and J. Abriata, *Atomistic simulation of H effects in metals and intermetallics.* Hydrogen Energy Progress Xii, Vols 1-3, 1998: p. 2199-2206.

29.   Ruda, M., D. Farkas, and J. Abriata, *Embedded-atom interatomic potentials for hydrogen in metals and intermetallic alloys.* Physical Review B, 1996. **54**(14): p. 9765-9774.

30.   Farkas, D., et al., *Atomistic simulations of the effects of segregated elements on grain-boundary fracture in body-centered-cubic Fe.* Metallurgical and Materials Transactions a-Physical Metallurgy and Materials Science, 2005. **36A**(8): p. 2067-2072.

31.   Geng, W.T., et al., *Embrittling and strengthening effects of hydrogen, boron, and phosphorus on a Sigma 5 nickel grain boundary.* Physical Review B, 1999. **60**(10): p. 7149-7155.

32.   Hickel, T., et al., *Ab Initio Based Understanding of the Segregation and Diffusion Mechanisms of Hydrogen in Steels.* Jom, 2014. **66**(8): p. 1399-1405.

33.   Birnbaum, H.K. and P. Sofronis, *Hydrogen-enhanced localized plasticity-a mechanism for hydrogen-related fracture.* Mater. Sci. Eng. A, Struct. Mater., Prop. Microstruct. Process., 1994. **A176**(1- 2): p. 191-202.

34.   Song, J., M. Soare, and W.A. Curtin, *Testing continuum concepts for hydrogen embrittlement in metals using atomistics.* Modelling and Simulation in Materials Science and Engineering, 2010. **18**(4): p. 045003.

35.   McMahon Jr, C.J., *Intergranular brittleness in iron.* Acta Metallurgica, 1966. **14**(7): p. 839-845.

36.   Dadfarnia, M., et al., *Recent Advances in the Study of Structural Materials Compatibility with Hydrogen.* Advanced Materials, 2010. **22**(10): p. 1128-1135.

37.   Delafosse, D. and T. Magnin, *Hydrogen induced plasticity in stress corrosion cracking of engineering systems.* Engineering Fracture Mechanics, 2001. **68**(6): p. 693-729.

38.   Mei Qiang, C., J.B. Douglas, and M.F. Horstemeyer, *A continuum model for hydrogen-assisted void nucleation in ductile materials.* Modelling and Simulation in Materials Science and Engineering, 2013. **21**(5): p. 055028.

39.   Robertson, I.M., H.K. Birnbaum, and P. Sofronis, *Hydrogen Effects On Plasticity*, in *Dislocations in Solids*, J.P. Hirth and L. Kubin, Editors. 2009, Elsevier: New York. p. 249-293.

40.   Abraham, D.P. and C.J. Altstetter, *Hydrogen-enhanced localization of plasticity in an austenitic stainless steel.* Metallurgical and Materials Transactions A (Physical Metallurgy and Materials Science), 1995. **26A**(11): p. 2859.

41.   Wang, S., et al., *Activation volume and density of mobile dislocations in hydrogen-charged iron.* Acta Materialia, 2013. **61**(13): p. 4734-4742.

42.   Song, J. and W.A. Curtin, *A nanoscale mechanism of hydrogen embrittlement in metals.* Acta Materialia, 2011. **59**(4): p. 1557-1569.

43.   Li, S., et al., *The interaction of dislocations and hydrogen-vacancy complexes and its importance for deformation-induced proto nano-voids formation in α-Fe.* International Journal of Plasticity, 2015. **- 74**(-): p. - 191.

44.   Neeraj, T., R. Srinivasan, and J. Li, *Hydrogen embrittlement of ferritic steels: Observations on deformation microstructure, nanoscale dimples and failure by nanovoiding.* Acta Materialia, 2012. **60**(13-14): p. 5160-5171.

45.   Srinivasan, R. and T. Neeraj, *Hydrogen Embrittlement of Ferritic Steels: Deformation and Failure Mechanisms and Challenges in the Oil and Gas Industry.* Jom, 2014. **66**(8): p. 1377-1382.

46.   Martin, M.L., I.M. Robertson, and P. Sofronis, *Interpreting hydrogen-induced fracture surfaces in terms of deformation processes: A new approach.* Acta Materialia, 2011. **59**(9): p. 3680-3687.

47.   Daw, M.S. and M.I. Baskes, *Semiemperical, Quantum-Mechanical Calculation of Hydrogen Embrittlement in Metals.* Physical Review Letters, 1983. **50**(17): p. 1285-1288.

48.   Daw, M.S. and M.I. Baskes, *Embedded-Atom Method - Derivation and Application to Impurities, Surfaces, and Other Defects in Metals.* Physical Review B, 1984. **29**(12): p. 6443-6453.

49.   Voter, A.F., Chen, S.P, *High temperature ordered intermetallic alloys*
MRS Symposia Proceedings, 1987. **82**: p. 175.

50.   Ramasubramaniam, A., M. Itakura, and E.A. Carter, *Interatomic potentials for hydrogen in alpha-iron based on density functional theory.* Physical Review B, 2009. **79**(17).

51.   Van Swygenhoven, H., et al., *Competing plastic deformation mechanisms in nanophase metals.* Physical Review B, 1999. **60**(1): p. 22--25.

52.   Van Swygenhoven, H., A. Caro, and D. Farkas, *A molecular dynamics study of polycrystalline fcc metals at the nanoscale: grain boundary structure and its influence on plastic deformation.* Materials Science and Engineering a-Structural Materials Properties Microstructure and Processing, 2001b. **309**: p. 440-444.

53.   Plimpton, S., *Fast Parallel Algorithms for Short-Range Molecular-Dynamics.* Journal of Computational Physics, 1995. **117**(1): p. 1-19.

54.   Kelchner, C.L., S.J. Plimpton, and J.C. Hamilton, *Dislocation nucleation and defect structure during surface indentation.* Physical Review B, 1998. **58**(17): p. 11085-11088.

55.   Stukowski, A., *Visualization and analysis of atomistic simulation data with OVITO-the Open Visualization Tool.* Modelling and Simulation in Materials Science and Engineering, 2010. **18**(1).

56.   Stukowski, A. and K. Albe, *Extracting dislocations and non-dislocation crystal defects from atomistic simulation data.* Modelling and Simulation in Materials Science and Engineering, 2010. **18**(8).

57.   Henderson, A., *ParaView Guide, A Parallel Visualization Application.*
Kitware Inc. 2007.

58.   Harris, T.M. and R.M. Latanision, *Grain-Boundary Diffusion of Hydrogen in Nickel.* Metallurgical Transactions a-Physical Metallurgy and Materials Science, 1991. **22**(2): p. 351-355.

59.   Brass, A.M. and A. Chanfreau, *Accelerated diffusion of hydrogen along grain boundaries in nickel.* Acta Materialia, 1996. **44**(9): p. 3823-3831.

60.   Pedersen, A. and H. Jonsson, *Simulations of hydrogen diffusion at grain boundaries in aluminum.* Acta Materialia, 2009. **57**(14): p. 4036-4045.

61.   Oudriss, A., et al., *Grain size and grain-boundary effects on diffusion and trapping of hydrogen in pure nickel.* Acta Materialia, 2012. **60**(19): p. 6814-6828.

62.   Oudriss, A., et al., *The diffusion and trapping of hydrogen along the grain boundaries in polycrystalline nickel.* Scripta Materialia, 2012. **66**(1): p. 37-40.

63.   Hoch, B.O., et al., *Effects of grain-boundary networks on the macroscopic diffusivity of hydrogen in polycrystalline materials.* Computational Materials Science, 2015. **97**: p. 276-284.

64.   Geng, W.T., et al., *Hydrogen-promoted grain boundary embrittlement and vacancy activity in metals: Insights from ab initio total energy calculatons.* Materials Transactions, 2005. **46**(4): p. 756-760.

65.   Farkas, D. and L. Patrick, *Tensile deformation of fcc Ni as described by an EAM potential.* Philosophical Magazine, 2009. **89**(34-36): p. 3435-3450.

66.   Alvaro, A., et al., *Hydrogen embrittlement in nickel, visited by first principles modeling, cohesive zone simulation and nanomechanical testing.* International Journal of Hydrogen Energy, 2015. **40**(47): p. 16892-16900.

67.   Barrows, W., R. Dingreville, and D. Spearot, *Traction-separation relationships for hydrogen induced grain boundary embrittlement in nickel via molecular dynamics simulations.* Materials Science and Engineering a-Structural Materials Properties Microstructure and Processing, 2016. **650**: p. 354-364.

68.   Lassila, D.H. and H.K. Birnbaum, *The effect of diffusive segregation on the fracture of hydrogen charged nickel.* Acta Metall., 1988. **36**(10): p. 2821-5.

69.   Lassila, D.H. and H.K. Birnbaum, *Intergranular fracture of nickel: the effect of hydrogen-sulphur co-segregation.* Acta Metall., 1987. **35**(7): p. 1815-22.

70.   Wilcox, B.A. and G.C. Smith, *Intercrystalline Fracture in Hydrogen-Charged Nickel.* Acta Metallurgica, 1965. **13**(3): p. 331-&.

71.   Robertson, I.M. and H.K. Birnbaum, *HVEM study of hydrogen effects on the deformation and fracture of nickel.* Acta Metallurgica, 1986. **34**(3): p. 353-366.

72.   Lee, T.C., I.M. Robertson, and H.K. Birnbaum, *An HVEM in situ deformation study of nickel doped with sulfur.* Acta Metallurgica, 1989. **37**(2): p. 407-15.

73.   Robertson, I.M., *The effect of hydrogen on dislocation dynamics.* Engineering Fracture Mechanics, 2001. **68**(6): p. 671-692.

74.   Robertson, I., et al., *Hydrogen Embrittlement Understood.* Metallurgical and Materials Transactions A, 2015: p. 1-19.

75.   Jiang, D.E. and E.A. Carter, *First principles assessment of ideal fracture energies of materials with mobile impurities: implications for hydrogen embrittlement of metals.* Acta Materialia, 2004. **52**(16): p. 4801-4807.

76.   Lassila, D.H. and H.K. Birnbaum, *The Effect of Diffusive Hydrogen Segregation on Fracture of Polycrystalline Nickel.* Acta Metallurgica, 1986. **34**(7): p. 1237-1243.

77.   Wang, S., et al., *Effect of hydrogen environment on the separation of Fe grain boundaries.* Acta Materialia, 2015. **under review**.

78.   Luo, J., et al., *The Role of a Bilayer Interfacial Phase on Liquid Metal Embrittlement.* Science, 2011. **333**: p. 1730.

79.   Martin, M.L., et al., *Liquid-metal-induced fracture mode of martensitic T91 steels.* Journal of Nuclear Materials, 2012. **426**(1-3): p. 71-77.

CHAPTER 6: NI NANOINDENTATION AT THE NANOSCALE: ATOMIC ARRANGEMENTS AT THE NI-C INTERFACE

F. Tavazza[1], B. Kuhr[2], D. Farkas[2], L.E. Levine[1]

[1] National Institute of Standards and Technology, Materials Science and Engineering Division, 100 Bureau Drive, Gaithersburg, Maryland 20899, USA

[2] Department of Materials Science and Engineering, Virginia Polytechnic Institute and State University, 213 Holden Hall 445 Old Turner Street Blacksburg, VA 24061

Abstract

As mechanical testing proceeds towards ever-decreasing length scales, the ultimate limit is the atomic scale. Here, we investigate the atomic-scale interactions that occur at the diamond-nickel interface during the earliest stages of a Ni nanoindentation measurement. Using molecular dynamics with a custom-designed empirical potential, we found that, irrespective of the Ni orientation, the same Ni-C interfacial structure always formed between the substrate and the diamond indenter. As the indenter digs deeper into the specimen, the location of the Ni-C interface changes, but its structure never does. In addition, the local formation of this structure produces longer-range disorder that may affect the local stresses and activation barriers to dislocation nucleation. As this process requires relatively large atomic displacements of the Ni atoms for some Ni orientations, we used density functional theory calculations to validate and understand the process.

Comments

This manuscript was published in the Journal of Physical Chemistry C [1]. It has been lightly edited for formatting.

1.   Tavazza, F., et al., *Ni Nanoindentation at the Nanoscale: Atomic Rearrangements at the Ni-C Interface.* Journal of Physical Chemistry C, 2017. **121**(5): p. 2643-2651.

6.1 Introduction

Nanoindentation is the most commonly-used technique for probing the mechanical response of samples at the nanometer length scale. When a sharp indenter tip is used, plastic deformation can occur at nanometer-scale indentation depths. For example, Ma *et al.* showed that a diamond Berkovitch indenter tip with a radius of 121 nm ± 11 nm can produce sudden strain bursts (pop-ins) at an average indentation depth of just 11 nm[1]. Experiments with even sharper tips, such as AFM cantilevers[2-7], can probe mechanical behavior at even smaller length scales. The ultimate limit, of course, is the atomic scale and this paper focuses on the detailed atomistic behavior at the diamond-nickel interface during indentation (including tip retraction) of Ni to depths up to about 1.1 nm. For such small indentations, all of the atoms involved may be considered surface or near-surface atoms and the details of the atomic interactions between the metal surface and carbon atoms in the indenter become important. In particular, the detailed response of the Ni atoms near the indenter could affect the dislocation nucleation process through changes in the local stresses and the activation barriers to dislocation nucleation. Here, we investigate the first aspect of this problem for Ni indentation: the Ni-C interaction and its effect on the Ni atomic structure of the interface.

Stress development during indentation and other types of contact have been the subject of vast amounts of experimental and modelling research. The predominant approach to quantifying and mapping stress states during contact has been through continuum methods such as Finite Element Modeling (FEM)[8-11] and analytical variants of the Hertzian contact solutions[12]. While this approach is attractive due to its high flexibility and computational inexpensiveness, it can ignore phenomena that result from the highly discretized nature of the atomic scale.

Molecular dynamics is frequently used in modeling nanoindentation [13-16], and many of these studies employ a continuum model for their indenter, describing it as a force field that is spherically symmetrical about the indenter center[17-23]. Other studies have implemented atomistic indenters[24-27]. One such study[28], showed that use of an atomistic indenter has an effect on dislocation nucleation. By investigating, in depth, the spatial rearrangement of atoms due to chemical effects at the sample indenter interface, it may be possible to identify chemical processes not available through continuum methods that contribute to nanoscale deformation.

To model the deformation as realistically as possible, we used a custom-designed hybrid Ni-C empirical potential, where the Ni-Ni and C-C interactions were described by well tested potentials present in the literature, while the mixed interactions were fitted to density functional theory (DFT) nanoindentation data[29, 30]. In addition, since the detailed chemical interaction between the carbon and nickel atoms is expected to play a role, DFT simulations were used to both validate and interpret the molecular dynamics (MD) results. Multi-scale approaches have been implemented in several other studies of indentation[9, 31-34]

In this paper, after describing the simulation methodology for both methodologies, we discuss the MD findings for the atomic rearrangement that occurs when the C atoms of the indenter come into contact with the Ni surface (Ni-C interface). This is done for various orientations of the Ni specimen ((111), (110) and (100)), various rotations of the indenter tip with respect to the Ni surface, and two temperatures (T = 1 K and T = 300 K). Results obtained using a different atomistic potential (Ruda2002) are discussed as well. The DFT validation comprises the last part of the paper. In this section, we examine the energetics of the observed hexagonal-to-square transformation of the Ni surface atoms as a function of the distance from the indenter tip. Results

119

from much more computationally intensive semistatic DFT simulations of nanoindentation are discussed as well, and further support our MD findings.

6.2 Methodology

Our investigation of the Ni/C interface was conducted using both MD and DFT simulations. MD allowed us to see the formation of the Ni/C interface and how its structure depends on the Ni surface orientation, while DFT allowed us to validate the MD findings as well as to understand the energetic reasons behind the atomic arrangement(s) that MD had suggested.

All of the MD simulations presented in this paper were run using the LAMMPS code[35]. They were conducted in the NVT ensemble and a Nose-Hoover thermostat was employed[36]. We studied two temperatures (T = 1 K and T = 300 K), and three substrate orientations ((111), (110) and (100)) for the Ni sample. We used a time step of 1 fs and, in all cases except when studying indenter retraction, an indenter speed of 0.1 Å/ps (10 m/s), which is among the slowest speeds commonly used in MD nanoindentation simulations[23, 27]. The indenter retraction investigation was run using a slower indenter speed (0.01 Å/ps) to make sure the atoms had plenty of time to completely react to the changes in their environment. The size of the Ni specimen was the same for all orientations (500 Å x 500 Å x 300 Å), which corresponds to 6820800, 6848640 and 6855760 atoms for the (111), (110) and (100) oriented samples, respectively. In all cases, we used periodic boundary conditions along x and y, and a fixed bottom layer of 10 Å along z. The MD simulation cell is shown in Figure 6-1 a), and, as only Ni atoms with centrosymmetry parameter larger than 3 are shown (in blue), only the top and bottom surfaces of the Ni specimen are visible. All the C atoms are displayed (red), so the whole atomistic indenter is depicted in the figure.
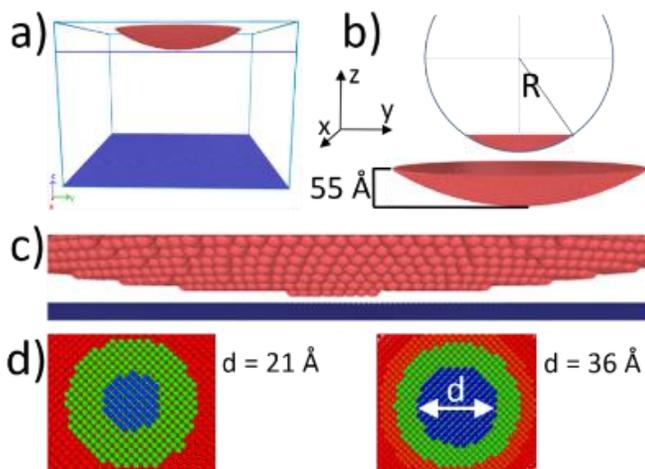
Figure 6-1: a) Simulation cell for all the MD calculations, shown here for a Ni (111) sample. The carbon atoms are red, while the Ni atoms are blue. Only Ni atoms with centrosymmetry > 3 are displayed. The atomistically rough, spherical indenter is displayed in greater detail in b), where the actual indenter is shown with respect to the whole sphere of radius R=29.8 nm, and in c), where the atomic planes the indenter is made of are clearly visible. In d) we show examples of how the indenter tip may change by simply slightly changing the position of the center of the carving sphere with respect to the position of the atomic planes in the diamond lattice when carving the indenter. In d) all atoms are C and different colors only indicate a different atomic plane along z.

The MD indenter was atomically rough and spherical, with a radius of 29.8 nm (Figure 6-1). It was made of individual C atoms and it was carved out of a (100)-diamond lattice. We were only interested in indenting to the point of initiating dislocation nucleation, and preliminary simulations showed that to happen for indentations of less than 2 nm. Therefore, to limit the number of atoms in the system, instead of keeping the whole semi-sphere as an indenter, we kept only its bottom part: a slice that went from the tip to about 55 Å above the tip itself. This indenter contained about 464000 atoms (Figure 6-1 b)). Among the simulations there were small changes in the size of the indenter because we wanted to make sure that our results did not depend on the specific indenter realization. Because of the discrete nature of the lattice, the "atomic" indenter is actually composed of a series of successive plateaus (Figure 6-1 c)) and,

121

therefore, it is possible to obtain very similar realizations (Figure 6-1 d)) by simply slightly

changing, for instance, the position of the center of the carving sphere with respect to the

position of the atomic planes in the diamond lattice. To preserve bulk information, the atoms in

the top 10 Å of our indenter were kept fixed during the simulations at T = 300 K. In most

simulation the atomic rows in the indenter plateaus were oriented parallel to the atomic rows in

the specimen surface. However, as discussed in more detail in section 3, we later removed this

restriction and run several simulations with the atomic rows in the indenter plateaus forming

various angles in the xy plane with the Ni rows, up to 22° (Figure 6-2). This was done to guarantee

that our findings are not dependent on a specific choice of the simulation cell, and, more

specifically, on an initial atomic alignment between indenter and specimen.
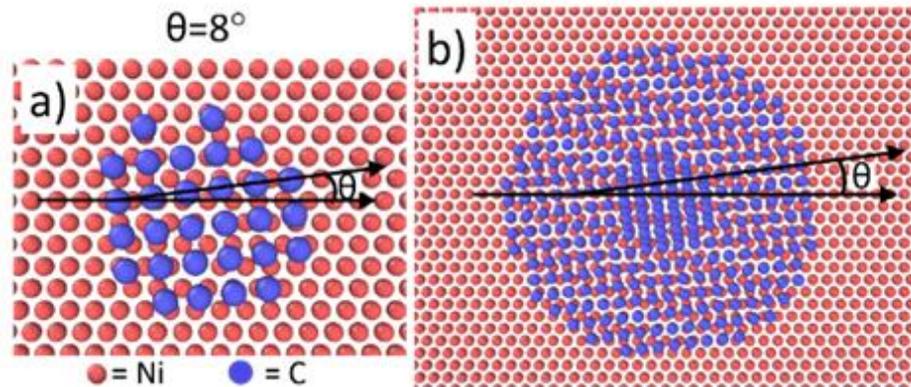
Figure 6-2: Example of initial positions with a slight rotation between the atomic rows formed by Ni surface atoms (Ni (111)) and those in the indenter tip. Only the lowest plane in the indenter is shown in a), while in b) the second lowest plane is shown as well.

To model the mixed Ni-C interactions as accurately as possible, a complete atomistic potential

for the Ni-C system was used, including Ni-Ni, C-C, and Ni-C interactions, with both attractive and

repulsive interactions.   This interatomic potential is a hybrid EAM[37]-Tersoff[38] Ni-C

interatomic potential with a DFT-based Lennard-Jones[39] term that includes an attractive

interaction. The Ni-Ni interactions were given by the EAM[37] potential developed by Mishin in 2004[40] and the C-C ones by the Tersoff potential[38]. The fitting procedure and final parameters for the Lennard-Jones mixed term are described in a recent publication[30]. This hybrid potential gave us a Ni lattice constant of 3.5201 Å at T = 1 K and of 3.5282 Å at T = 300 K. The C lattice constant was 3.5659 Å at T = 1 K and 3.5720 at T= 300 K.

For comparison, and to explore if the found interfacial structure is potential-dependent, we carried out additional MD indentation simulations using the same simulation cell, indenter and indentation speed, but a different atomistic potential. Specifically, we used the EAM potential developed by Ruda et al.[41] to describe both the Ni-Ni and the Ni-C interactions. In these simulations, the indenter was relaxed using the Tersoff potential[38] before initiating the actual nanoindentation, then frozen, so that no match between the Ni-C and the C-C bond strength in the atomistic potential was needed (as no C-C interactions are computed during the actual indentation). The two potentials we used are fairly different, as the Ruda potential[41] is a standard EAM potential while the potential from the present work[30] is a hybrid potential where the metal is described by an EAM form, the indenter is described by a functional form (Tersoff) designed to represent covalent bonding and the mixed term is given by a Lennard-Jones interaction. The Ruda potential was fitted on ab initio calculated NiC in the NaCl structure cohesive energy and mechanical properties, while the Ni-C interactions in the potential developed in the present work were not fitted to any NiC-in-the-NaCl-structure data. We fitted the present potential to DFT calculated Ni-C attraction between a single Ni atom on the (111) Ni surface and an atomically sharp tip of a diamond indenter about 3 Å above the specimen surface. No other fitting parameters were needed for the present potential, as the Ni-Ni and C-C were

already provided in the literature[30]. As a result of the differences between the two potentials,

physical quantities are predicted to have different values. With respect to NiC in the NaCl

structure, the Ruda potential predicts a lattice parameter for NiC of 0.3978 nm, a bulk modulus

of 284 GPa, and an enthalpy of formation of 0.14 eV/ atom, while the potential developed in the

present work predicts a lattice parameter of 0.347 nm, a bulk modulus of 301 GPa and an

enthalpy of formation of 2.10 eV/atom. Ab initio results for NiC in the NaCl structure [42] report

values of 0.401 nm for the lattice parameter, 304 GPa for the bulk modulus and 0.93 eV/atom

for the enthalpy of formation (Table 1).

Table 6-1: NaCl-NiC data for our potential, the Ruda one and ab-initio results taken from H. Amara et al., Phys Rev B 79, 014109 (2009)

NiC in NaCl structure	Lattice constant (Å)	Bulk Modulus (GPa)	Enthalpy of formation (eV/atom)
"our" potential	3.47	301	0.14
Ruta potential	3.978	284	2.10
DFT results	4.01	304	0.93

All of the DFT calculations described in this work were carried out using the DMol^3 code[43-45].

This code employs localized basis sets, and we used a real-space cutoff of 4 Å and a double-zeta-

polarized, atom-centered basis set (dnp). The exchange-correlation potential was treated within

the Perdew-Burke-Ernzerhof (PBE) generalized gradient approximation (GGA) approach[46]. The

ion core electrons of the Ni were described by a hardness conserving semi local pseudopotential

(dspp)[47]. The geometry optimization was performed using a conjugate gradient approach

based on a delocalized internal coordinate scheme[48, 49].

The simulation cell we used during the DFT investigation (Figure 6-3) contained 6 Ni (111) layers

and 1 C (100) layer. Each layer contained 4 atoms. Ni slabs with up to 10 layers for the (111)

orientation were used in independent, previous DFT simulations to determine the relaxed nickel

interplanar distances, and here we built our initial Ni configuration by taking the top 6 layers out

of those relaxed configurations. To preserve bulk information, the bottom two layers were kept

completely fixed. We also kept fixed the z coordinate of all the C atoms, and of the Ni atoms on

the Ni surface. This was done to keep a fixed distance between the C layer simulating the indenter

tip and the Ni surface. Periodic boundary conditions were applied in the x and y directions. For

both Ni and C we used 3.547 Å as lattice constant, which is the DMol^3 lattice constant for Ni using

PBE. Using the same lattice constant for both allowed to apply periodic boundary conditions to

the simulated system. The DMol^3 relaxed lattice constant for C using PBE is 3.572 Å, so we are

only compressing it by 0.7% to make it fit the Ni periodicity.
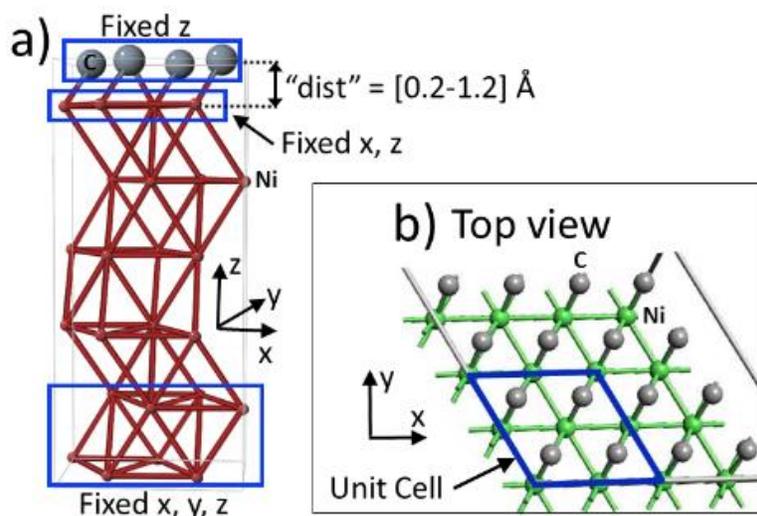
Figure 6-3 : DFT simulation cell: Side view (a) and top view (b). Carbon atoms are grey, Ni atoms red in a), green in b)

6.3 Atomic rearrangement at the interface: Ni-C monolayer structure

All the simulations we ran gave the exact same qualitative result: while no structural modification at the atomic level was seen in the indenter as a result of the nanoindentation process, a Ni-C interfacial structure always developed in the specimen. A structurally unchanged indenter agrees with previous MD findings[30], where more bond-breaking capable potentials such as ReaxFF were used, but are in disagreement with DFT results[29], suggesting that a correct treatment of the C-C interactions under strong compressive stress is, possibly, beyond MD capabilities with currently available potentials.

The use of an atomistic indenter allows the investigation of the Ni-C interface that forms as soon as the indenter comes into physical contact with the specimen. To determine the atomic structure of the Ni-C interface, we ran several sets of MD simulations, where we changed details such as the carving of the indenter tip, the orientation of the Ni sample, and the rotation of the indenter tip with respect to the atomic rows on the specimen. Several studies have shown that the relative orientation between the substrate and indenter can effect deformation during the indentation [10, 50-54]. In addition, we investigated the interface formation at two temperatures (T = 1 K and T = 300 K) and used other interatomic potentials[41]. In all cases, the same interfacial structure developed: a 1-layer thick co-penetration of Ni and C atoms in a square lattice (Figure 6-4). So rearranged, the average Ni-Ni distance is 2.60 ± 0.078 Å, C-C is 2.531 ± 0.008 Å, and Ni-C is 1.81 ± 0.011 at T=300K. The interfacial structure is remarkably similar to the {100} plane of a B1 crystal structure (NaCl prototype).
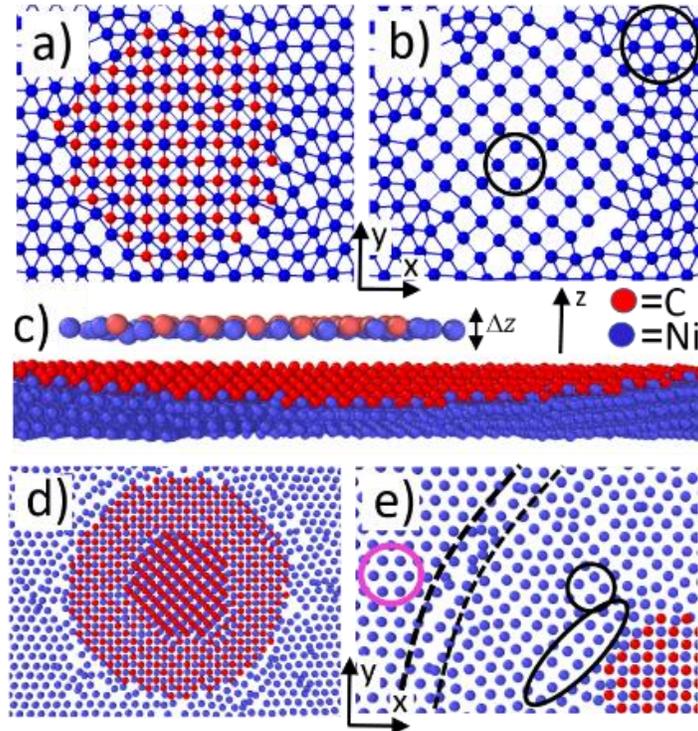
Figure 6-4: Contact between indenter and specimen leads to the formation of a square interfacial structure. Early contact in a) and b), contact when the indenter is several Angstrom into the specimen in c), d) and e). Both Ni and C atoms are shown in a), while only the Ni atoms are depicted in b), to better display the structural rearrangement (from hexagonal to square) that Ni atoms in Ni (111) surface have to undergo to form such an interfacial structure. In c) side views of the contact area between specimen and indenter are shown: monolayer where the intermixing occurs and, below it, a slice through the center of the indenter showing that the intermixing only occurs on a single layer. In d) another top view of the sample shows that the same structure is formed as the indenter is lowered further into the specimen. Finally, e) is taken at the same indentation depth as d), but only atoms in the atomic plane containing the very tip of the indenter are shown. Some Ni atoms directly below the indenter (inside the black circle and ellipse, for instance) have already changed their structural arrangement from hexagonal to squared, even if no C atom is intermixed with them yet.

Experimentally, NaCl-structure carbides of the 5d transition metals have been reported[55]. Moreover, while the phase diagram for the Ni-C system[42] shows a tendency of phase separation, i.e. a positive enthalpy of formation, the fact that the ordered phase Ni_3C can be produced by mechanical alloying [56, 57] indicates that the enthalpy of formation cannot be strongly positive. In a recent study [42], an enthalpy of formation of 0.93 eV/atom was calculated

for such a system using DFT calculations. This agrees well with values obtained from extrapolation of thermodynamic data [58-60]. This is an enthalpy of formation low enough that is reasonable to expect the formation this carbide under stressed conditions, as it is the case during nanoindentation. This also means that, as the enthalpies of formations of the two potentials we used are comparable to the ab-initio one, the intermixing that we are seeing can easily be interpreted in the light of carbide formation.

Forming such a structure at the interface during indentation of a Ni (100) surface requires very little atomic displacement, as a Ni (100) atomic plane is already arranged in a square lattice. However, the formation of this structure is quite remarkable for the case of Ni (111), as its creation requires transformation from a hexagonal arrangement to a square one (Figure 6-4 b)) on the Ni plane. In Figure 6-4 c side views of the contact area between specimen and indenter are shown to prove that the mixed interfacial structure is only 1 layer thick. The interfacial structure described above is formed in every simulation as soon as the C atoms come into direct contact with the Ni atoms, and, as the indenter digs deeper into the specimen, its location and size changes, but its structure never does (Figure 6-4 d). Finally, Figure 6-4 e) only shows atoms in the atomic plane containing the very tip of the indenter (thickness $\Delta z=1.8$ Å). This demonstrates how some Ni atoms directly below the indenter (inside the black circle and ellipse, for instance) have already changed their structural arrangement from hexagonal to square. It also shows how the maximum atomic disorder occurs at the boundary between the area already directly under the indenter tip and the rest of the atomic plane. Such a boundary region is marked by dashed black lines in the figure, just to guide the eyes.

Up to here we have discussed simulation results obtained in cases where the atomic rows in the indenter plateaus were parallel to the atomic rows in the specimen surface. In real indentation experiments, however, there is no control on the orientation of the atomic rows in either the specimen surface or the indenter tip. It is important, therefore, to simulate this more "random" case, and verify that the above identified interfacial structure is formed irrespectively of the misorientation between specimen and indenter. To this purpose we ran several simulations, at both temperatures, for misorientation angles up to 22°. We found that the intermixed, 1-layer thick, square structure always formed, irrespective of the misorientation between the atomic rows on the Ni surface and the indenter plateau. As an example, Figure 6-5 shows such a structure formed for a 22° misorientation at T = 1 K. The interfacial structure obtained when no misorientation is present is shown as well, as a comparison. Black lines are drawn to guide the eye through the atomic rows. While the formed interfacial structure is the same in both cases, its orientation changes, always following the orientation of the indenting diamond lattice. This means that forming such a structure is even more surprising for Ni (111) misoriented with respect to the indenter, as even larger displacements for the Ni atoms are necessary in such a case.
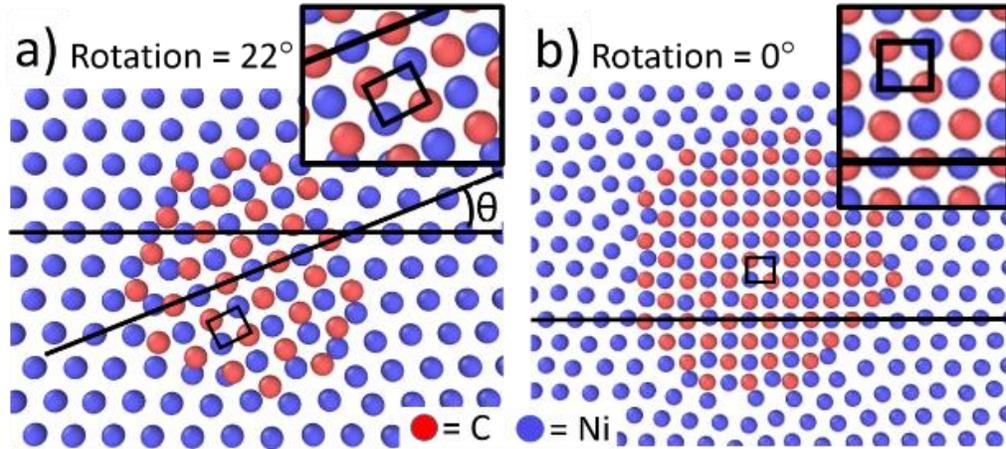
Figure 6-5: **Structure formed at the Ni-C interface when the atomic rows on the Ni (111) surface form an angle θ =22° and θ=0°(a) and b), respectively) with the atomic rows in the indenter tip. The simulation temperature was T = 1 K in both cases. Black lines and squares are drawn to guide the eye. The Ni-C interfacial structure is the same in both cases, but its orientation changes, always following the orientation of the indenting diamond lattice.**

Lastly, the same interfacial structure is also found when Ni adheres to the indenter as the indenter is slowly retracted from the specimen, as shown in **Error! Reference source not found.**.

Here, a "slow" indenter (speed = 0.01 Å/ps) has been lifted from a Ni (111) specimen after an 11.5 Å deep indentation at T = 1 K. A group of Ni atoms has adhered to the indenter during the process, forming a pyramidal "island", and has been completely removed from the Ni (111) specimen. Clearly, the same interface structure discussed above was formed during the indentation, and has been retained while the indenter was retracted. Details on this set of simulations, as well as a discussion of both the indenter and the specimen behavior during retraction are given in a previous publication[30].
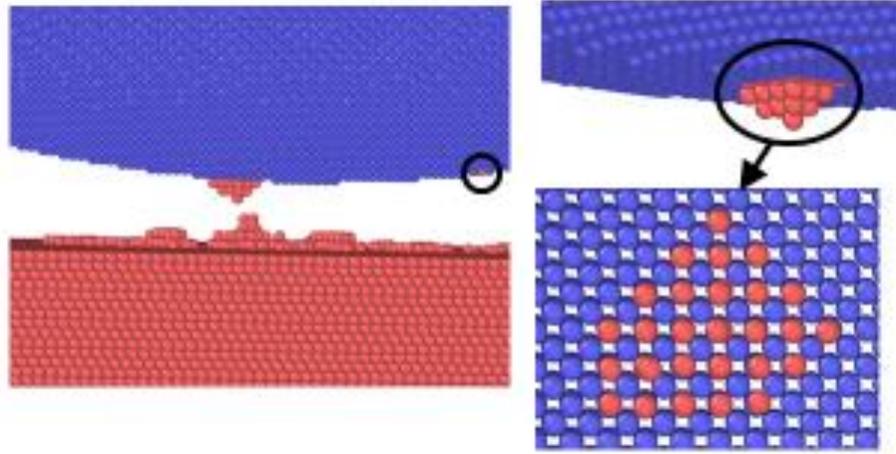
Figure 6-6: Blue atoms are C, red ones Ni. The Indenter has been retracted from the specimen, and, as a consequence of such a retraction, a small pyramidal clump of Ni has adhered to the indenter (a). The interfacial layer between the indenter surface and the Ni island shows the same, square interfacial structure as formed during the indentation (b)

To conclude the investigation of the Ni-C interface, results from orientations other than (111) should be discussed too. Figure 6-7 shows the interfacial structure formed at two indentation depths ((a) 0.92nm and (b) 1.52nm) when indenting Ni (100), and at indentation depths (c) 0 nm and (d) 0.7 nm when indenting Ni (110). All results were obtained at T=1 K, but (a) and (b) were simulated using the EAM potential developed by Ruda *et al.[41]* instead of the hybrid potential used in all the other results discussed in the paper to this point[30]. The first observation coming from Figure 6-7 is that the square interfacial structure is formed no matter the Ni orientation and the interatomic potential. The second, even more surprising point, is that the formation of the square, intermixed structure may cause significant structural disorder even for Ni surfaces with an atomic arrangement already similar to the final one. This can occur if the initial misalignment between the indenter atomic rows and the Ni ones is large enough, as shown in Figure 6-7 c) and d). Here we compare the atomic arrangement before the indentation starts

131

(Figure 6-7 c) and 0.7 nm into it (Figure 6-7 d). In d) the only atoms displayed are those in a plane of thickness Δz=1.4 Å that contains the C atoms in the very tip of the indenter. Red lines are drawn in the figure to guide the eye to the original atomic row direction in the Ni planes. A θ=10° misorientation is present between those lines and the ones formed by the C atoms. Figure 6-7 d) shows that the intermixed structure has formed following the atomic rows in the indenter, and that such an in-plane rotation of the Ni atom atomic rows has generated quite a structural disorder in the Ni plane. As extended atomic defects are a significant source of stress, understanding the details of the atomic reorganization that occurs during nanoindentation sheds light on the origin of stress points, and therefore on the subsequent dislocation nucleation. A large body of work on dislocation nucleation under the indenter shows that is can be effected by a variety of factors[22, 54, 61-76].
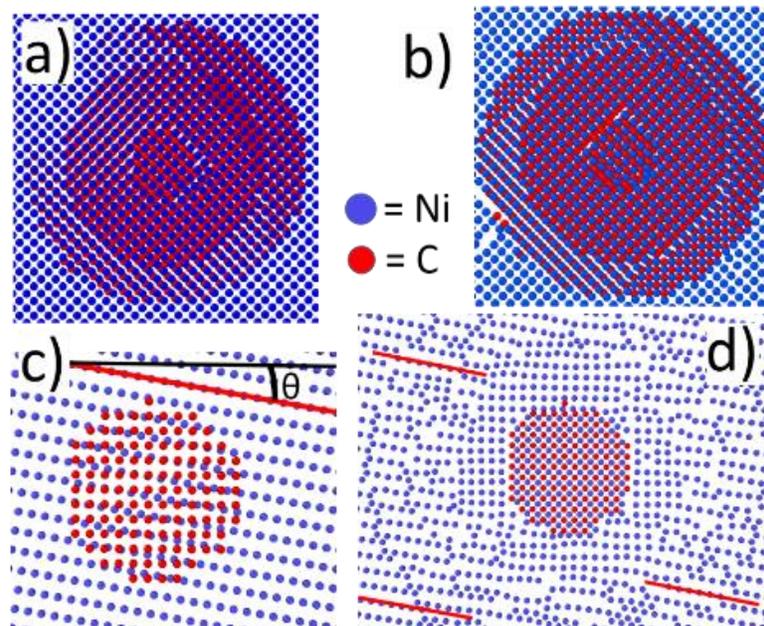
Figure 6-7: Snapshots of T=1K indentation simulations of Ni (100) at indentation depths 0.92nm (a) and 1.52nm (b), and of Ni (110) before indentation (c) and at indentation depth 0.7 nm (d). The Ruda atomistic potential was used in obtaining a) and b), while the hybrid one was used in the Ni (110) simulations.

6.4 DFT validation of structural rearrangement

In Section 3 we showed that the formation of a Ni-C interface may significantly modify the atomic arrangement on and near the Ni surface. Because lattice bonds are broken and reformed during such a process, we felt that the MD results should be validated by more accurate DFT calculations. In the following, we'll give a quick description of the DFT methodology we used, then discuss how the DFT findings compare to the classically-obtained Ni-C interfacial structure.

The first step in determining the reliability of our MD findings for the Ni-C interfacial structure is to address the lack of dimerization in the MD indenter tip. This is quite a large approximation, as it is well known that (100) C reconstructs into a (2x1) surface, with an unbuckled dimer geometry[77-79]. Such an approximation may very well affect the reconstruction at the interface, as the initial atomic positions are significantly different in the two cases (Figure 6-8). We addressed this issue in detail in a recent publication[29], where we simulated nanoindentation using a DFT semistatic approach. In that work, we lowered a (100) diamond tip into a Ni (111) or a Ni (100) specimen using a succession of 0.15 Å displacement steps. Our finding was that, in all cases, even in the presence of oxygen impurities on the Ni surface, the dimers opened up as the indenter approached the Ni. The specifics of the Ni surface only affected the distance at which the dimer opening occurred. We found that, in most cases, the opening happened before the two materials come in direct contact, and that it always happened at larger tip-Ni distances for Ni (100) surfaces than for Ni (111) ones.
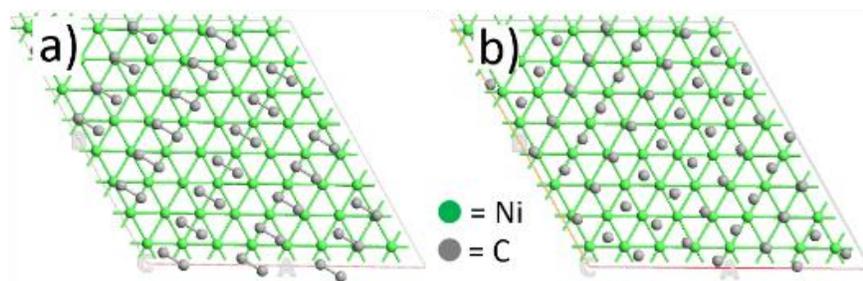
Figure 6-8: Difference in the initial structures, between having and not having dimer rows in the indenter tip. Top view of the indenter tip approaching the Ni (111) surface, as the tip is or is not in its (2x1) reconstruction (a) and b), respectively).

To investigate how the atomic arrangement on the Ni surface depends on the distance from the approaching indenter, we ran 6 simulations, each one for a different, fixed, distance between the C layer and the Ni surface. The largest investigated distance was 1.2 Å and the smallest was 0.2 Å. At each distance, we investigated the energetics of the transformation from an initial hexagonal Ni arrangement to an approximately square configuration. Having established that an initial configuration as in Figure 6-8 a) is a correct starting point for our investigation of the atomic arrangement at the Ni-C interface, we simulated the transformation from an hexagonal 2D lattice to a square one by rigidly displacing some Ni atoms on the Ni surface as shown in Figure 6-9. More specifically, every other row of Ni atoms on the (111) surface is moved along the $-x$ direction until the hexagonal configuration is transformed to a rectangular one. Ideally, we should obtain a square configuration, but the limitations of the DFT cell forced us to investigate a case similar, but not identical, to the ideal one, as in the DFT simulations the Ni-Ni distance along y in the final configuration is compressed by a factor of 1.155 with respect to the Ni-Ni distance along x (Figure 6-9). Lastly, as the Ni-Ni nn distance in the fcc lattice and the average Ni-Ni distance in the Ni-C rearranged configuration are very similar (2.56 ± 0.052 Å and 2.60 ± 0.078

Å, respectively, at T=300K – data from our MD simulations), it is a good approximation to keep

the cell size fixed during the transformation between the hexagonal Ni arrangement and the

rectangular one.
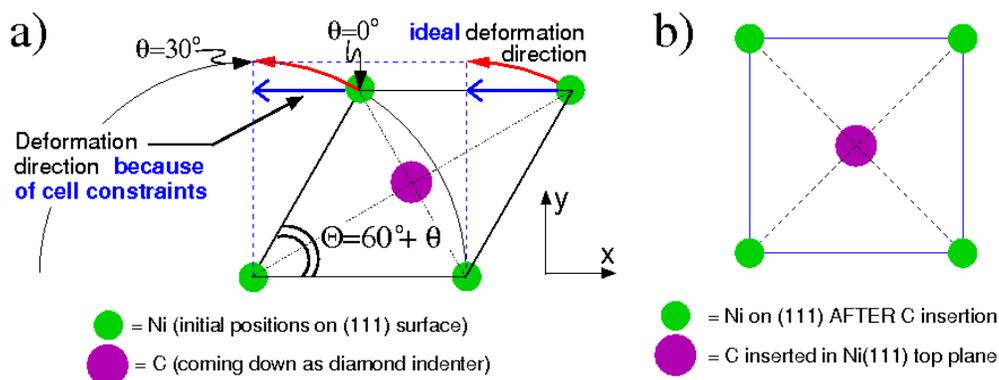
Figure 6-9: Top view of the (111) Ni surface. a) Initial positions and deformation direction, b) Final positions (schematic).The deformation angle Θ=60°+θ is shown in a), where θ ranges from 0° (hexagonal structure) to 30°(square structure).

Our results are shown in Figure 6-10, where the energy cost of the Ni surface deformation is

plotted versus the deformation angle for 6 fixed distances between the indenter tip and the Ni

surface. The atomic initial positions in the x, y plane are the same in all cases, and are shown in

Figure 6-10 (b). Before starting the deformation, all initial configurations are relaxed within the

constraints described in Section 5.1 (Figure 6-10 c). Intermediate structures are displayed in

Figure 6-10 (d) and (e), for the case where the tip is closest (distance tip-Ni surface=0.02 nm) or

furthest (distance tip-Ni surface=0.12 nm) from the Ni surface, respectively.
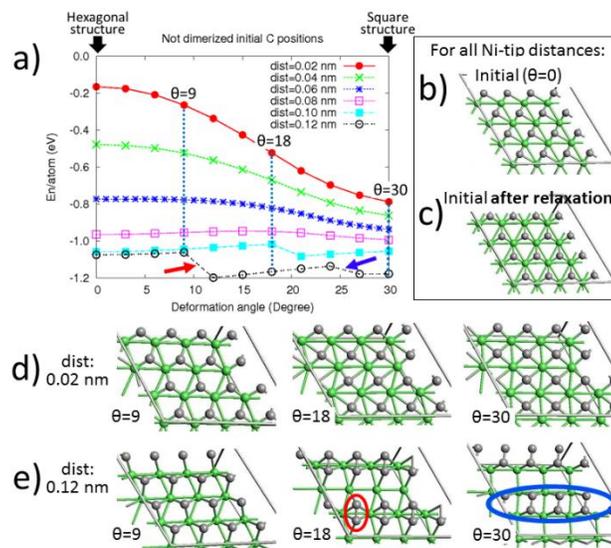
Figure 6-10: Energetics (a) and atomic positions (b-e) during the Ni surface deformation, as a function of the deformation angle.

As depicted in Figure 6-10 (a), DFT finds the "squared" Ni structure energetically advantageous with respect to the initial hexagonal one as long as the tip-Ni distance is shorter than 0.8 Å. Moreover, no energy barrier is found for such a surface deformation at such short distances. This means that the structural rearrangement for this 2D system will always occur as the tip approaches the specimen. For a real specimen, of course, the interaction with the underlying Ni layers must be considered. In addition, Figure 6-10 shows that the C atoms prefer the dimerized

configuration if the Ni specimen is sufficiently far away, and provides us with a way to estimate what "far" is. Observing the formation of dimers validates our modeling strategy, as a dimerized configuration is the ground state structure for isolated C (100) surfaces. The dimers have re-formed in Figure 6-10 (e) between θ=18° and θ=30°, and Figure 6-10 (a) displays an abrupt decrease in configurational energy in the same θ interval. A similar, but slightly smaller energy

jump is present in the case of tip-Ni distance equal to 1 Å as well, indicating a similar behavior. However, for a tip-Ni distance of 0.8 Å the deformation is characterized only by the presence of a very small energy barrier, therefore demarking the distances for which the Ni surface is structurally affected by the presence of the indenter from those for which the Ni specimen is not.

Lastly, to further validate the finding of the Ni-C intermixed squared structure, we performed several semistatic nanoindentations using DFT, utilizing a Ni (111) specimen and an atomically flat indenter, with two dimers (4 atoms) in the tip. This approach eliminates the need to constrain the DFT cell as was necessary when investigating the deformation directly, however, as only 4 C atoms are present, only "precursors" of the rearrangement could be expected. The simulation methodology and detailed discussion of these simulation results is given in a previous publication[29]. Here we only want to focus on findings related to the Ni-C rearrangement at the surface, i.e. the opening of the C dimers and the deviation from the hexagonal structure in the case of the Ni surface. We found that the opening of the dimers occurred in all examined cases, including those where the Ni surface was contaminated by oxygen atoms. We also observed the early stages of transformation from hexagonal to squared structure, as much as it is reasonable to expect having an extremely limited simulation box and only 2 dimers acting on the Ni surface. Figure 6-11 shows a typical example of our findings. Panel a) shows the simulation cell when the indenter tip is still about 2 Å away from the specimen, while b) displays the configuration obtained when the tip of the indenter is about 0.6 Å above the Ni surface. For clarity, only the C atoms in the indenter tip and the Ni atoms on the surface are shown in the top views. Ellipses guide the eye to the dimers (before and after they open up), while a dashed square points out the region where the early stages of the squared, intermingled structure can be observed.
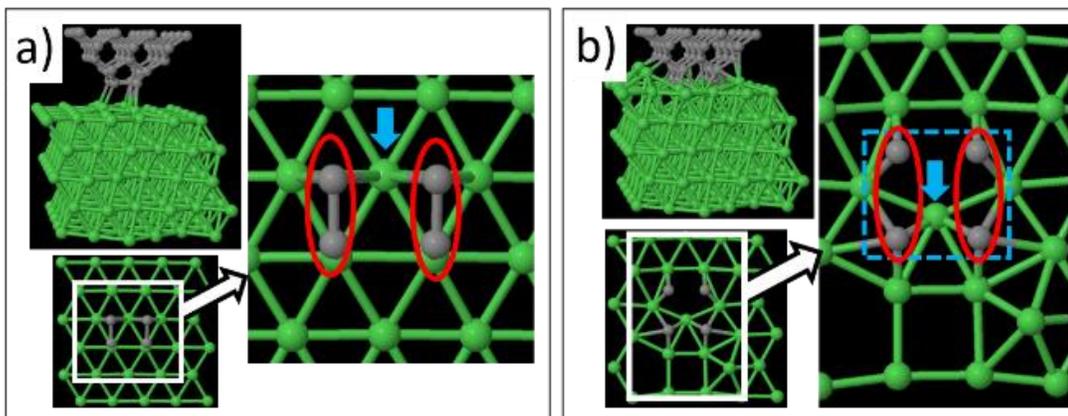
Figure 6-11: Semistatic DFT simulation of early stages of nanoindentation. Atomic snapshots as the indenter tip is 2 Å (a), and 0.6 Å (b) above the Ni (111) surface. In (b) both dimers have opened up (red ellipses guide the eye to the C atoms forming the dimers, before and after the opening). A blue arrow points to the C atom that in a) is in-between the two dimers, in b) is almost at the center of the square that is formed by the C atoms that used to be dimerized. A dashed blue square points out such an area. C atoms are gray, Ni atoms are green.

In conclusion, all of the DFT findings agree with the MD results for the atomic structure of the Ni-C contact layer. This demonstrates that the structural transformation to a square Ni lattice is the lowest energy way to arrange the Ni-C interface under compressive stress and that such an atomic rearrangement can probably be obtained using any classical force field that would properly model both attractive and repulsive Ni-C, C-C and Ni-Ni interactions.

6.5 Conclusions

Using MD with a custom-designed Ni-C potential and validating DFT simulations, we explored the atomic interactions between a (100)-oriented diamond nanoindenter and a single crystal Ni specimen during the early contact phase. As the indenter tip approaches to within approximately 0.8 Å of the Ni surface, the carbon dimers open up, even in the presence of oxygen on the sample surface. The specific distance depends upon the orientation of the Ni surface. Next, the

interaction between the impinging carbon atoms and top Ni layer causes the positions of the Ni atoms to shift into a square lattice commensurate with the C atom positions, producing a one-atom-thick square lattice array of C and Ni atoms. Remarkably, this same Ni-C configuration develops for all of the orientations of the Ni sample that were explored, including (111), (100), (110), and numerous rotations where the planes of nickel atoms are rotated with respect those in the diamond lattice. In retraction simulations, Ni atoms remaining on the indenter tip retain the square Ni-C structure after removal from the Ni specimen. Also, indentation simulations were conducted at two temperatures, 1 K and 300 K, and the same Ni-C structure formed in all cases. Finally, the same structure was also found using different interatomic potentials to describe Ni-Ni and Ni-C interactions. The interfacial structure is similar to the {100} plane of a B1 crystal structure (NaCl prototype). The stability of this interfacial structure was confirmed by DFT studies that found the formation of this interface structures energetically favorable.

In addition to developing a unique, persistent and highly ordered atomic configuration directly under the indenter tip, the Ni-C interaction was observed to produce extended disorder of the Ni surface atoms away from the direct-contact region. This irregular surface structure is indicative of highly localized strain, and therefore highly localized local stresses, that can affect the dislocation nucleation process and contribute to the enhanced dislocation nucleation that has been reported from atomic ledges[28]. In other words, the present results indicate a strong preference for a structured interface, and therefore suggests that the onset of plasticity could occur at the interface instead of beneath it, as predicted by continuum models and MD simulations without atomistic indenters.

Acknowledgments

References

1. Ma, L., et al., *The role of probe shape on the initiation of metal plasticity in nanoindentation.* Acta Materialia, 2012. **60**(12): p. 4729-4739.
2. Basire, C. and C. Fretigny, *Determination of viscoelastic moduli at a submicrometric scale.* European Physical Journal-Applied Physics, 1999. **6**(3): p. 323-329.
3. Campbellová, A., et al., *Small-load nanoindentation experiments on metals.* Surface and Interface Analysis, 2010. **42**(6-7): p. 766-769.
4. Cuenot, S., S. Demoustier-Champagne, and B. Nysten, *Elastic modulus of polypyrrole nanotubes.* Physical Review Letters, 2000. **85**(8): p. 1690-1693.
5. Salvetat, J.P., et al., *Elastic and shear moduli of single-walled carbon nanotube ropes.* Physical Review Letters, 1999. **82**(5): p. 944-947.
6. Tangyunyong, P., et al., *Nanometer-scale mechanics of gold films.* Physical review letters, 1993. **71**(20): p. 3319.
7. Tomasetti, E., R. Legras, and B. Nysten, *Quantitative approach towards the measurement of polypropylene/(ethylene-propylene) copolymer blends surface elastic properties by AFM.* Nanotechnology, 1998. **9**(4): p. 305-315.
8. Baitsch, M., K.C. Le, and T.M. Tran, *Dislocation structure during microindentation.* International Journal of Engineering Science, 2015. **94**: p. 195-211.
9. Buchwald, J. and S.G. Mayr, *Influence of surface stresses on indentation response.* Nanotechnology, 2015. **26**(12).
10. Li, J., et al., *Atomistic mechanisms governing elastic limit and incipient plasticity in crystals.* Nature, 2002. **418**(6895): p. 307-310.
11. Liu, M. and H. Proudhon, *Finite element analysis of frictionless contact between a sinusoidal asperity and a rigid plane: Elastic and initially plastic deformations.* Mechanics of Materials, 2014. **77**: p. 125-141.
12. Kruggel-Emden, H., et al., *Review and extension of normal force models for the Discrete Element Method.* Powder Technology, 2007. **171**(3): p. 157-173.
13. Gao, Y., et al., *Comparative simulation study of the structure of the plastic zone produced by nanoindentation.* Journal of the Mechanics and Physics of Solids, 2015. **75**: p. 58-75.
14. Gao, Y., C.J. Ruestes, and H.M. Urbassek, *Nanoindentation and nanoscratching of iron: Atomistic simulation of dislocation generation and reactions.* Computational Materials Science, 2014. **90**: p. 232-240.
15. Li, J., A.H.W. Ngan, and P. Gumbsch, *Atomistic modeling of mechanical behavior.* Acta Materialia, 2003. **51**(19): p. 5711-5742.
16. Sinnott, S.B., et al., *Computer Simulations of Nanometer-Scale Indentation and Friction*. Nanotribology and Nanomechanics: Measurement Techniques and Nanomechanics, Vol 1, ed. B. Bhushan. 2011. 439-525.
17. Gouldstone, A., et al., *Indentation across size scales and disciplines: Recent developments in experimentation and modeling.* Acta Materialia, 2007. **55**(12): p. 4015-4039.

18.   Imran, M., et al., *Mechanical behavior of Cu-Zr bulk metallic glasses (BMGs): A molecular dynamics approach.* Chinese Physics B, 2013. **22**(9).
19.   Kelchner, C.L., S.J. Plimpton, and J.C. Hamilton, *Dislocation nucleation and defect structure during surface indentation.* Physical Review B, 1998. **58**(17): p. 11085-11088.
20.   Nair, A.K., et al., *Size effects in indentation response of thin films at the nanoscale: A molecular dynamics study.* International Journal of Plasticity, 2008. **24**(11): p. 2016-2031.
21.   Qiu, C., et al., *Study of nanoindentation behavior of amorphous alloy using molecular dynamics.* Applied Surface Science, 2014. **305**: p. 101-110.
22.   Ruestes, C.J., et al., *Atomistic simulation of tantalum nanoindentation: Effects of indenter diameter, penetration velocity, and interatomic potentials on defect mechanisms and evolution.* Materials Science and Engineering a-Structural Materials Properties Microstructure and Processing, 2014. **613**: p. 390-403.
23.   Zhu, P. and F. Fang, *Molecular dynamics simulations of nanoindentation of monocrystalline germanium.* Applied Physics A, 2012. **108**(2): p. 415-421.
24.   Goel, S., et al., *Molecular dynamics simulation of nanoindentation of Fe3C and Fe4C.* Materials Science and Engineering a-Structural Materials Properties Microstructure and Processing, 2014. **597**: p. 331-341.
25.   Solhjoo, S. and A.I. Vakis, *Single asperity nanocontacts: Comparison between molecular dynamics simulations and continuum mechanics models.* Computational Materials Science, 2015. **99**: p. 209-220.
26.   Sushko, G., et al. *Molecular dynamics simulation of nanoindentation of nickel-titanium crystal*. in *Journal of Physics: Conference Series*. 2013. IOP Publishing.
27.   Verkhovtsev, A.V., et al., *Molecular dynamics simulations of the nanoindentation process of titanium crystal.* Computational Materials Science, 2013. **76**: p. 20-26.
28.   Wagner, R.J., et al., *Dislocation nucleation during nanoindentation of aluminum.* Journal of Applied Physics, 2008. **104**(11).
29.   Tavazza, F. and L.E. Levine, *DFT Investigation of Early Stages Of Nanoindentation in Ni.* The Journal of Physical Chemistry C, 2016. **DOI 10.1021/acs.jpcc.6b01148**.
30.   Tavazza, F., et al., *Molecular Dynamics Investigation of the Effects of Tip-Substrate Interactions during Nanoindentation.* Journal of Physical Chemistry C, 2015. **119**(24): p. 13580-13589.
31.   Chang, H.J., et al., *Multiscale modelling of indentation in FCC metals: From atomic to continuum.* Comptes Rendus Physique, 2010. **11**(3-4): p. 285-292.
32.   Gouldstone, A., et al., *Discrete and continuous deformation during nanoindentation of thin films.* Acta Materialia, 2000. **48**(9): p. 2277-2295.
33.   Shao, Y.F., et al., *Multiscale simulations on the reversible plasticity of Al (0 0 1) surface under a nano-sized indenter.* Computational Materials Science, 2013. **67**: p. 346-352.
34.   Xu, S., et al., *A quasistatic implementation of the concurrent atomistic-continuum method for FCC crystals.* International Journal of Plasticity, 2015. **72**: p. 91-126.
35.   Plimpton, S., *Fast parallel algorithms for short-range molecular dynamics.* Journal of computational physics, 1995. **117**(1): p. 1-19.
36.   Nosé, S., *A unified formulation of the constant temperature molecular dynamics methods.* The Journal of chemical physics, 1984. **81**(1): p. 511-519.
37.   Daw, M.S. and M.I. Baskes, *Embedded-atom method: Derivation and application to impurities, surfaces, and other defects in metals.* Physical Review B, 1984. **29**(12): p. 6443.
38.   Tersoff, J., *Modeling solid-state chemistry: Interatomic potentials for multicomponent systems.* Physical Review B, 1989. **39**(8): p. 5566.

39.   Jones, J.E. *On the determination of molecular fields. I. From the variation of the viscosity of a gas with temperature*. in *Proceedings of the Royal Society of London A: Mathematical, Physical and Engineering Sciences*. 1924. The Royal Society.

40.   Mishin, Y., *Atomistic modeling of the γ and γ'-phases of the Ni–Al system.* Acta Materialia, 2004. **52**(6): p. 1451-1467.

41.   Ruda, M., D. Farkas, and J. Abriata, *Interatomic potentials for carbon interstitials in metals and intermetallics.* Scripta materialia, 2002. **46**(5): p. 349-355.

42.   Amara, H., et al., *Tight-binding potential for atomistic simulations of carbon interacting with transition metals: Application to the Ni-C system.* Physical Review B, 2009. **79**(1).

43.   Delley, B., *An all-electron numerical method for solving the local density functional for polyatomic molecules.* The Journal of chemical physics, 1990. **92**(1): p. 508-517.

44.   Delley, B., *From molecules to solids with the DMol3 approach.* The Journal of chemical physics, 2000. **113**(18): p. 7756-7764.

45.   Pan, Z. and T.J. Rupert, *Damage nucleation from repeated dislocation absorption at a grain boundary.* Computational Materials Science, 2014. **93**: p. 206-209.

46.   Perdew, J.P., K. Burke, and M. Ernzerhof, *Generalized gradient approximation made simple.* Physical review letters, 1996. **77**(18): p. 3865.

47.   Delley, B., *Hardness conserving semilocal pseudopotentials.* Physical Review B, 2002. **66**(15): p. 155125.

48.   Baker, J., A. Kessi, and B. Delley, *The generation and use of delocalized internal coordinates in geometry optimization.* The Journal of chemical physics, 1996. **105**(1): p. 192-212.

49.   Pulay, P. and G. Fogarasi, *Geometry optimization in redundant internal coordinates.* The Journal of chemical physics, 1992. **96**(4): p. 2856-2860.

50.   Hu, T.Y., et al., *Molecular dynamics simulation of incipient plasticity of nickel substrates of different surface orientations during nanoindentation.* Materials Science and Technology, 2015. **31**(3): p. 325-331.

51.   Ju, S.P., et al., *The nanoindentation responses of nickel surfaces with different crystal orientations.* Molecular Simulation, 2007. **33**(11): p. 905-917.

52.   Kum, O., *Orientation effects in shocked nickel single crystals via molecular dynamics.* Journal of applied physics, 2003. **93**: p. 3239-3247.

53.   Liang, Y.C., et al., *Study of Dislocation Nucleation Mechanism in Nanoindentation Process.* Nanoscience and Nanotechnology Letters, 2013. **5**(5): p. 536-541.

54.   Ziegenhain, G., A. Hartmaier, and H.M. Urbassek, *Pair vs many-body potentials: Influence on elastic and plastic behavior in nanoindentation of fcc metals.* Journal of the Mechanics and Physics of Solids, 2009. **57**(9): p. 1514-1526.

55.   Wiltner, A. and C. Linsmeier, *Formation of endothermic carbides on iron and nickel.* Physica Status Solidi a-Applied Research, 2004. **201**(5): p. 881-887.

56.   Yue, L.P., et al., *Magnetic properties of disordered Ni3C.* Physical Review B, 2000. **62**(13): p. 8969-8975.

57.   Banhart, F., J.C. Charlier, and P.M. Ajayan, *Dynamic behavior of nickel atoms in graphitic networks.* Physical Review Letters, 2000. **84**(4): p. 686-689.

58.   Cottrell, A.H., *Chemical bonding in transition metal carbides*. 1995: Institute of Materials.

59.   Haglund, J., et al., *Band-Structure and Cohesive Properties of 3d-Transition-Metal Carbides and Nitrides with the Nacl-Type Structure.* Physical Review B, 1991. **43**(18): p. 14400-14408.

60.   Guillermet, A.F., J. Haglund, and G. Grimvall, *Cohesive Properties of 4d-Transition-Metal Carbides and Nitrides in the Nacl-Type Structure.* Physical Review B, 1992. **45**(20): p. 11557-11567.

61.   Chen, I.H., et al., *Defect formation by pristine indenter at the initial stage of nanoindentation.* Journal of Applied Physics, 2013. **114**(21).

62.   Lee, Y.M., et al., *Atomistic simulations of incipient plasticity under A1(111) nanoindentation.* Mechanics of Materials, 2005. **37**(10): p. 1035-1048.

63.   Liang, H.Y., et al., *Crystalline plasticity on copper (001), (110), and (111) surfaces during nanoindentation.* Cmes-Computer Modeling in Engineering & Sciences, 2004. **6**(1): p. 105-114.

64.   Lilleodden, E.T., et al., *Atomistic simulations of elastic deformation and dislocation nucleation during nanoindentation.* Journal of the Mechanics and Physics of Solids, 2003. **51**(5): p. 901-920.

65.   Minor, A.M., et al., *A new view of the onset of plasticity during the nanoindentation of aluminium.* Nature Materials, 2006. **5**(9): p. 697-702.

66.   Njeim, E.K. and D.F. Bahr, *Atomistic simulations of nanoindentation in the presence of vacancies.* Scripta Materialia, 2010. **62**(8): p. 598-601.

67.   Remington, T.P., et al., *Plastic deformation in nanoindentation of tantalum: A new mechanism for prismatic loop formation.* Acta Materialia, 2014. **78**: p. 378-393.

68.   Salehinia, I. and S.N. Medyanik, *Effects of Vacancies on the Onset of Plasticity in Metals-An Atomistic Simulation Study.* Metallurgical and Materials Transactions a-Physical Metallurgy and Materials Science, 2011. **42A**(13): p. 3868-3874.

69.   Salehinia, I., V. Perez, and D.F. Bahr, *Effect of vacancies on incipient plasticity during contact loading.* Philosophical Magazine, 2012. **92**(5): p. 550-570.

70.   Shin, C., Y.N. Osetsky, and R.E. Stoller, *Dislocation nucleation and defect formation in copper by stepped spherical indenter.* Philosophical Magazine, 2012. **92**(25-27): p. 3158-3171.

71.   Tsuru, T. and Y. Shibutani, *Anisotropic effects in elastic and incipient plastic deformation under (001), (110), and (111) nanoindentation of Al and Cu.* Physical Review B, 2007. **75**(3).

72.   Tucker, G.J. and S.M. Foiles, *Molecular dynamics simulations of rate-dependent grain growth during the surface indentation of nanocrystalline nickel.* Materials Science and Engineering a-Structural Materials Properties Microstructure and Processing, 2013. **571**: p. 207-214.

73.   Ukwatta, A. and A. Achuthan, *A molecular dynamics (MD) simulation study to investigate the role of existing dislocations on the incipient plasticity under nanoindentation.* Computational Materials Science, 2014. **91**: p. 329-338.

74.   Yaghoobi, M. and G.Z. Voyiadjis, *Effect of boundary conditions on the MD simulation of nanoindentation.* Computational Materials Science, 2014. **95**: p. 626-636.

75.   Zhang, J.J., et al., *Atomistic simulation of the influence of nanomachining-induced deformation on subsequent nanoindentation.* Computational Materials Science, 2012. **59**: p. 14-21.

76.   Zimmerman, J.A., et al., *Surface step effects on nanoindentation.* Physical Review Letters, 2001. **87**(16): p. art. no.-165507.

77.   Jones, P.M., et al., *Atomistic Frictional Properties of the C (100) 2x1-H Surface.* Advances in Tribology, 2013. **2013**.

78.   Kang, H.C., *Structure of dimers at the C(100), Si(100) and Ge(100) surfaces.* Surface and Interface Analysis, 1999. **28**(1): p. 92-96.

79.   Yang, C. and H.C. Kang, *Cluster study of the dimer geometry on the C (100) surface.* Surface science, 1998. **409**(3): p. 521-527.

80.   Stukowski, A., *Visualization and analysis of atomistic simulation data with OVITO-the Open Visualization Tool.* Modelling and Simulation in Materials Science and Engineering, 2010. **18**(1).

CHAPTER 7: AN ELASTIC PLASTIC CONTACT MODEL WITH STRAIN HARDENING FOR THE LAMMPS GRANULAR PACKAGE

Bryan R Kuhr, Mathew R Brake, Jeremy B Lechman

Sandia National Laboratories, P.O. Box 5800, Albuquerque, New Mexico

Abstract

The following details the implementation of an analytical elastic plastic contact model with strain hardening for normal impacts conceived by Mathew Brake into the LAMMPS granular package. The model assumes that, upon impact, the collision has a period of elastic loading followed by a period of mixed elastic plastic loading, with contributions to each mechanism estimated by a hyperbolic secant weight function. This function was successfully implemented in the LAMMPS source code as the pair style gran/ep/history. Preliminary tests, simulating the pouring of pure nickel spheres, showed the elastic/plastic model took 1.66x as long as similar runs using gran/hertz/history.

Comments

This manuscript is a peer review openly accessible government report prepared for Sandia National Laboratories [1]. It has been lightly edited for formatting.

1.   Kuhr, B., M.R.W. Brake, and J.B. Lechman, *An Elastic Plastic Contact Model with Strain Hardening for the LAMMPS Granular Package.* 2015.

7.1 Introduction

This report describes the implementation of a new elastic-plastic contact model for spheres that can exhibit strain-hardening into the LAMMPS (Large-scale Atomistic/Molecular Massively Parallel Simulator) granular package. What follows is a brief description of the relevant portions of the LAMMPS granular package and the elastic-plastic contact model. For more detailed information, see the LAMMPS documentation and reference [1].

7.1.1 LAMMPS Granular Package

LAMMPS includes a "granular" package for the simulation of macro-scale spherical particles. This package accounts for the diameter and mass of each particle in addition to their angular and linear velocities when solving Newton's equations of motion in a given simulation domain. Accordingly, the particle-particle interactions can be based oncontinuum models for contact mechanics and frictional effects. The current LAMMPS distribution includes three granular pair styles: gran/hooke, gran/hooke/history and gran/hertz history. These pair styles model the normal elastic contact force between two particles as either linearly proportional to the overlap distance (the Hookean model) or via a nonlinear spring (the Hertz contact model). The tangential force is calculated via a columbic friction model with the option of tangential elastic contact. Each pair style allows for velocity damping, wherein a viscoelastic damping constant is specified for normal and tangential contact. The overall force acting on the point of contact between two particles is thus

$$F = F_{n(elas)} + F_{n(damp)} + F_{t(fric)} + F_{t(damp)} \tag{1}$$

This force calculation will be detailed for the gran/hertz/history pair style as that is the basis for the current work.

1.1.1 Hertzian Contact

The gran/hertz/history pair style models the normal contact force of any two particles via

$$F_{n(elas)} = \sqrt{\delta}\sqrt{\frac{R_iR_j}{R_i+R_j}}\left(k_n\delta\mathbf{n}_{ij}\right) = \frac{4}{3}E\sqrt{r_{eff}}\delta^{3/2}\mathbf{n}_{ij} \tag{2}$$

Where δ is the overlap distance between two particles, R_i and R_j are the non-deformed radii of the particles, k_n is the elastic constant specified by the user and n_{ij} is the unit vector between the particle centers. Some may be more familiar with the expression on the right side of the equation where E is the elastic modulus, and r_{eff} is the effective radius of the particle pair,

$$r_{eff} = \frac{R_iR_j}{R_i+R_j} \tag{3}$$

1.1.2 Frictional Forces.

Friction is calculated in gran/hertz/history using a piecewise definition:

$$F_{t(fric)} = \begin{cases} -\sqrt{\delta r_{eff}}k_t\Delta s_t & \sqrt{\delta r_{eff}}|k_t\Delta s_t| < \mu\|F_n\| \\ -\mu\|F_n\|\hat{v}_t & \sqrt{\delta r_{eff}}|k_t\Delta s_t| \geq \mu\|F_n\| \end{cases} \tag{4}$$

with elastic constant k_t, tangential displacement vector between particles Δs_t, friction coefficient μ, and tangential component of the particles' relative velocity vt. Of these properties, k_t and μ are specified by the user. This is one of two ways that energy is dissipated in these simulations.

1.1.3 Velocity Damping

A second method that can dissipate energy in the system is via the inclusion of viscoelastic damping. This is handled in LAMMPS by additional terms in the calculation of normal and tangential velocity with normal damping coefficient γ_n and tangential damping coefficient γ_t

$$F_{n(damp)} = -\sqrt{\delta r_{eff}}m_{eff}\gamma_n\mathbf{v}_n \tag{5}$$

$$F_{t(damp)} = -\sqrt{\delta r_{eff}}m_{eff}\gamma_t\mathbf{v}_t \tag{6}$$

The effective mass of the two particles is based on the mass of each of the particles (m_i and m_j):

$$m = \frac{m_im_j}{m_i+m_j} \tag{7}$$

Figure 7-1 shows the effects of various damping parameters on the normal contact force of two particles colliding "head-on".
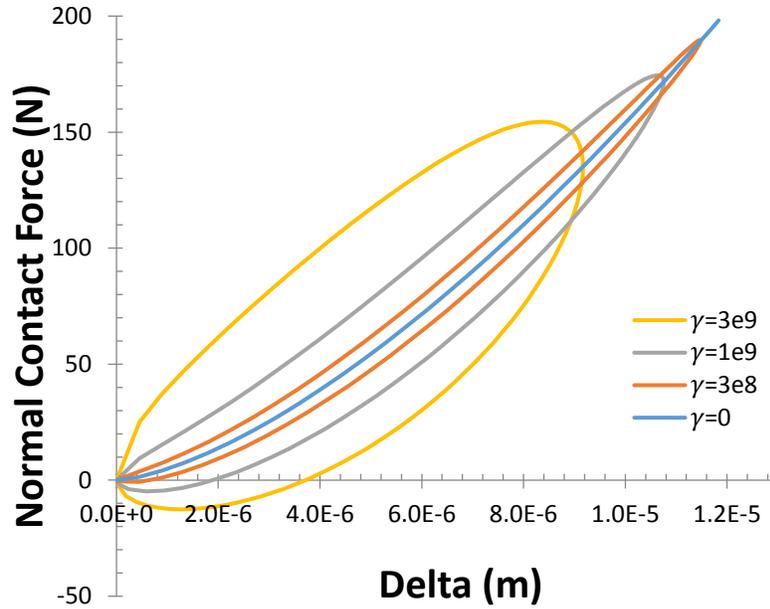
Figure 7-1: Effects of various damping coefficients (m⁻¹s⁻¹) on a simulated Ni-WC collision (Courtesy Sandia National Laboratories)

Table 7-1: gran/hertz/history inputs

Input:	k_n	k_t	γ_n	γ_t	μ	Dampflag
Description:	Normal elastic constant	Tangential elastic constant	Normal damping parameter	Tangential damping parameter	Coulombic friction coefficient	Include or exclude $F_{t(damp)}$
SI Units:	Pa	Pa	1/m/s	1/m/s	None	None
Relevant Equation:	(2)	(4)	(5)	(6)	(4)	(1)

This can be a useful representation of soft, viscous materials, but is phenomenologically incorrect for

harder materials, such as metals, that deform plastically upon such impacts.

1.1.4 Input Sytax

LAMPPS requires the inputs detailed in table 6-1 to use gran/hertz/history. The following command

calls the pair style gran/hertz/history

pair_style gran/hertz/history Kn Kt gamma_n gamma_t xmu dampflag

147

7.1.2 Elastic-Plastic Contact Model

A new model for contact force between spherical particles that accounts for plastic deformation and strain hardening is developed in [1]. This model poses that, like tensile behavior, as contact between two particles is initiated it enters a period of recoverable elastic deformation, followed by a period of mixed elastic/plastic deformation. The following is a brief summary of the relationships derived in that model

1.2.1 The elastic regime

It is accepted that the load reaction follows the Hertzian relationship described in eq. 2 from the initiation of contact until the onset of yield ($0 < \delta \leq \delta_y$). defined

$$\delta_y = \frac{r_{eff}}{A(v)} \left(\frac{\pi \sigma_y}{2E}\right)^2 \tag{8}$$

from [2] where $A(v)$ is the maximum amplitude of the stress field in the more compliant material during contact as function of its Poisson ratio (v), defined by:

$$A(v) = \max_{z/a \geq 0} \left(-(1 + v)\left(1 - \frac{z}{a}\tan^{-1}\left(\frac{a}{z}\right)\right) + \frac{3}{2}\frac{1}{1+(z/a)^2}\right)^2 \tag{9}$$

where z/a is the ratio of the depth below the contact point to the radius of the contact area.

1.2.2 The Mixed Elastic-Plastic Regime

After the onset of yield, the model hypothesizes that deformation has both elastic and plastic contributions, with the elastic contribution decaying as the plastic contribution increases. The normal force on the point of contact then becomes:

$$F_n = \phi_1(\delta)F_{n(elas)} + \phi_2(\delta)F_{n(plas)} \tag{10}$$

with transitionary functions ϕ_1 and ϕ_2 that determine that determine the contribution of each deformation mechanism. If a uniform pressure distribution during plastic flow is assumed, the contact force is:

$$F_{n(plas)} = p_0\pi \frac{a^n}{a_p^{n-2}}\mathbf{n}_{ij} \tag{11}$$

148

where the exponent n is the Meyer Hardness, a is the instantaneous contact area radius, p_0 and a_p are the contact pressure and contact area radius at which fully developed plastic flow occurs. Given the relationship

$$a^2 = \left(1 + \phi_2(\delta)\right)r_{eff}\delta \tag{12}$$

then

$$a_p^2 = 2r_{eff}\delta_p \tag{13}$$

Without strain hardening, p_0 can be calculated given the Brinnel Hardness (H) via:

$$p_o = Hg10^6 \tag{14}$$

Here, The acceleration due to gravity g is needed for unit conversion from the units of Brinell Hardness (kgf/mm^2) to Pa. In [1], ϕ_1 and ϕ_2 are derived to be

$$\phi_1(\delta) = \begin{cases} \text{sech}\left((1+\xi)\frac{\delta-\delta_y}{\delta_p-\delta_y}\right) & \delta > \delta_y \\ 1 & \delta \le \delta_y \end{cases} \tag{15}$$

$$\phi_2(\delta) = \begin{cases} 1 - \text{sech}\left((1-\xi)\frac{\delta-\delta_y}{\delta_p-\delta_y}\right) & \delta > \delta_y \\ 0 & \delta \le \delta_y \end{cases} \tag{16}$$

These functions are scaled by ξ, an empirical constant that is shown to agree well with the data given ξ = *n − 2.* And are dependent on δ$_p$ which is derived along with ϕ_1 and ϕ_2

$$\delta_p = \left(\frac{3\pi p_0}{2E}\right)^2 r_{eff} \tag{17}$$

1.2.3 The Restitution Phase
This model accepts the well-established rule that unloading is an elastic process, with no reverse yielding. The normal force during restitution follows

$$F_{n(rest)} = \begin{cases} \frac{4}{3}E\sqrt{\bar{r}_{eff}}(\delta - \bar{\delta})^{3/2} & \partial > \bar{\partial} \\ 0 & \partial \le \bar{\partial} \end{cases} \tag{18}$$

where $\bar{r}_{eff}$ and $\bar{\delta}$ are the deformed radius of curvature and residual deformation, respectively, that result from contact. These values can be obtained by continuity and are given as

$$\bar{\delta} = \delta_m \left(1 - \frac{F_m}{4/3E\sqrt{r_{eff}}\delta_m^{3/2}} \right) \qquad (19)$$

$$\bar{r}_{eff} = \frac{F_m^2}{(4/3E)^2(\delta_m - \bar{\delta})^3} \qquad (20)$$

where δ_m and F_m are the maximum displacement and normal force, respectively, achieved during

contact prior to restitution. Equation 19 is a proposed relationship that specifies $\bar{\delta}$ is proportional to

$F_m/F_{n(elas)}(\partial_m)$, and equation 20 is derivable from continuity. This model results in a loading curve

such as shown in Figure 7-2.
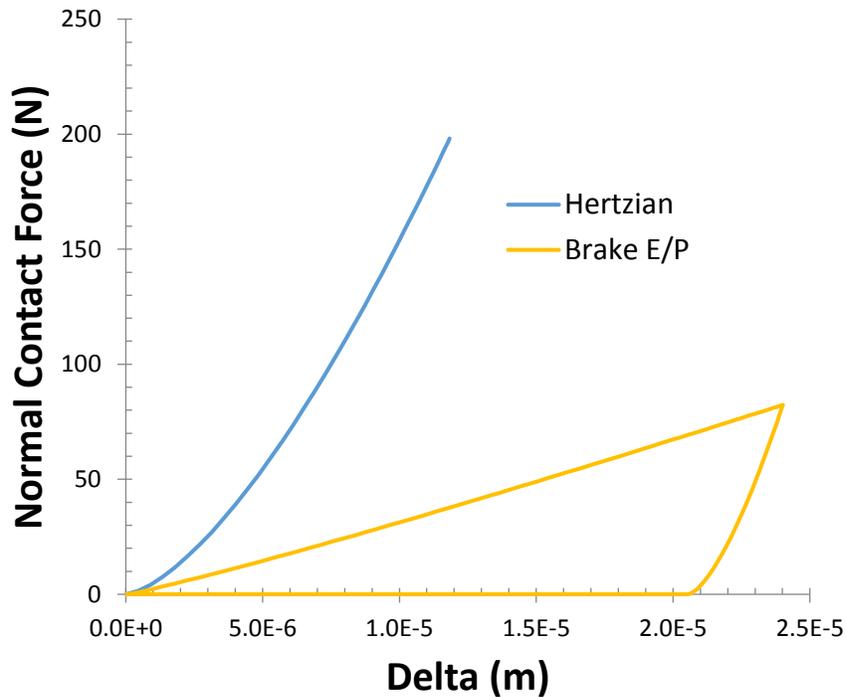
**Figure 7-2: Normal force reaction for Hertzian, Brake Elastic/Plastic Model for a 4.5m/s collision between 3.18mm spheres of Ni and WC (Courtesy Sandia National Laboratories)**

7.2 New LAMMPS Model

To incorporate the elastic-plastic contact model into LAMMPS, a new pair style is used. To allow high

levels of user control, only necessary features of the contact model are implemented into the pair style

while the remaining features are included in an initialization script, which allows users to estimate inputs from experimental data. These programs are described in what follows.

7.2.1 Pair Style gran/ep/history

The new pair style is called gran/ep/history, "ep" being an abbreviation for "elastic-plastic" and history denoting the capability to use shear history to calculate frictional effects. The handing of friction is the same in gran/ep/history as it is in gran/hertz/history, although the observed magnitude of the frictional force will be different due to the new calculation of the normal force. The damping forces are also calculated the same way, but are implemented slightly differently as noted in Eqs. 5 and 6. The new pair style accepts all the inputs that gran/hertz/history accepts and five additional terms to define the plastic behavior.

In order to implement the elastic-plastic contact model, the overall force on a spherical particle (equation 1 for gran/hertz/history) becomes:

$$F = \begin{cases} \phi_1(\delta)\big(F_{n(elas)} + F_{n(damp)}\big) + \phi_2(\delta)F_{n(plas)} + F_{t(fric)} + F_{t(damp)}: & \delta > \delta_m \\ F_{n(rest)} + F_{n(damp)} + F_{t(fric)} + F_{t(damp)}: & \delta \leq \delta_m \end{cases} \tag{21}$$

The inputs described in table 7-1 are used to calculate $F_{n(elas)}$, $F_{n(damp)}$, $F_{t(fric)}$ and $F_{t(damp)}$ in exatly the same way as gran/hertz/history. Additional inputs, detailed in table 7-2 are necessary to calculate $\phi_1(\delta)$, $\phi_2(\delta)$ and $F_{n(plas)}$.

To model a single material using gran/ep/history, insert the following lines into the input script:

```
pair_style gran/ep/history &
Kn Kt gamma_n gamma_t xmu dampflag weight cy cp p0 n
pair_coeff * *
```

Table 7-2: Additional inputs for gran/ep/history

Input:	ξ	c_y	c_p	p_0	n
Description:	Weight constant	Proportionality constant such that $$\delta_y = c_y r_{eff}$$	Proportionality constant such that $$\delta_p = c_p r_{eff}$$	Plastic flow pressure	Meyer's hardness exponent
SI Units:	None	None	None	Pa	None
Relevant Equation:	(15), (16)	(15), (16)	(15), (16)	(11)	(11)

To model two different materials, the following syntax can be used:

```
pair_style hybrid &
gran/ep11/history Kn Kt gamma_n gamma_t xmu dampflag weight cy cp p0 n &
gran/ep12/history Kn Kt gamma_n gamma_t xmu dampflag weight cy cp p0 n &
gran/ep22/history Kn Kt gamma_n gamma_t xmu dampflag weight cy cp p0 n
pair_coeff 1 1 gran/ep11/history
pair_coeff 1 2 gran/ep12/history
pair_coeff 2 2 gran/ep22/history
```

The arguments following "gran/ep11/history" are those governing a collision between two particles of material type "1", and those following "gran/ep12/history" govern a collision between a particle of type "1" and a particle of type "2", etc. This method can currently be used for up to four material types. It is important that every material interaction possible in a simulation is defined.

During a simulation, a pair of spheres may collide multiple times. Several different loading curves can result, depending on the relative positions of the spheres. Consider the following scenarios for a pair of strain-hardenable spheres. Case I, They undergo a collision, restitution, then a second collision at the same point of impact. Case II, They undergo a collision, restitution, then a second collision at a new

point not affected by the first. Case III, They undergo a collision, restitution, then a second collision in a

region of the sphere that has been deformed by the first.

(a)   (b)
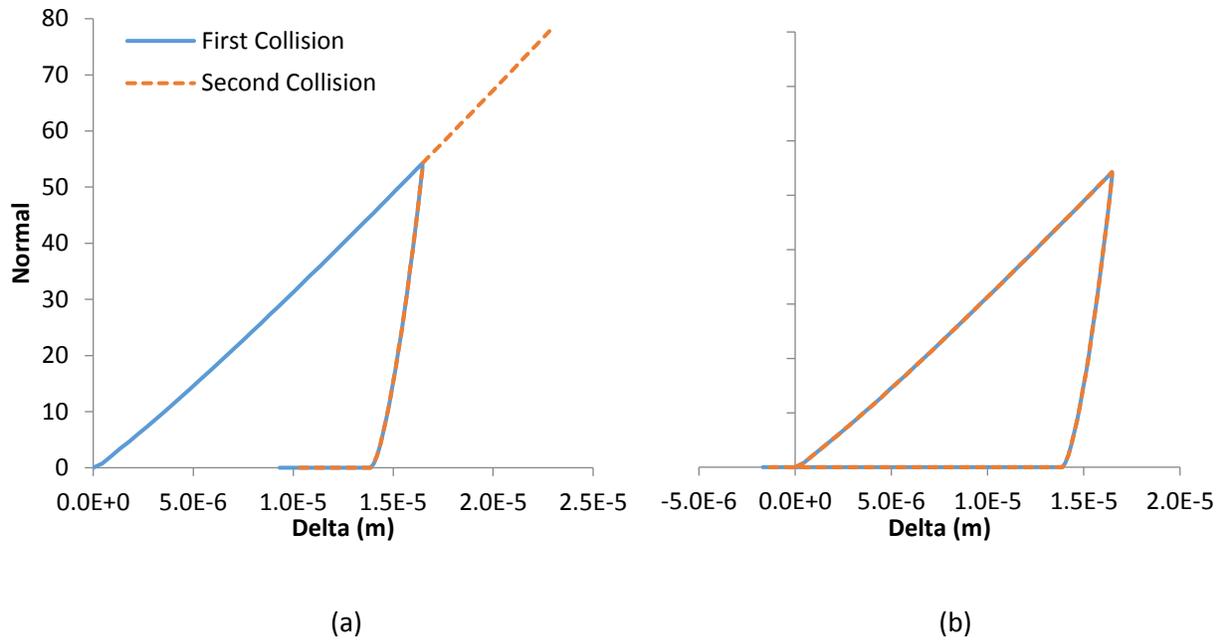
Figure 7-3: Second Collision load curves when (a) δ reaches a negative value and (b) δ remains positive (Courtesy Sandia National Laboratories)

Table 7-3: Pair Style Time Comparison

Pair Style	Average Total Simulation Time (min)	Average Pair Calculation Time (min)
gran/hertz/history	67.52	10.01
gran/ep/history	111.83	28.86

For simplicity, the model is implemented under the assumption that each subsequent impact between

two spheres that have already come in contact is one of the first two cases (Case I or Case II) and not

among the numerous potential configurations that arise when considering Case III. An example of Case I

and Case II collisions are illustrated in Fig. 3. If the distance between sphere centers is smaller than it

would be undeformed, the first scenario (Case I) is assumed. The loading curve of the second collision

then follows the restitution curve of the first collision until the maximum force of that collision is

reached, and then continues on the loading curve of the first collision (see Fig. 3a). If at any point the

153

distance between sphere centers is larger than it would be undeformed, the second scenario (Case II) is

assumed and loading begins as it did in the first collision (see Fig. 3b).

For algorithmic timing comparisons, small benchmark simulations are used that model 2000 pure nickel

particles of 5mm diameter poured into a cylindrical drum of 10cm diameter from a height of 10 cm over

0.5 sec using both gran/hertz/history and gran/ep/history. Table 7-3 documents the computational

times for 500 simulations run on four processors for both impact models. The use of gran/ep history

contributed to a 1.66x increase in computation time, largely due to a 2.88x increase in computation time

spent on pair calculations.

7.2.2 Initialization script

An initialization script was created to generate appropriate LAMMPS commands as described in *2.1.2*

using the material properties and relationships described in 1.2. For efficiency, eq 9. was replaced by

the quadratic fit in equation 22.

$$A(v) = 0.381981v^2 - 0.804221v + 0.591121 \tag{22}$$

Table 7-4: Properties required for use of gran_ep_initialize.py

Property:	E	v	σ	n	H
Description:	Young's Moduls	Poisson's Ratio	Yield Stress	Meyer's Hardness	Brinell Hardness
Units:	Pa	None	Pa	None	kgf/mm^2
Relevant Eauation:	8, 18, 19, 20	9, 22	8	11, 23	14

This equation has a correlation of $R^2 = 0.999987$. The initialization script requires the properties

detailed in table 7-4. To use this code, enter the relevant properties into the section labeled "## List of

material properties" then run the code. The output will contain the commands that must be copied and

pasted into your LAMMPS input script. Substituting the string 'unknown' for yield stress and Meyer's

hardness has two effects: 1) The code assumes other materials yield first and 2) The code generates an

154

elastic-only command for interactions between two spheres of that type. This is appropriate in the case

of one ceramic interacting with metals. For instance, if one were to run gran_ep_initialize.py with

```
# Properties for material 1
name = 'Pure Nickel'
Emod =          159e9   # Pa  % Young's modulus
nu =    0.3       # Poisson's ratio
SY =    159e6   # Pa % Yield strength
Meyer =         2.21      # Meyer's Hardness
rho =   8880    # density, kg/m^3
HB =    90        # Brinell Hardness, kgf/mm^2
# Properties for material 2
name = 'WC-10Co'
Emod =          475e9
nu =    0.22
SY =    'unknown'
Meyer =         'unknown'
rho =   14500
HB =    1167
```

the output would look like:

```
units si
pair_stlye hybrid &
gran/ep11/history 1.165e+11 0 0 0 0 0 2.100e-01 3.140e-06 1.418e-04 2.207e+08 2.210e+00  &
gran/ep12/history 1.726e+11 0 0 0 0 0 2.100e-01 1.431e-06 2.227e-04 4.098e+08 2.210e+00  &
gran/ep22/history 3.328e+11 0 0 0 0 0 0 1 1 0 2 # elastic interaction only
pair_coeff 1 1 gran/ep11/history  #Pure Nickel/Pure Nickel interaction:
pair_coeff 1 2 gran/ep12/history  #Pure Nickel/WC-10Co interaction:
pair_coeff 2 2 gran/ep22/history  #WC-10Co/WC-10Co interaction:
set type 1 density 8880
set type 2 density 14500
```

The "elastic interaction only" command is functionally equivalent to

```
gran/hertz/history 3.328e+11 0 0 0 0 0 0
```

The weight constant ξ is calculated by the empirical relationship:

$$\xi = \begin{cases} n - 2 & n > 2 \\ \delta_y/\delta_p & n \leq 2 \end{cases} \tag{23}$$

and is subject to the constraints $0.01 < \xi < 0.5$ and $F_{n(Brake)}(\delta_y) < F_{n(elas)}(\delta_p)$. If these are not met,

ξ is assumed to be 0.1 and iteratively increased by 1% until they are.

Note that these commands are for frictionless collisions with no viscoelastic damping. They would have to be edited to include these effects. Up to four materials can be modeled this way in LAMMPS, but an unlimited number of input lines can be generated in a single run.

7.3 Discussion

7.3.1 Limitations

The new pair style gran/ep/history accounts for normal plastic deformation via a model that assumes collision on a single point of contact. It does not account for changes to the normal force reaction due to small amounts of tangential sliding around deformed areas. It also does not account for plastic deformation that has occurred due to frictional forces. This model does not include temperature calculation, and therefore cannot adjust parameters due to temperature changes that would result from high energy impacts. However, this new model does include strain hardening, plasticity, and other effects as documented in [1]. For low to moderate energy impacts of metallic volumes, this is an appropriate model to use.

7.3.2 Future Work

This project could continue in a number of ways. First, the model should be validated with comparison to experimental systems, such as the drop experiments in [3]. Should the current model prove insufficient, it may be useful for the next generation of these codes to address the issues described in 3.1. This would give insight into the predictive usefulness of these factors on real systems. One physical phenomenonthat could be implemented in the short term is the elastic-plastic microslip friction model in [1]. Finally, it would be useful to compare the current model to atomistic simulations to see how each model predicts parameters such as δy and to compare the compliance curves.

References

1. Brake, Matthew Robert. "An Analytical Elastic Plastic Contact Model with Strain Hardening and Frictional Effects for Normal and Oblique Impacts." (2014): n. pag. Web.

2. Johnson, K.L., 1985, Contact Machanics Cambridge University Press, Cambridge.

3. Ambroso, M.A. et al., "Penetration Depth for Shallow Impact Cratering." (2005) Phys. Rev. E 71, 051305

4. S. Plimpton, Fast Parallel Algorithms for Short-Range Molecular Dynamics, J Comp Phys, 117, 1-19 (1995)

CONCLUSIONS

The content above describes several efforts using molecular dynamics simulation techniques to better understand plastic deformation of metals at surfaces and grain boundaries. This research highlights the role that atomistic modelling plays in understanding plasticity at the nanoscale. Atomic level resolution of the stress and strain state allows the comparison of MD simulations to experimental findings, continuum modelling and first principles modelling. Significant efforts were made in these manuscripts to present validation of the MD results by these other techniques. The main findings of these studies are, in brief:

- Stress states in plastically deformed boundaries in simulated thin film samples were thoroughly characterized.

- It was determined that large grain boundary normal stresses exist at the intersections of slip planes and grain boundaries, a finding consistent with the causal relationship proposed between dislocation channeling and embrittlement.

- Procedures were developed to directly compare stress states at these intersections in both experimental and simulated deformed samples, by their stress states and their surface step heights.

- Local stress and strain during deformation is exacerbated by additional boundary disorder, as introduced by a local melting and quenching sequence.

- Lattice dislocations were detected in random grain boundaries.

- The boundary dislocation content before and during deformation was found to be extremely dependent on the initial boundary relaxation state.

- Hydrogen was shown to cluster in grain boundaries, crating regions of high free volume where dislocation can nucleate.

- Increasing hydrogen content, at low levels, corresponded to increasing yield strength of polycrystalline materials, and an increase in crack propensity at higher strain levels.

- Near surface reordering of Ni Substrate atoms was identified in nanoindentation of Ni by a diamond indenter. This structure formed very consistently across several simulation variables including interatomic potentials and crystallographic orientation. This reordered was validated by Density functional Theory simulations.

- A new pair potential style was developed for particle dynamics modelling of strain hardenable metal spheres which includes accurate force-displacement behavior during elastic and plastic deformation.